

# Understanding heterogeneous and anisotropic porous media based on geometric properties derived from three-dimensional images

Rongrong Tian<sup>1</sup>, Tingchang Yin<sup>1</sup>, yanmei tian<sup>1</sup>, chen yu<sup>2</sup>, Jiazuo Zhou<sup>3</sup>, Xiangbo Gao<sup>1</sup>, Xingyu Zhang<sup>1</sup>, Sergio-Andres Galindo-Torres<sup>1</sup>, and Liang Lei<sup>1</sup>

<sup>1</sup>Westlake University

<sup>2</sup>University of Chinese Academy of Sciences

<sup>3</sup>China University of Geosciences

April 26, 2024

## Abstract

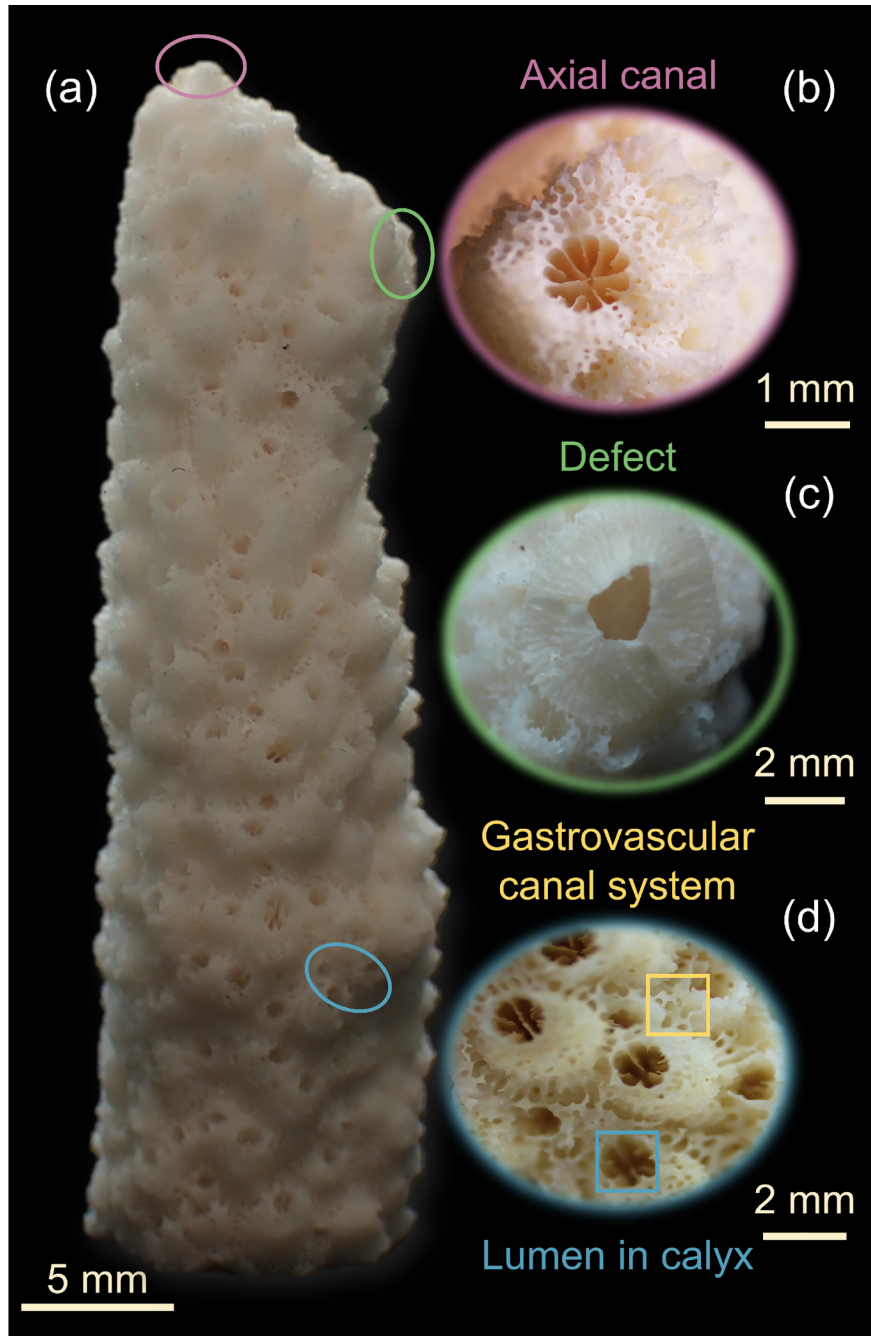
Natural porous media is generally heterogeneous and anisotropic. The structure of porous media plays a vital role and is often the source of the heterogeneity and anisotropy. In physical processes such as fluid flow in porous media, a small number of major features, here referred to as wide channels, are responsible for the majority of the flow. The thickness and orientation of these channels often determine the permeability characteristics. Typically, the identification of such major features is conducted through time-consuming and expensive simulations. Here we propose a prompt approach based on geometric properties derived from three-dimensional (3D) images. The size or radius of the major features is obtained via distance maps, and their orientations are determined by Principal Component Analysis. Subsequently, we visualize these features with color and color brightness according to their orientation and size, together with their location and distribution in 3D space. The simultaneous visualization of anisotropy (orientation) and heterogeneity (size) in one plot provides a straightforward way to enhance our understanding of pore structure characteristics. Besides, we propose a refined stereographic projection method to statistically illustrate both heterogeneity and anisotropy. Based on these insights, we further present a new way to compress the model size in numerical simulation, therefore significantly reducing the computational cost, while retaining its essential characteristics.

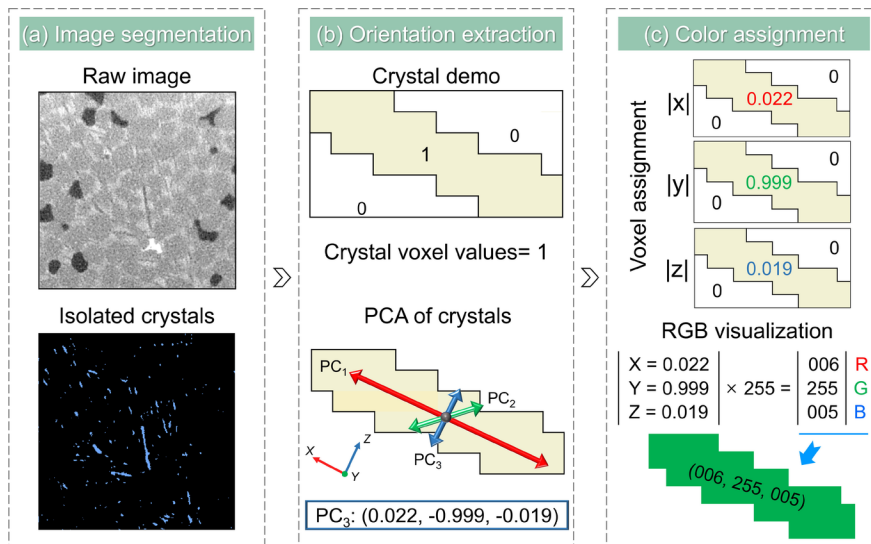
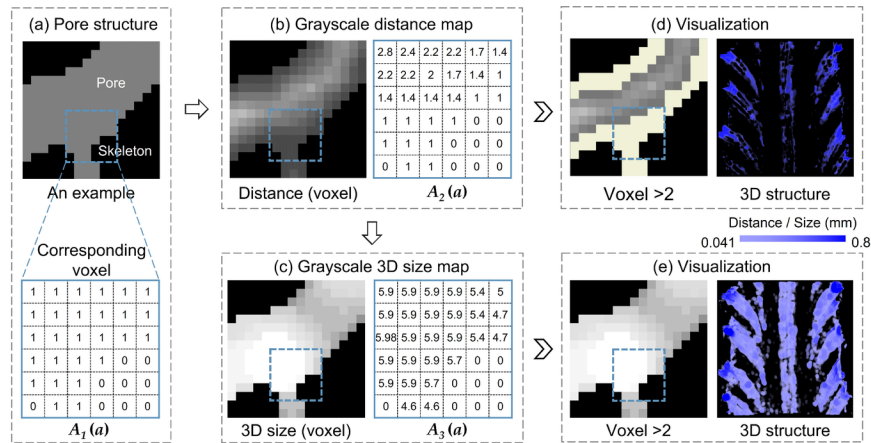
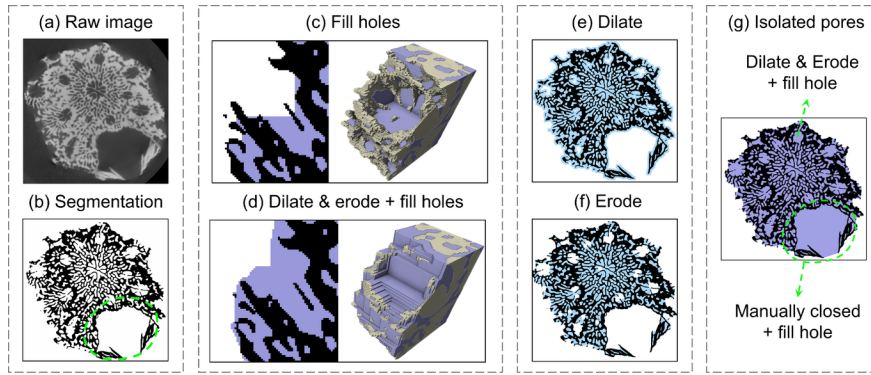
## Hosted file

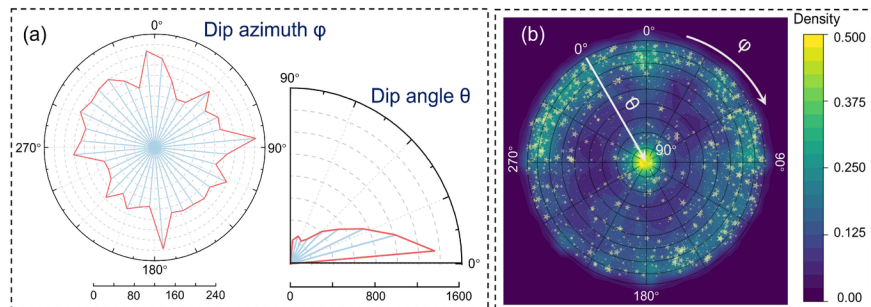
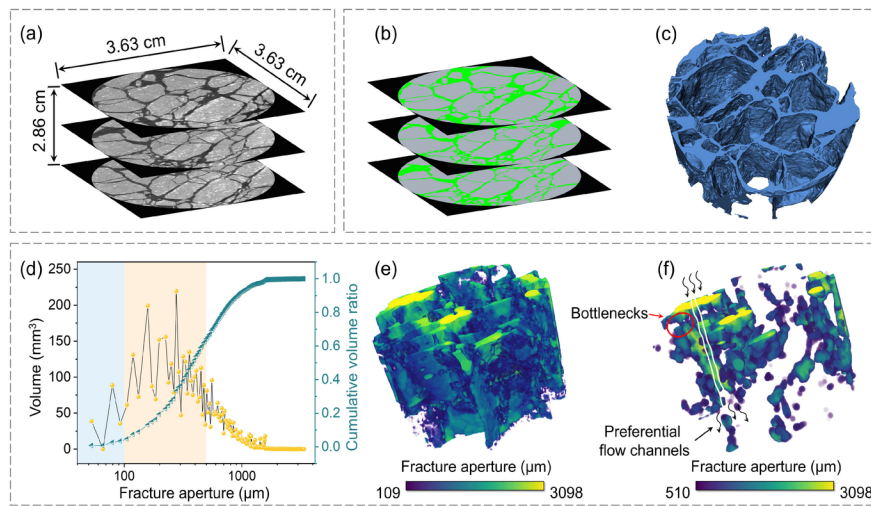
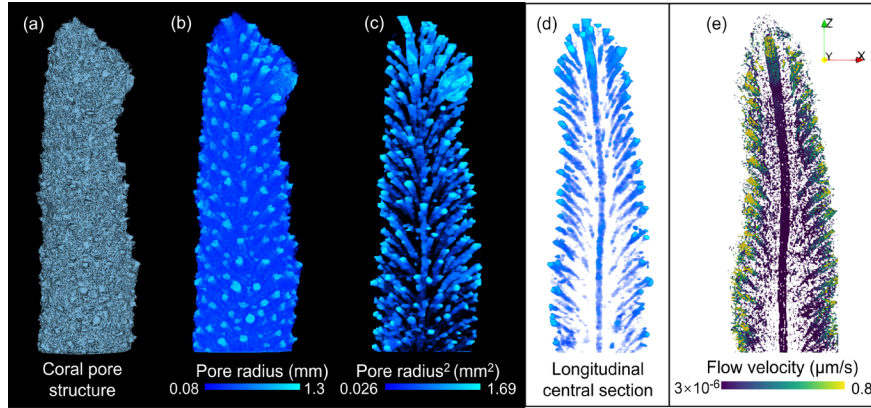
Manuscript.docx available at <https://authorea.com/users/703868/articles/862769-understanding-heterogeneous-and-anisotropic-porous-media-based-on-geometric-properties-derived-from-three-dimensional-images>

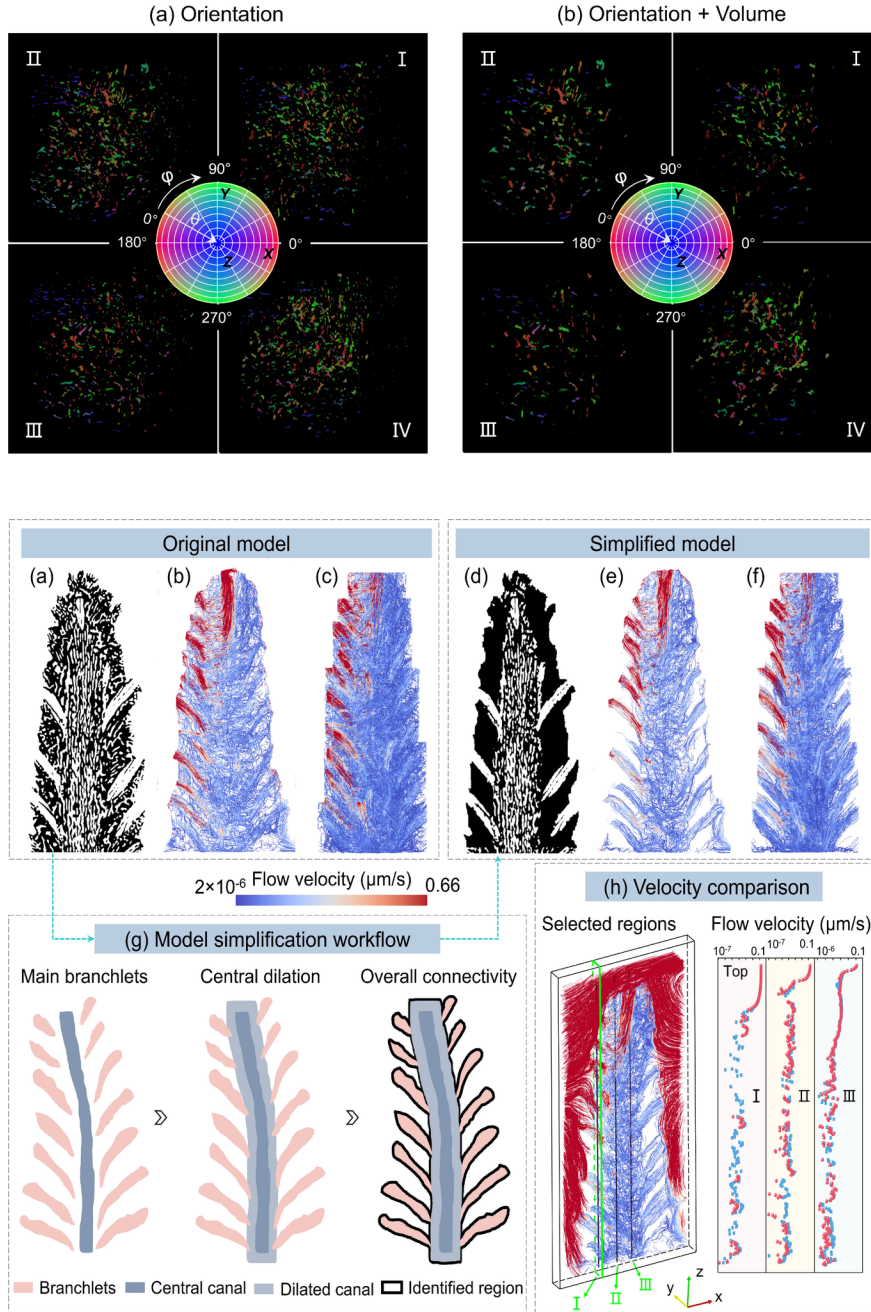
## Hosted file

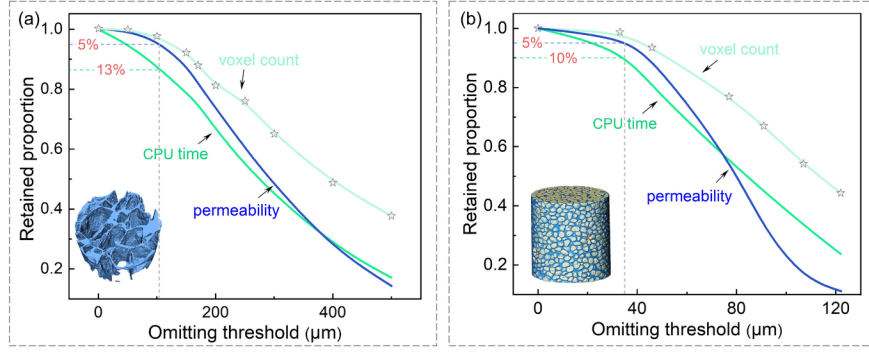
Supporting Information.docx available at <https://authorea.com/users/703868/articles/862769-understanding-heterogeneous-and-anisotropic-porous-media-based-on-geometric-properties-derived-from-three-dimensional-images>











1           **Understanding heterogeneous and anisotropic porous media based on**  
2                           **geometric properties derived from three-dimensional images**

3   **Rongrong Tian<sup>1,3</sup>, Tingchang Yin<sup>1,3</sup>, Yanmei Tian<sup>1,3</sup>, Chen Yu<sup>4</sup>, Jiazuo Zhou<sup>5</sup>,**  
4   **Xiangbo Gao<sup>1,3</sup>, Xingyu Zhang<sup>3</sup>, Sergio Andres Galindo-Torres<sup>2,3,6</sup>,**  
5   **and Liang Lei<sup>2,3,6\*</sup>**

6   <sup>1</sup>College of Environmental and Resources Science, Zhejiang University, Hangzhou,  
7   Zhejiang 310058, China

8   <sup>2</sup>Research Center for Industries of the Future, Westlake University, Hangzhou,  
9   Zhejiang 310030, China

10   <sup>3</sup>Key Laboratory of Coastal Environment and Resources of Zhejiang Province, School  
11   of Engineering, Westlake University, Hangzhou, Zhejiang 310030, China

12   <sup>4</sup>School of Chemistry and Materials Science, Hangzhou Institute for Advanced Study,  
13   University of Chinese Academy of Sciences, Hangzhou, Zhejiang 310030, China

14   <sup>5</sup>State Key Laboratory of Geomechanics and Geotechnical Engineering, Institute of  
15   Rock and Soil Mechanics, Chinese Academy of Sciences, Wuhan, Hubei 430000,  
16   China

17   <sup>6</sup>Institute of Advanced Technology, Westlake Institute for Advanced Study, Hangzhou,  
18   Zhejiang 310024, China

19   Corresponding author: Liang Lei ([leiliang@westlake.edu.cn](mailto:leiliang@westlake.edu.cn))

20  
21   **Key Points:**

- 22       • A novel method for visualizing heterogeneity and anisotropy of porous media is  
23       proposed by deriving geometric properties from 3D images
- 24       • Stereographic projection is refined to statistically demonstrate heterogeneity  
25       and anisotropy in one plot
- 26       • The enhanced understanding of heterogeneity and anisotropy leads to a new  
27       approach to simplify geometric models in numerical simulation

30 **Abstract**

31 Natural porous media is generally heterogeneous and anisotropic. The structure  
32 of porous media plays a vital role and is often the source of the heterogeneity and  
33 anisotropy. In physical processes such as fluid flow in porous media, a small number  
34 of major features, here referred to as wide channels, are responsible for the majority  
35 of the flow. The thickness and orientation of these channels often determine the  
36 permeability characteristics. Typically, the identification of such major features is  
37 conducted through time-consuming and expensive simulations. Here we propose a  
38 prompt approach based on geometric properties derived from three-dimensional (3D)  
39 images. The size or radius of the major features is obtained via distance maps, and  
40 their orientations are determined by Principal Component Analysis. Subsequently, we  
41 visualize these features with color and color brightness according to their orientation  
42 and size, together with their location and distribution in 3D space. The simultaneous  
43 visualization of anisotropy (orientation) and heterogeneity (size) in one plot provides  
44 a straightforward way to enhance our understanding of pore structure characteristics.  
45 Besides, we propose a refined stereographic projection method to statistically  
46 illustrate both heterogeneity and anisotropy. Based on these insights, we further  
47 present a new way to compress the model size in numerical simulation, therefore  
48 significantly reducing the computational cost, while retaining its essential  
49 characteristics.

50 **Plain Language Summary**

51 Natural porous media, like soil or rock, have uneven structures which make it  
52 behave distinctively depending on their specific location or orientation. While this  
53 understanding has been widely acknowledged, conventional approaches rely on  
54 time-consuming and expensive methods such as field investigations, lab experiments,  
55 or numerical simulations to guess. Although imaging techniques such as X-ray  
56 computer tomography (CT) could provide the three-dimensional structure, there has  
57 yet to be no visualization technique that directly depicts the heterogeneity and  
58 anisotropy. Here, we propose a novel method that leverages feature size  
59 (heterogeneity) and orientation (anisotropy) to enable the simultaneous visualization of  
60 both size and orientation of targeted objects. A refined stereographic projection is  
61 introduced to statistically demonstrate the heterogeneity and anisotropy within one  
62 plot. To illustrate the effectiveness of our method, we utilize examples of coral pore  
63 structure, rock fractures, and ice crystals. The derived geometric features demonstrate  
64 a strong correlation with numerical simulation results of fluid flow, thereby proving  
65 its credibility and value in enhancing our comprehension of the heterogeneity and  
66 anisotropy of porous media. Based on these findings, we further propose a new  
67 approach to simplify geometric models in numerical simulations, which significantly  
68 reduces the computational cost while preserving the overall behavior.

69

## 70 **1. Introduction**

71 Heterogeneity and anisotropy are inherent features in natural porous media.  
72 These two features are the source of the unpredictable nature of sediments or  
73 geomaterials, as the structure along with the composition determines physical  
74 behaviors. Therefore, understanding the heterogeneity and anisotropy of porous media  
75 is critical to explain observed behaviors and predict outcomes in engineering  
76 practices.

77 The approach to consider the porous media with representative elementary  
78 volume (REV) is common. REV is based on the self-similarity of microstructures and  
79 can produce representative results when pore structure properties are stationary with  
80 increasing scale (Puyguiraud et al., 2020). Such an approach allows anisotropy but  
81 assumes that the media itself is homogeneous at a certain scale (Hunt & Sahimi, 2017;  
82 Bang & Lukkassen, 1999). It is ineffective for some porous media, like bio-generated  
83 structures. For instance, the coral pore structure shows some self-similarity and fractal  
84 behavior, the branches are scaled replicas of the whole structure (Martin-Garin et al.,  
85 2007). Since the branches are orientated differently, there is no scale that yields a  
86 representative volume for fluid flow. In other words, the heterogeneity and anisotropy  
87 are throughout the entire pore structure, and the concept of REV does not apply.  
88 Therefore, the attempt to simplify the actual pore structure must be based on the  
89 actual geometry.

90 Heterogeneity is critical in determining most physical properties of the porous  
91 media. Taking fluid flow in porous media as an example, seepages in porous media  
92 are often controlled by preferential flow channels (Hyman, 2020; Shigorina et al.,  
93 2021). Predicting these channels in porous media is vital in many geophysical  
94 scientific and engineering applications, such as oil and gas recovery (Chong et al.,  
95 2017; Chen et al., 2021), CO<sub>2</sub> geological storage (Xu et al., 2020; Shahriar & Khanal,  
96 2023; Yang et al., 2018), and the estimation of subsurface contamination migration

97 (Sebben & Werner, 2016; Johnson et al., 2003). However, due to its heterogeneous  
98 porosity network, it is not practical to directly identify preferential flow channels.

99 It is difficult to properly consider heterogeneity without a real three-dimensional  
100 (3D) structure. The application of computer tomography (CT) technology (Flannery et  
101 al., 1987) and magnetic resonance imaging (MRI) (Budinger & Lauterbur., 1984)  
102 makes it possible to obtain the actual 3D pore structure, and its combination with  
103 digital image technology (Wildenschild & Sheppard, 2012; Lyu et al., 2021) enables  
104 the numerical representation of the porous media heterogeneity. However, two  
105 significant limitations remain for numerical simulations: high cost and a trade-off  
106 between the image resolution and sample volume (Silin & Patzek, 2006). The rebuilt  
107 model needs to be substantial enough to yield a meaningful result and have sufficient  
108 details to accurately depict fine pores (Jiang et al., 2013).

109 Image processing has contributed to numerical model simplification. For  
110 example, the connectivity of the pore structure can be identified by skeletonization  
111 (Ferreira & Nick, 2023, Lee et al., 1994), and thickness can be estimated by medial  
112 axis transform algorithms (Van der Walt et al., 2014) and distance transform  
113 algorithms (Grevera, 2007). On this basis, pore-network model, which was initially  
114 developed as regular lattices (Fatt, 1956), can be established to represent the  
115 connectivity and spatial arrangement of a 3D structure (Mahabadi et al., 2018; Jing et  
116 al., 2020). A pore-network model typically consists of pore nodes representing locally  
117 widest parts of pore space and bonds (sometimes called “pore throats”) connecting  
118 pores and the remainder (Jiang et al., 2017), and the flow calculation is much less  
119 expensive (Bultreys et al., 2016). However, the topology and geometry of the pore  
120 space are missing in modeling (Zhang et al., 2022), which may lead to significantly  
121 different flow properties (Nemati et al., 2020). In addition, the fractal theory is  
122 employed to characterize the pore irregularity (Zhang et al., 2020, Qin et al., 2023),  
123 yet the accuracy of this method remains uncertain since the spatial variation of pore  
124 size and pore network connectivity are neglected (Song et al., 2020).

125 The abovementioned efforts focus on heterogeneity, and the physical property in  
126 an isotropic but heterogeneous media within a small area can be represented by a  
127 scalar value. Anisotropy, on the other hand, requires the physical property to be  
128 represented by a tensor rather than a scalar (Galindo-Torres et al., 2012; Ren &  
129 Santamarina, 2018), which makes the problem more complicated. In geology,  
130 researchers focus on analyzing the distribution of fracture orientations, the fraction of  
131 void space, fracture local apertures, and preferred crystallographic orientation of  
132 minerals. These factors lead to the anisotropy. The rose diagram (Degu & Hossain,  
133 2012; Nemec et al., 1988) in geology are a common tool to describe the orientation  
134 distribution, where the petal runs along the same direction as the object, and the  
135 length of the petal depends on the frequency of the object in that direction. This  
136 method typically plots the dip azimuth and dip angle separately, although these two  
137 angles are actually coupled. Stereographic projection could be realized by projecting  
138 the geometric elements of the 3D space onto the plane (Howarth, 1996), both the  
139 longitude and latitude directions are plotted together. However, these approaches are  
140 limited to a 2D view, in which the dependencies between the individual characteristics  
141 cannot be investigated and the potential spatial regularities cannot be derived. Both  
142 rose diagrams and stereographic projections are statistical methods, showing the  
143 probability, but not the actual distribution in the space.

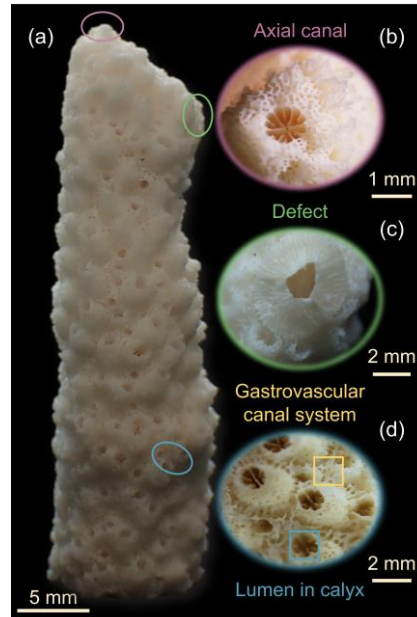
144 Overall, heterogeneity and anisotropy remain conceptual and can therefore be  
145 obscure, without direct and vivid visualization. Frequently, they are considered  
146 separately. Current literatures simplify the morphology of actual 3D structures when  
147 considering heterogeneity and anisotropy due to limitations in computational  
148 efficiency. Visualization, as a tool, has been demonstrated powerful for other purposes;  
149 for example, visualizing pore size distribution using a 3D size map (Hilderand &  
150 Ruegsegger, 1997) is a common practice (Ihli et al., 2017), and Grau et al. (2010)  
151 described a method to visually identify the shortest path between two pores by  
152 correlating the distance between a specific pore and its neighboring pores with color.

153 Therefore, it is promising and necessary to develop new visualization ways to  
154 facilitate our understanding of the heterogeneity and anisotropy of porous media.

155 Here, we propose a method to simultaneously depict heterogeneity and  
156 anisotropy in 3D structures while retaining their original morphology. We first show  
157 how size-dependent heterogeneity and orientation-dependent anisotropy can be  
158 derived from CT images. Then coral samples, rock fracture networks, and ice crystals  
159 are selected as representative examples to present the visualization results. Based on  
160 these results, we introduce a new approach to simplify geometric models in numerical  
161 simulations.

## 162 **2. Methods for Heterogeneity Characterization**

163 A coral structure and its CT images are used to demonstrate our method (Figure  
164 1). The axial canal, the lumen in the calyx, and the gastrovascular canal system  
165 linking the axial canal and the lumen in the calyx constitute the main components of  
166 the coral pore structure. Previous research (Li et al., 2021) indicates that the main  
167 branchlets of the coral canal system are significant for understanding coral growth  
168 patterns. The following workflow shows how the heterogeneous main branchlets are  
169 extracted. This workflow can be summarized as follows: image segmentation, pore  
170 structure isolation, 3D size measurement, and characterization and visualization of  
171 size-dependent heterogeneity.

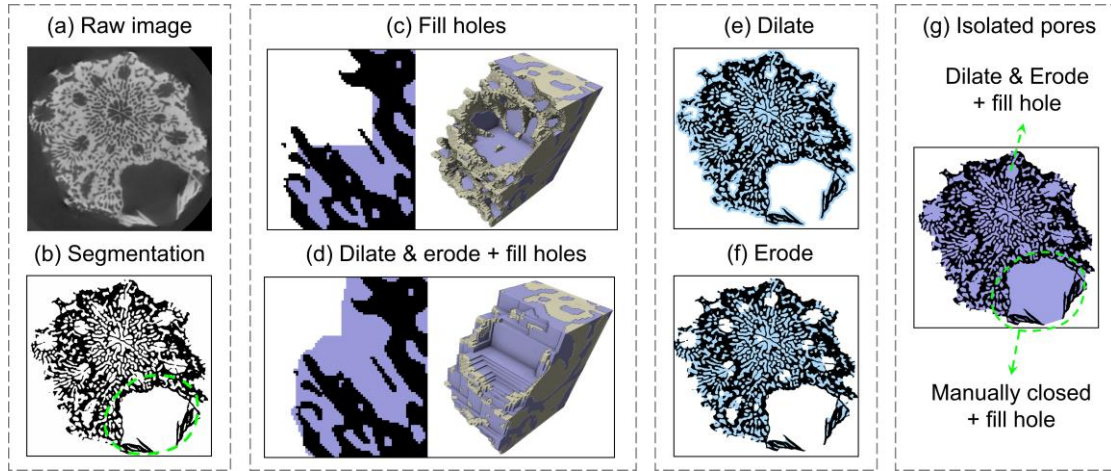


172

173 **Figure 1.** Details of a coral sample. (a) Holistic coral view. (b) Top pore  
 174 corresponding to axis canal. (c) A defect in the sample. (d) Side pores corresponding  
 175 to the lumen in the calyx and gastrovascular canal system.

## 176 2.1. Image Segmentation

177 An example image is shown in Figure 2a with a resolution of  $12.8 \times 12.8 \times 12.8$   
 178  $\mu\text{m}$  per voxel. In this image, the void space and coral skeleton exhibit different voxel  
 179 intensities, which quantifies the attenuations of X-rays as they pass through the  
 180 corresponding points with different densities and atomic numbers. Image  
 181 segmentation was carried out with ilastik (Berg et al., 2019). This machine  
 182 learning-based tool offers significant advantages over traditional threshold  
 183 segmentation and watershed segmentation methods. It learns from user-defined labels  
 184 and then assigns image voxels to different groups in a batch-processing mode. The  
 185 resulting image in Figure 2b contains two pixel values, 1 and 2, corresponding to  
 186 ‘coral skeleton’ (black) and ‘remainder’ (white, including air and coral pores).



187

188 **Figure 2.** Isolation of coral pore structure. (a) Raw CT image of the coral sample. (b)  
 189 Image segmentation. There is a notable defect circled in blue within the coral  
 190 structure. (c) Inner pore isolation by ‘fill holes’ function. (d) Inner pore isolation by  
 191 ‘3D dilate and erode’ and ‘fill holes’ functions. The black phase represents the coral  
 192 skeleton and is depicted as yellow in 3D structure, while the purple phase represents  
 193 the inner pores. (e) Volume expansion by ‘dilation’. (f) Volume shrinkage after  
 194 ‘erosion’. (g) Coral skeleton and the isolated coral inner pore structure.

## 195 2.2. Pore Structure Isolation

196 As seen in Figure 2b, the segmentation process separated the coral skeleton and  
 197 the air-filled space, which can be further distinguished into inner pores and the space  
 198 surrounding the coral skeleton. The coral pores are connected to the outside space and  
 199 filled with the same substrate, air. It is therefore difficult to isolate the pore structure,  
 200 and the challenge is to mathematically define the boundary between the pores at the  
 201 coral edge and the outside space. Here, we propose two methods based on binary  
 202 images of the coral skeleton.

203 The first method is to use the ‘fill holes’ function in ImageJ (Schindelin et al.,  
 204 2012). In most cases, the inner pores are enclosed by the coral skeleton in 2D slices,  
 205 allowing them to be filled with this function. The only issue occurs at the boundary  
 206 between pores and the outside space, where a large space cannot be filled as they may  
 207 appear to be open in 2D slices. One can apply the ‘fill holes’ function in the resliced

208 results in all x, y, and z directions. Performing boolean operations by subtracting the  
209 skeleton from the results after filling holes yields the coral pore structure. The  
210 visualization of the outcome is shown in Figure 2c.

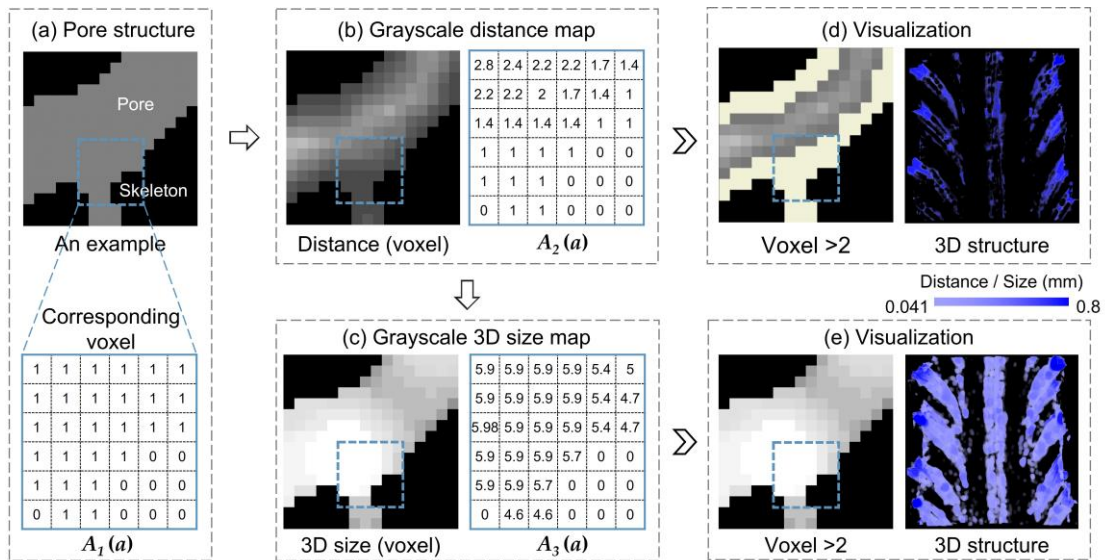
211 In the second method, we apply the 3D ‘dilate’ function N times to close the  
212 pore openings (Figure 2e), and then apply the 3D ‘erode’ function the same N times to  
213 retreat from the over-occupied voxels while retaining the closed pore openings  
214 (Figure 2f). The value of N depends on the size of the pore openings: a small N value  
215 can not close large pores, whereas a large N value will render a more spherical coral  
216 outline, resulting in the loss of distinctive pore features. One can choose a good N  
217 value (N=5, in this paper) if the coral pore openings are relatively homogeneous in  
218 size. In the case of Figure 2a, which features a defect in the coral that requires a large  
219 N value that hurts the coral outline, we use a small N value to close small pore  
220 openings and manually close the large opening at the defect. Large pores or certain  
221 portion of the large pores could be left empty after N times of erosion-expansion  
222 cycles (Figure 2f). The unfilled portions are then filled with the 3D ‘fill holes’  
223 function to obtain a summation of the coral skeleton and inner pores (Figure 2g). Then  
224 the subtraction of the coral skeleton from the summation yields the coral pore  
225 structure. Eventually, the three phases in the CT image: coral skeleton, pore structure,  
226 and air (outside space) are successfully distinguished in Figure 2g. The visualization  
227 of the result is shown in Figure 2d.

228 In general, the pore structure obtained by the first method is conservative, and  
229 some of the pore space is left as outer space. The second method aligns more closely  
230 with human judgment, although it typically introduces some additional voxels at the  
231 coral surface and sometimes requires manual intervention.

### 232 **2.3. Feature size determination**

233 The heterogeneity of porous media is primarily determined by morphology,  
234 which can be characterized by the local size of the 3D pore structure (Hilderand &  
235 Ruegsegger, 1997). Part of the three-phase image (Figure 3a) is used as an example to

236 illustrate the determination process of feature size, which includes 3D Euclidean  
 237 distance (Merchant et al., 2023) measurement (Figure 3b) and 3D size determination  
 238 (Figure 3c). Matrix  $A_1(a)$  in Figure 3a stores the initial voxel values of the three-phase  
 239 images (Figure 2g). The algorithm of 3D distance and size measurement is accelerated  
 240 in parallel (Chandra et al., 2001), and further details are given in Text S1-S5 in  
 241 Supporting Information. Eventually, each voxel within a specific pore is assigned a  
 242 value according to its corresponding 3D distance and size. Specifically, the voxel  
 243 values in Figure 3b are assigned as the distance from the voxel to the closest pore wall,  
 244 while the voxel values in Figure 3c are assigned as the radius of the largest inscribed  
 245 circle that contains the voxel. These values are stored in the computed matrices  $A_2(a)$   
 246 and  $A_3(a)$ , respectively.



247

248 **Figure 3.** Coral pore size determination and visualization. (a) Isolated pore structure.  
 249 (b, c) Grayscale 3D distance and size map. (d, e) Extraction of main pore networks  
 250 after setting thresholds on the 3D distance and size maps, respectively. The same color  
 251 bar is applied.

252 **2.4. Heterogeneity Characterization and Visualization**

253 The heterogeneity characterization should be combined with geophysics. For  
 254 example, in fluid flow through a cylindrical tube, the average pore fluid velocity is

255 proportional to the square of the pore radius ( $R$ , similar to the value determined in the  
256 3D size map) according to the Hagen-Poiseuille equation, and the overall flux is  
257 proportional to the fourth power of  $R$ . If the goal is to analyze the stiffness of the coral  
258 skeleton, then section modulus is proportional to the cube of the local skeleton  
259 diameter. In all these cases, the diameter or the feature size is the key.

260 For extracting main flow channels, we can set a threshold value to display only  
261 larger pores. If this operation is conducted on the 3D distance map, the pore surface  
262 voxels are all with the same value which indicates the distance to the nearest coral  
263 skeleton. Therefore, the peripheries of all pore structures are lost due to their smaller  
264 values (rendered in yellow in Figure 3d). This immediately reveals the topology of a  
265 structure and areas with poor connectivity.

266 If the operation is conducted on the 3D size map, in which the peripheral  
267 voxels are also assigned with the pore size, the complete pore structure meeting the  
268 threshold value is retained. The visualization allows one to distinguish pore size by  
269 color brightness (Figure 3e).

270 3D visualization is produced via 3Dslicer, a free and open-source software  
271 platform for the visualization of medical, biological, and other 3D images (Fedorov et  
272 al., 2012). The 'Volume Rendering' module allows users to specify pore surface color  
273 with voxel value (which stores pore size), and therefore the 3D size of major pores,  
274 their 3D location or distribution, and connectivity are all visualized simultaneously. If  
275 the purpose is to visualize the average velocity of the fluid flow, one can multiply the  
276 matrix  $A_3$  by itself to obtain the square of the 3D size map in the visualization.

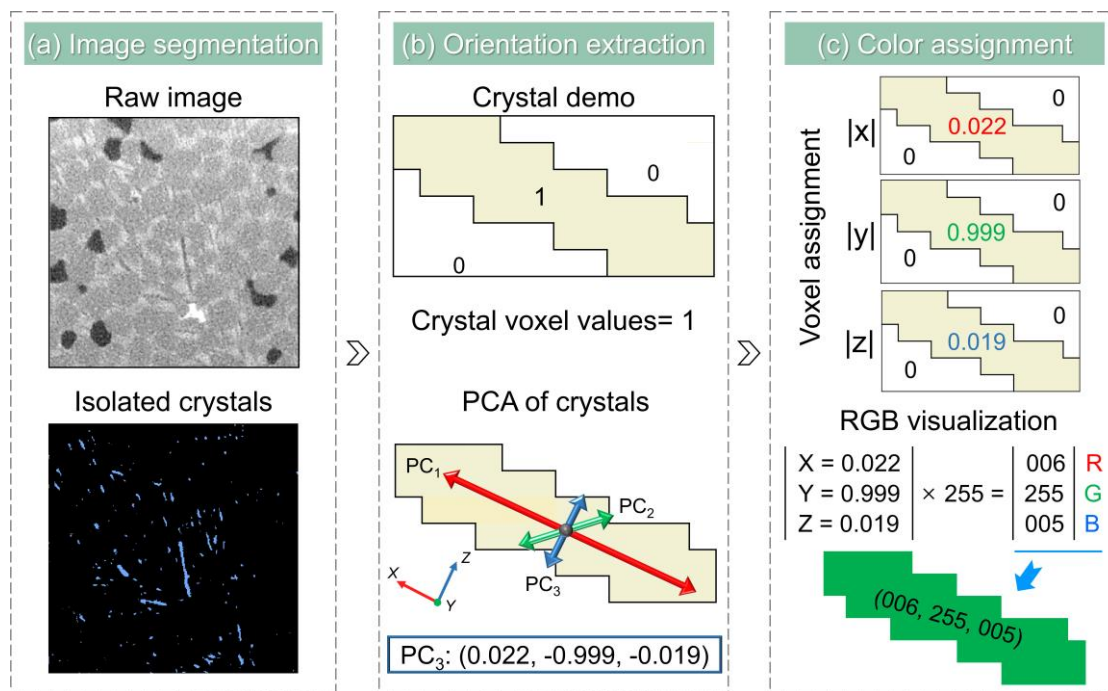
### 277 **3. Methods for Anisotropy Characterization**

278 Physical properties such as permeability and electrical resistivity have been  
279 proven to show anisotropy due to the anisotropy of the pore structure. Here, we take  
280 CT images of ice crystals as a demo to simultaneously depict the orientation and  
281 volume (or size) of individual ice crystals using color and color brightness.

### 282 **3.1. Feature Identification of Individual Ice Crystals**

283 The raw data in Figure 4a consists of CT images of a freezing salty sand  
284 specimen saturated with 5% KI solution. The ice nuclei in the pores are often platy  
285 and therefore have preferential growth orientations. The procedure for identifying  
286 crystal features is shown in Figure 4.

287 The identification of ice crystals anisotropy is carried out with ilastik. Crystals  
288 are isolated from segmented images to facilitate feature identification (Figure 4a).  
289 Here, orientations and volumes of ice crystals are selected to demonstrate their  
290 anisotropy. Specifically, crystal volumes are determined by corresponding voxel  
291 numbers, and Principal Component Analysis (Anderson, 1963) is employed for  
292 orientation characterization (Figure 4b). Three principal components corresponding to  
293 the long, medium, and short axes are obtained. The selection of feature principal  
294 components depends on the object shape and driven research questions. Given that the  
295 crystals are platy and thin along their short axes, we choose the third principal  
296 component,  $PC_3$ , which is perpendicular to the crystal's major plane, to visualize  
297 orientations. The identified ice crystals and obtained features of ice crystals serve as  
298 the input data for the subsequent color assignment. More details about the operation  
299 can be found at <https://www.ilastik.org/documentation>.



300

301 **Figure 4.** Ice crystal orientation identification and visualization. (a) Images  
 302 segmentation. Isolated ice crystals segmented from a raw image. (b) Crystal  
 303 orientation extracted by Principal Component Analysis (PCA). (c) Color assignments  
 304 for crystal voxels based on the third principal component's  $|x|$ ,  $|y|$ , and  $|z|$  coordinates.

### 305 3.2. From Anisotropy to Color Assignment

306 The computed anisotropic features are now in the form of data. Here we propose  
 307 a method to assign colors to the crystals according to their corresponding orientations.  
 308 Three coordinates of the principal component  $PC_3$  are mapped to three components in  
 309 the RGB color system, which constructs various colors based on a combination of red,  
 310 green, and blue. A normalization step is required to scale up the range of the three  
 311 coordinates of  $PC_3$  from  $[0, 1]$  to  $[0, 255]$  in the RGB system (Figure 4c). Note there  
 312 could be negative values for the coordinates in a principal component, and 8 cases  
 313 when considering the signs of the three coordinates can be reduced to 4 cases if we  
 314 flip all the signs simultaneously to avoid negative  $z$ -axis coordinates as the orientation  
 315 remains during this operation. Therefore, we can demonstrate the orientation of the  
 316 crystals in a 3D view with four plots, in which the colors denote the orientations.

317 Considering that principal components are unit vectors with only two

318 independent variables, there is an additional variable left to present another feature of  
319 the crystals. Here we use the crystal size as an example. The crystal size is used to  
320 decide the modulus of the unit vector. Specifically, the three coordinates of unit  
321 vectors are linearly adjusted according to the volume ratio between the corresponding  
322 crystal and the largest crystal. So that the brightness of a certain color (or the  
323 combination of RGB) represents the crystal size, that is, larger crystals are brighter  
324 and smaller crystals are dimmer. In this way, both of the two features, orientations,  
325 and volume, are represented in the same 3D view. The volume used here could be  
326 replaced by elastic modulus, density, wave velocity, or anything else to demonstrate  
327 heterogeneity.

328 The color assignment is carried out with Matlab, and its pseudocode is given in  
329 Text S6 in Supporting Information. One example of this procedure is shown in Figure  
330 4c. The voxels of ice crystals are assigned with  $|x|$ ,  $|y|$ , or  $|z|$  values of related vectors  
331 separately. At last, three files are computed and then imported into ImageJ to integrate  
332 them into one RGB file, where  $x$ ,  $y$ , and  $z$  are replaced by one RGB value of the  
333 relevant crystal. The combined characteristics of orientations and volume of ice  
334 crystals are visually highlighted and classified in 3D view.

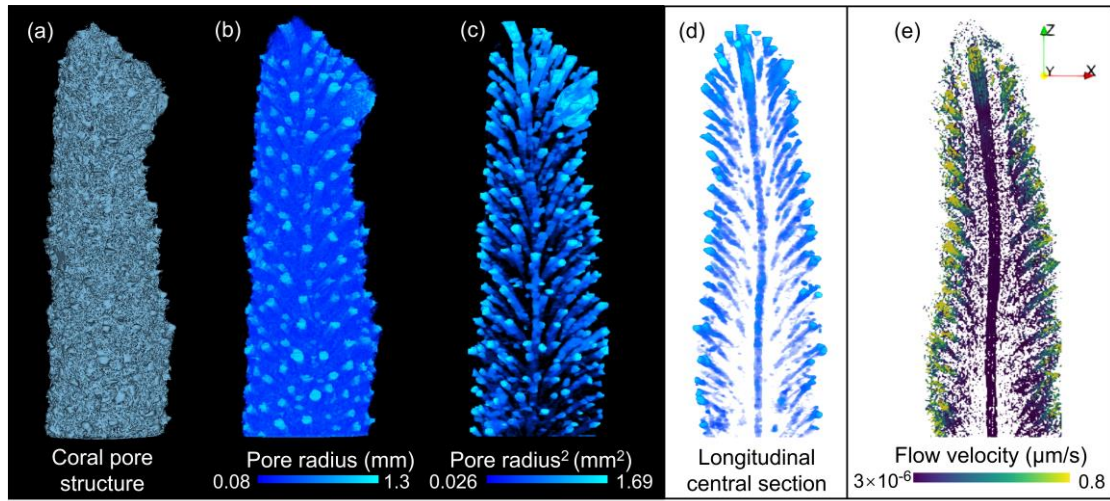
## 335 **4. Results and Applications**

336 This section uses three examples to show the visualization results and discusses  
337 how these visualizations enhance our understanding of the heterogeneity and  
338 anisotropy of porous media. These results are further used to generate a new approach  
339 to simplify geometric models in numerical simulations.

### 340 **4.1. Coral Pore Structures**

341 Understanding the flow paths within coral pore structures helps researchers  
342 comprehend carbon and nutrient cycling, as coral reefs are essential components in  
343 the biogeochemical cycle. The visualization of isolated coral pore structures is shown  
344 in Figure 5a. The intricate voids of coral gastrovascular canal system make it difficult

345 for researchers to extract the main branchlets (axial canal and lumen in calyx) from  
 346 complex pore structures.



348 **Figure 5.** 3D visualization of the coral pore structure under various situations. (a)  
 349 Isolated coral pore structure. (b) Color-coded visualization of coral pore size. (c)  
 350 Extraction of coral main branches. (d) Intercepted central section of coral branches  
 351 along the longitudinal plane, with a color-coded scale bar identical to that in (c). (e)  
 352 Thresholded velocity distribution obtained by LBM to show main flow channels and  
 353 velocities.

354 Figure 5b shows the visualization of the 3D pore size with the method in  
 355 Section 2.4, in which false color is assigned to the voxels according to the pore size.  
 356 The color varies from deep to light blue as pore size increases, therefore pore size can  
 357 be distinguished by the color of the pore surface. One can roughly locate the major  
 358 branchlets. We further filter pores smaller than a particular size by thresholding and  
 359 denoising, and the branch distribution of the coral canal system is obtained (Figure  
 360 5c). The coral pore structure mainly consists of an axis channel and surrounding  
 361 branchlets, resembling a tree. While all branchlets are connected to the main trunk in  
 362 a tree structure, each branchlet in a coral system is relatively independent, with only  
 363 small channels connecting with the axial canal. These small channels are filtered out  
 364 during thresholding.

365 The visualization of the main branchlets of the coral pore structure not only  
366 helps to grasp the key heterogeneity but also sheds light on the hydrodynamic  
367 properties of the coral structure. According to Hagen-Poiseuille's equation, as also  
368 mentioned in Section 2.4, the average flow velocity in a round tube is proportional to  
369 the square of the tube diameter. Therefore, for comparison with the later obtained flow  
370 velocity, we present the values of  $R^2$  here. The fluid flow within the coral sample,  
371 driven by ocean currents, is simulated with the Lattice Boltzmann Method (LBM),  
372 and the simulated boundary conditions are detailed in Table S1 and Figure S2 in  
373 Supporting Information. In Figure 5d, at the periphery of the branchlets, the pore size  
374 reaches its maximum, and the flow velocity also reaches the largest in Figure 5e. In  
375 the area with a larger aperture, the simulation results show a larger flow rate.  
376 Therefore, the distribution of flow velocity can be predicted with the color-coded pore  
377 size.

378 One of the key advantages of the visualization lies in its efficiency in extracting  
379 main flow paths through porous media and its scale independence compared with  
380 numerical simulations. The coral pore structures contain a large number of tiny pores  
381 in addition to the tree-shaped branches, and including these tiny pores in the  
382 simulation greatly increases the computational cost because a large number of grid  
383 cells are required. Due to the large data size, model simplification is frequently  
384 required. For studies that prefer to preserve the entire structure, researchers often need  
385 to ignore certain details of the reconstructed model by sacrificing the resolution to  
386 shorten the computational time, which retains the physical size of the model but uses a  
387 coarser mesh. For the proposed method, as long as the resolution of the image is  
388 sufficient, the results we obtain cover all details. Comparatively, the computational  
389 cost of the full-resolution image with our method is still 1/100 of the fluid dynamic  
390 simulation (LBM simulation used here) with a quarter reduced resolution. The prompt  
391 analyses, purely based on geometry, although simple, could greatly help our  
392 understanding of the pore structure by identifying the skeleton as the main contributor  
393 to the flow. Furthermore, these analyses do not rely on computing power and therefore

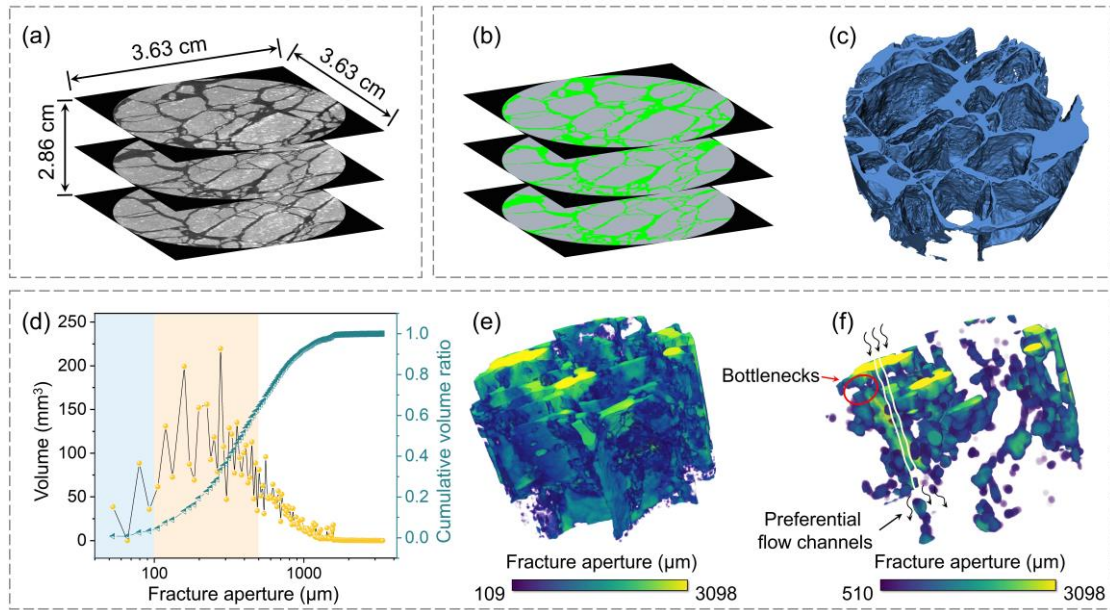
394 can be applied to a large area. In addition, it is easy to conduct such analyses on  
395 different portions of porous media and merge the results afterward, while a similar  
396 approach with LBM simulation is not applicable.

#### 397 **4.2. Fractured Rock**

398 Identification of preferential flow channels in rock masses and sediments is  
399 universally required in geological engineering. Here we take fractured rock as  
400 examples to demonstrate the application of our method in preferential flow channels  
401 extraction. Preferential flow channels here are defined by the seepage characteristics  
402 of good connectivity and high fracture apertures.

403 A rock sample and fracture details are shown in Figure 6a. The omnidirectional  
404 fracture network extracted from CT images makes it difficult to determine the  
405 preferential seepage path without further processing (Figure 6c). Preferential flow  
406 channels are positively correlated with the aperture and connectivity of fractures.  
407 According to Hagen-Poiseuille's equation, the flow velocity in planar flow channels is  
408 proportional to  $R$ , and the volume flow is proportional to  $R^3$ . Therefore, the quantitative  
409 analysis of fracture aperture distribution in rock sample based on 3D size  
410 determination algorithm is critical.

411



412

413 **Figure 6.** Details of the fractured rock sample and its connectivity visualization. (a)  
 414 Rock sample size and its raw CT images. (b) Segmented images. The gray and green  
 415 phases are rock and fracture. (c) 3D fracture structures. (d) The distribution of fracture  
 416 apertures. (e, f) 3D visualization of remaining fracture structure after excluding pores  
 417 less than 100 and 500  $\mu\text{m}$ . 100  $\mu\text{m}$  has little effect on the whole structure connectivity,  
 418 while 500  $\mu\text{m}$  is the maximum threshold value before connectivity is lost.

419 The fracture aperture shows obvious heterogeneity, as shown in Figure 6d, and  
 420 small pore throats are common, which can be the bottleneck that limits the flow  
 421 continuity. To identify the size of the pore throats that would affect the fracture  
 422 network connectivity, we use different threshold values on the full fracture network  
 423 and identify the exact location of the pore throats. When pores with radius less than  
 424 100  $\mu\text{m}$  are hidden, the connectivity of the fracture network is not greatly affected  
 425 (Figure 6e). However, when the threshold value is up to 500  $\mu\text{m}$ , the connectivity of  
 426 the fracture network deteriorates significantly, and one bottleneck appears (circled in  
 427 red in Figure 6f). There is still one large aperture area marked in black that remains  
 428 connected vertically, indicating its major contribution to the flow. We consider the  
 429 preferential flow channels as the remaining fracture network.

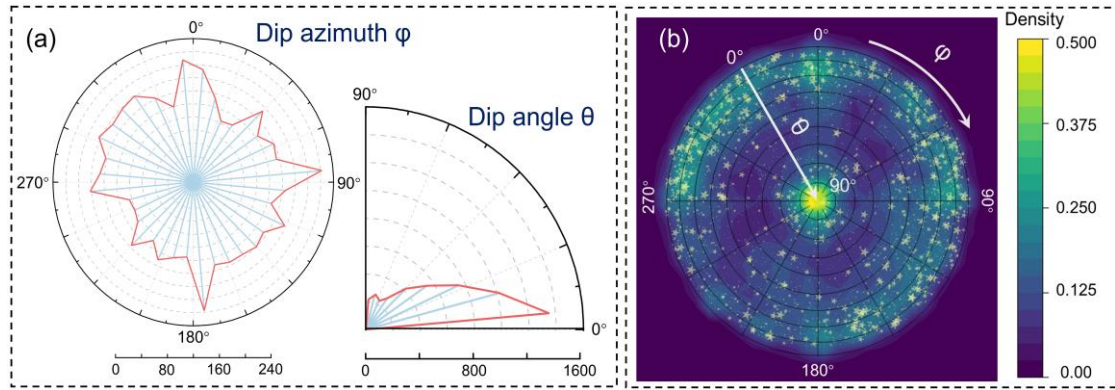
430 Additional permeability analyses of the rock sample with Avizo are carried out to

431 verify the reliability of identified preferential flow channels with fractures larger than  
432 500  $\mu\text{m}$ , and the results are given in Text S7 in Supporting Information. The results  
433 prove the effectiveness of this method in predicting preferential flow channels, and  
434 the velocities at different locations can also be roughly compared with fracture color  
435 representing aperture.

### 436 **4.3. Ice Crystals**

437 Symmetry breaking occurs during crystallization. The formed crystals frequently  
438 show directional behavior. Anisotropy of crystals results in directional-dependent  
439 strength, stiffness, and deformation characteristics. Revealing crystal orientations  
440 within a rock can help us interpret its anisotropic properties. We use ice crystal  
441 formation in a salty sandy specimen as an example. Ice crystal images used here are  
442 from the nucleation stage, revealing crystal orientations that can help us understand  
443 the nuclei growth preference (Anderson et al., 2017).

444 Rose diagram and equal-area stereographic projection are used first to show the  
445 statistics of crystal orientations (Figure 7). A significant number of dip angles around  
446  $0^\circ$  indicates the crystals show a preferential growth orientation along vertical  
447 directions (note that the axis perpendicular to the crystal major plane is selected to  
448 demonstrate the crystal orientation). In Figure 7b, the semi-sphere is expanded to a 2D  
449 plane according to equal-area stereographic projection (Text S8 in Supporting  
450 Information). Equal-area is chosen so that the density in Figure 7b (shown as cloud  
451 colors), defined as the number of crystals per unit area, demonstrates the probability  
452 of crystal orientations. The color bar encodes the point density in the subregion, which  
453 also represents the probability of crystal orientations. The main orientation is easily  
454 visible as yellow areas, which represent a strong prevalence along the horizontal axis,  
455 and the central high density is caused by its relatively small equal area. Additionally,  
456 it correlates the volume of each crystal with the size of the dot. Crystals with volumes  
457 bigger than 1000 voxels are all set as 1000 voxels, so that there are no abnormal dots  
458 overlapping with adjacent smaller dots.



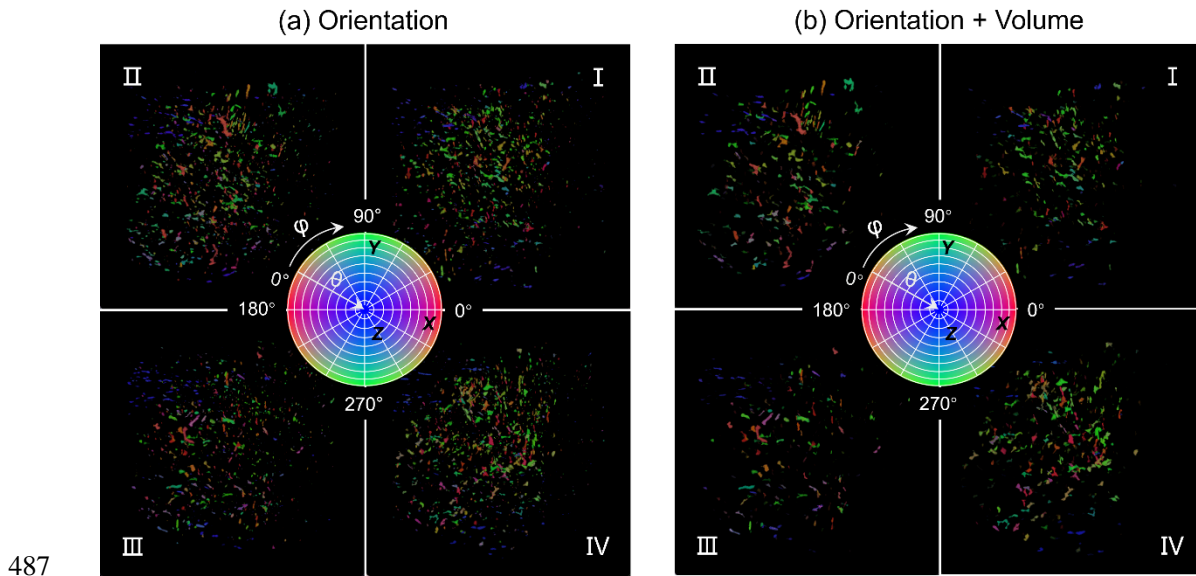
459

460 **Figure 7.** Statistic of crystal orientation distributions. (a) Rose diagram. The dip  
 461 azimuth  $\phi$  ranges from  $0^\circ$  to  $360^\circ$ . The dip angle  $\theta$  ranges from  $0^\circ$  (horizontal) to  $90^\circ$   
 462 (vertical), showing the angle inclined from the horizontal plane. (b) Equal-area  
 463 stereographic projection. The dip azimuth  $\phi$  and dip angle  $\theta$  correspond to that in (a).

464 In this method, the correspondences between features and the crystals are  
 465 missing. All crystals are gathered at the same origin, and the original location of each  
 466 crystal, along with the relative position between different crystals, is not available.  
 467 Besides, the morphology of the crystal, as a key anisotropic characteristic, is absent.  
 468 We show both the morphology, spatial distribution, and orientation of all crystals in  
 469 one visualization (Figure 8a) and further correlate the color brightness with the crystal  
 470 size in Figure 8b, where the brightness of the color demonstrates the crystal size (See  
 471 3D animations in Data Set S1 in Supporting Information). Here, the maximum  
 472 volume is set as 500 voxels to avoid extensive crystal darkening. Crystals larger than  
 473 500 voxels maintain their original color, while those smaller than 500 voxels appear  
 474 dimmer. The crystal size shown as the color brightness can be replaced by another  
 475 characteristic when necessary. For example, it can be either fracture aperture, length,  
 476 or aspect ratio in geology.

477 We plot the color coding overlapping the stereographic projection orientations in  
 478 the center of the four quadrants (Figure 8). One can then look for the orientation of a  
 479 particular crystal according to its color and correspondingly find its dip angle and dip  
 480 azimuth. The group behavior among homooriented crystals is clearly identified, with  
 481 the major vertically orientated crystals (crystals with color ranging between red and

482 green in Figure 8) spreading across other regions. This indicates that the nuclei prefer  
 483 to grow along the z-axis, aligning with the direction of the temperature gradient, while  
 484 the minority of blue crystals accumulate at the side corner. Such a trend would not be  
 485 possible to discern in a stereographic projection plot, which, in turn, highlights the  
 486 necessity of the proposed 3D visualization.



487  
 488 **Figure 8.** Visualization of anisotropic characteristics of ice crystals with four  
 489 quadrants (a) Orientation visualization. (b) Simultaneous visualization of orientation  
 490 and volume. Red, green, and blue colors signify x, y, and z coordinates of vectors,  
 491 respectively. Various colors are generated by blending these three primary colors  
 492 according to their corresponding vector coordinates. This integration process produces  
 493 a spectrum of colors, which is presented in the form of equal-area stereographic  
 494 projection. Each color represents a unique orientation, and the determination of  
 495 orientation follows the illustration in Figure 7.

496 We have compared this method with those found in the literature across fields  
 497 including fiber-reinforced composites, geology, and crystallography. Mishurova et al.  
 498 (2017) presented the orientation of fibers by two plots to separately demonstrate the  
 499 azimuth angle and dip angle. In crystallography, the most well-known color coding is  
 500 the crystal orientation map, which also needs two plots to identify one direction

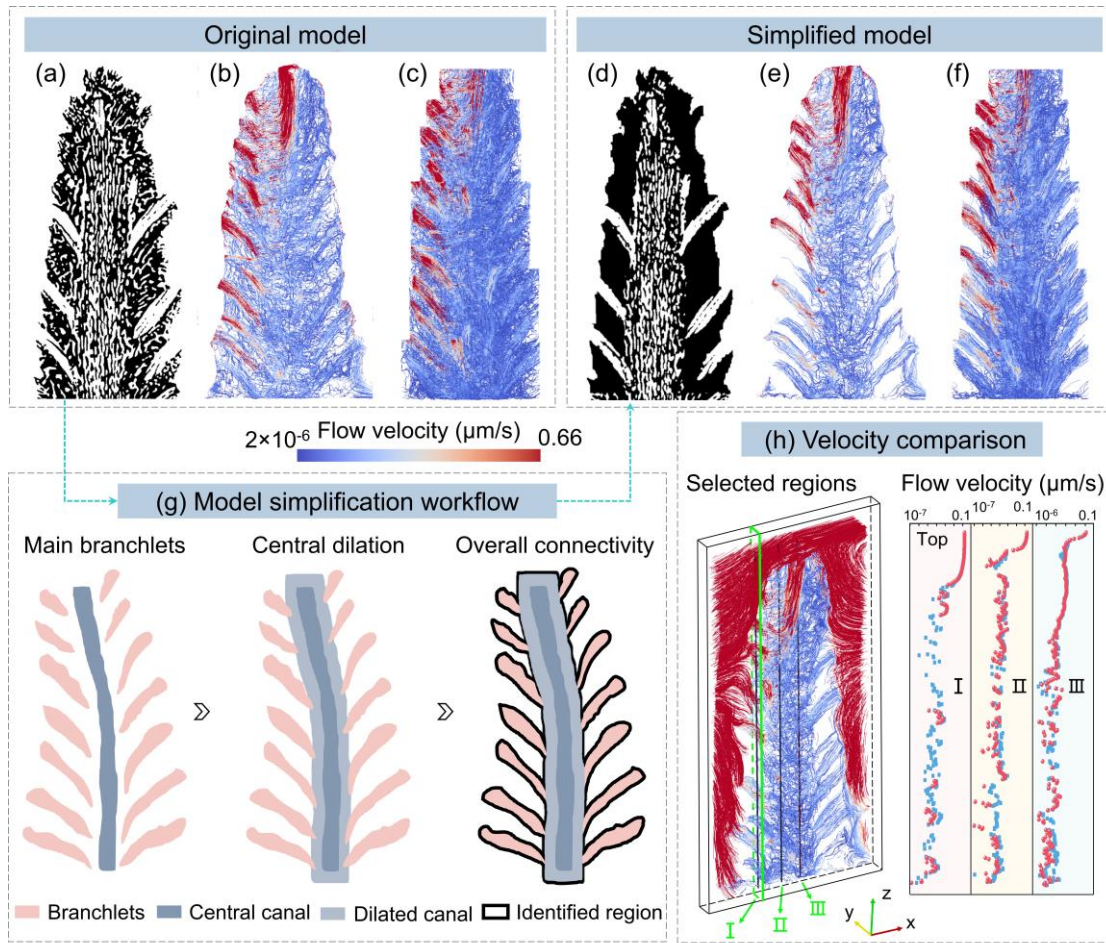
501 (Wittwer & Seita, 2022). Therefore, it is difficult to grasp the orientation directly in  
502 these two methods. Robb et al. (2007) used a color sphere based on a combination of  
503 the azimuth angle and dip angle. Weissenböck et al., (2014) used the same color map  
504 as us but did not divide it into four cases. However, in both of these two methods,  
505 specific colors could represent more than one orientation, and sometimes the  
506 orientation difference between two features shown with the same color could be more  
507 than 90 degrees. In comparison, our method demonstrates the direction in just one plot,  
508 and a unique direction could be traced to one color in one of the four quadrants. The  
509 three colors RGB naturally align with the x, y, and z directions, which makes it a  
510 natural match with the Cartesian coordinate system and, therefore, more intuitive. In  
511 addition, we combine size or any other heterogeneity with orientation in just one plot,  
512 a feature not available in existing methods.

#### 513 **4.4. Geometrical Model Simplification for Numerical Simulation**

514 Previous sections have demonstrated the effectiveness of our method in  
515 enhancing the understanding of porous media heterogeneity and anisotropy. Based on  
516 this understanding, we further discuss its potential for geometrical model  
517 simplification in the numerical simulation.

518 The fluid flow simulation results of the coral sample show that the filtered tiny  
519 pores have little influence on the ultimate flow properties of the coral pore structure,  
520 as discussed in Section 4.1. This provides a new approach to simplify the geometric  
521 model by filtering out tiny pores at the periphery of the coral structure, which can  
522 greatly improve computational efficiency without losing reliability. The simplest way  
523 is to use only the main branchlets of the coral pore structure; however, the central  
524 canal is disconnected from the branchlets. Therefore, we purposely retained the small  
525 pores around the central canal to ensure connectivity. As shown in Figure 9g, the  
526 central canal is dilated  $M$  times, connecting all the branchlets, the Boolean  
527 conjunction of the dilated central canal and the branchlets defines the region (labeled  
528 as the identified region) in which all inner pores should be included in the simulation.  
529 Such an approach guarantees a good connectivity among all the main channels while

530 involves only a small number of small pores.



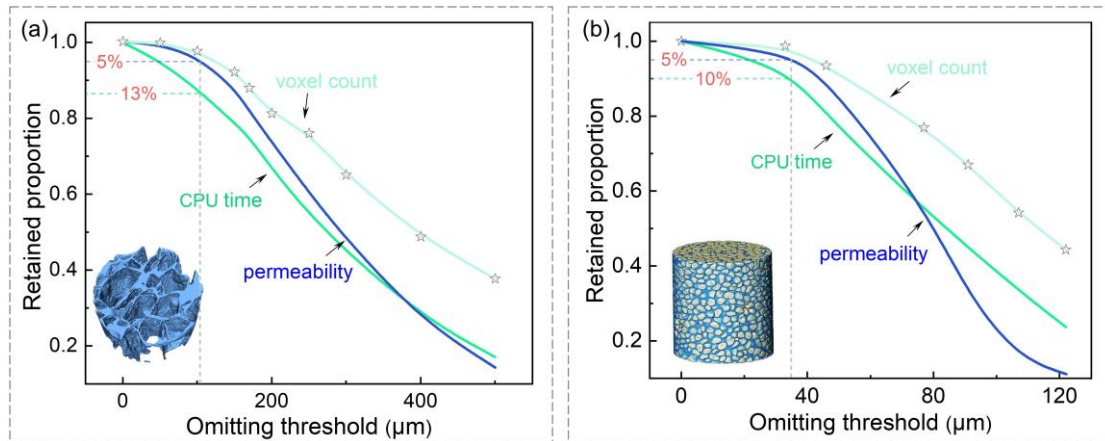
531

532 **Figure 9.** Comparison of simulation results before and after the coral pore structure  
 533 simplification. (a, d) Original and simplified simulation models. The black phase  
 534 represents the coral skeleton. (b, e) The longitudinal section of streamline distribution.  
 535 (c, f) Overall streamline distribution in 3D. (g) Workflow of coral pore structure  
 536 simplification. (h) Flow velocities pre- and post-simplification (plotted as blue and red  
 537 dots) at three selected regions (labeled I, II, and III).

538 The same fluid flow conditions are applied to both the original and simplified  
 539 models. Simulation results of the simplified model preserve fluid flow channels  
 540 (Figures 9b, e) and present clearer streamlines (Figures 9c, f). Overall, the absence of  
 541 tiny pores slightly changes the absolute velocity (less than 5% for the average flow  
 542 velocity: 1.1%, 2.5%, and 5% for regions I, II, and III) and flow paths (which are

543 more aligned with branch boundaries), and the flow velocity distribution remains  
 544 consistent with the original model (Figure 9h). The effect of simplification on the flow  
 545 field outside the coral is even less as the velocity profile at the top in Figure 9h pre-  
 546 and post- simplification almost overlap with each other.

547 Taking the rock sample in Figure 6 as an example, fractures narrower than a  
 548 certain threshold value are hidden and then the permeability of the remaining fracture  
 549 structure and the computation time are calculated with COMSOL. As the omitting  
 550 threshold increases, more fractures are neglected in the simulation, therefore, the  
 551 retained permeability, voxel count, and CPU time all decrease. The effect of these  
 552 filtered fractures on the overall permeability is equivalent to the reduction ratio of  
 553 overall permeability, and the results are shown in Figure 10. The fractures below 100  
 554  $\mu\text{m}$  have little effect on the overall permeability, and then the permeability sharply  
 555 decreases with the increasing threshold value. Another sand specimen (Figure 10b) is  
 556 used to verify this approach (more details about this specimen are given in Text S9 in  
 557 Supporting Information). When a threshold value smaller than 33  $\mu\text{m}$  is applied, the  
 558 reduction in overall permeability is less than 3%.



559

560 **Figure 10.** Retained proportion of permeability, surface area, and voxel count over  
 561 the total while omitting pores smaller than a certain threshold, as well as the  
 562 corresponding CPU time ratio over the case with the original pore structure. (a) Rock  
 563 sample. (b) Saturated sand specimen.

564 The voxel count and surface area of the pore structure are correlated to the  
565 complexity of the mesh and computational cost. It is reported that there is an  
566 approximate power law relationship between CPU time and the number of finite  
567 elements, with an exponent larger than 1.5 (Erhel et al., 2009). Here, voxelized  
568 models are applied for permeability simulation. Consequently, the computation time  
569 obtained (dark green line) shows a direct correlation with voxel count (light green  
570 line), following a quadratic function with an exponent of about 2. If we regard a 5%  
571 permeability loss as acceptable, the CPU time can be reduced by 13% and 10% for the  
572 rock and sand cases, respectively. This reduction in computational time works for both  
573 samples. Therefore, fractures with low contributions (100 and 35  $\mu\text{m}$  for the specific  
574 rock and sand specimens) can be identified in advance with our method to simplify  
575 the fracture structures during simulation modeling and further enhance computational  
576 efficiency.

577 Simply neglecting smaller pores can cause problems in multiphase flow in  
578 porous media, since the neglected pores could be occupied by the wetting phase. On  
579 the other hand, we could consider the smaller pores and the simplified pore structure  
580 separately. For example, in a capillarity regime, we could assume that the wetting  
581 phase is stuck in the small pores and not sensitive to the pressure gradient, while still  
582 responding to other physical processes such as diffusion.

## 583 **5. Conclusions**

584 This study proposes a cost-effective method for simultaneously demonstrating  
585 heterogeneity and anisotropy based on geometry and image analyses.

586 The heterogeneity of porous media is characterized by measuring pore size in CT  
587 images, and the anisotropy is determined using principal component analysis. Then a  
588 simultaneous visualization of both the orientation-based anisotropy and the size-based  
589 heterogeneity is generated by rendering the pore structure surface using color and  
590 color brightness. This visualization preserves the morphology and spatial location of  
591 pore structure, which enables interactive exploration of the spatial relationships

592 between individual pores. Furthermore, we propose a refined stereographic projection  
593 to statistically display both anisotropy (orientation) and heterogeneity (size) in one  
594 plot.

595 The proposed method facilitates our understanding of heterogeneity and  
596 anisotropy within the porous media, and a general trend for size-related physical  
597 behavior can be predicted with the visualization results. We then propose a method of  
598 geometrical model simplification for the numerical simulation, specifically, by  
599 discarding tiny pores with low contribution to property while retaining the major  
600 contributing structures. The simplified models yield a good match with the original  
601 model but significantly reduce the computational cost.

## 602 **Acknowledgments**

603 This work is supported by Research Center for Industries of the Future (RCIF),  
604 Westlake Education Foundation, and Open Research Fund of State Key Laboratory of  
605 Geomechanics and Geotechnical Engineering, Institute of Rock and Soil Mechanics,  
606 Chinese Academy of Sciences (Grant No. SKLGME021008). We thank Westlake  
607 Center for Micro/Nano Fabrication for the facility support and technical assistance.

## 608 **Open Research**

609 The CT image data and corresponding image processing results in this study are  
610 available at Tian (2023) in Mendeley Data via <https://doi.org/10.17632/6ypbv8gbcp.1>.  
611 The code associated to this work is archived and published as Yin (2023) in Mendeley  
612 Data via <https://doi.org/10.17632/rbgwgc2yv9.1>, which can be accessed freely after  
613 registration. The LBM simulation and the corresponding model were described in  
614 MechSys (2021): Multi-physics Simulation Library and Galindo-Torres (2013). The  
615 software can be obtained from <http://mechsys.nongnu.org/>.

616 **References**

- 617 Anderson, M. W., Gebbie-Rayet, J. T., Hill, A. R., Farida, N., Attfield, M. P.,  
618 Cubillas, P., et al. (2017). Predicting crystal growth via a unified kinetic  
619 three-dimensional partition model. *Nature*, *544*, 456–459.  
620 <https://doi.org/10.1038/nature21684>
- 621 Anderson, T. W. (1963). Asymptotic theory for principal component analysis. *Annals*  
622 *of mathematical statistics*, *34*(1), 122–148.  
623 <https://doi.org/10.1214/aoms/1177704248>
- 624 Bang, B., & Lukkassen, D. (1999). Application of homogenization theory related to  
625 Stokes flow in porous media. *Application of Mathematics*, *44*(4), 309–319.  
626 <https://doi.org/10.1023/A:1023084614058>
- 627 Berg, S., Kutra, D., Kroeger, T., Straehle, C. N., Kausler, B. X., Haubold, C., et al.  
628 (2019). ilastik: interactive machine learning for (bio) image analysis. *Nature*  
629 *Methods*, *16*, 1226–1232. <https://doi.org/10.1038/s41592-019-0582-9>
- 630 Budinger, T. F., & Lauterbur, P. C. (1984). Nuclear magnetic resonance technology  
631 for medical studies. *Science*, *226*, 288–298.  
632 <http://dx.doi.org/10.1126/science.6385252>
- 633 Bultreys, T., Van Hoorebeke, L., & Cnudde, V. (2016). Simulating secondary  
634 waterflooding in heterogeneous rocks with variable wettability using an  
635 image-based, multiscale pore network model. *Water Resources Research*, *52*(9),  
636 6833–6850. <https://doi.org/10.1002/2016WR018950>
- 637 Chandra, R., Dagum, L., Kohr, D., Menon, R., Maydan, D., & McDonald, J. (2001).  
638 Parallel programming in OpenMP. San Francisco, Morgan Kaufmann Publishers  
639 Inc.
- 640 Chen, J., Yang, S., Mei, Q., Chen, J., Chen, H., Zou, C., et al. (2021). Influence of  
641 pore structure on gas flow and recovery in ultradeep carbonate gas reservoirs at  
642 multiple scales. *Energy & Fuels*, *35*(5), 3951–3971.  
643 <https://doi.org/10.1021/acs.energyfuels.0c04178>

- 644 Chong, Z., Li, X., Chen, X., Zhang, J., & Lu, J. (2017). Numerical investigation into  
 645 the effect of natural fracture density on hydraulic fracture network propagation.  
 646 *Energies*, *10*, 914. <https://doi.org/10.3390/en10070914>
- 647 Degu, A. M., & Hossain, F. (2012). Investigating the mesoscale impact of artificial  
 648 reservoirs on frequency of rain during growing season. *Water Resources*  
 649 *Research*, *48*(5), W25510. <https://doi.org/10.1029/2011WR010966>
- 650 Erhel, J., De Dreuzy, J. R., & Poirriez, B. (2009). Flow simulation in  
 651 three-dimensional discrete fracture networks. *SIAM Journal on Scientific*  
 652 *Computing*, *31*(4), 2688–2705. <https://doi.org/10.1137/080729244>
- 653 Fatt, I. (1956). The network model of porous media I. Capillary pressure  
 654 characteristics. *Transaction of the AIME*, *207*(1), 144 – 159.  
 655 <https://doi.org/10.2118/574-G>
- 656 Fedorov, A., Beichel, R., Kalpathy-Cramer, J., Fine, J., Fillion-Robin, J., Pujol, S., et  
 657 al. (2012). 3D Slicer as an Image Computing Platform for the Quantitative  
 658 Imaging Network. *Magnetic Resonance Imaging*, *30*(9), 1323–1341.  
 659 <https://doi.org/10.1016/j.mri.2012.05.001>
- 660 Ferreira, A. A. S., & Nick, H. M. (2023). Computed-tomography-based discrete  
 661 fracture-matrix modeling: An integrated framework for deriving fracture  
 662 networks. *Advances in Water Resources*, *177*, 104450.  
 663 <https://doi.org/10.1016/j.advwatres.2023.104450>
- 664 Flannery, B. P., Deckman, H. W., Roberge, W. G., & D’Amico, K. L. (1987).  
 665 Three-dimensional X-ray microtomography. *Science*, *237*, 1439–1444.  
 666 <http://dx.doi.org/10.1126/science.237.4821.1439>
- 667 Galindo-Torres, S. A., Scheuermann, A., & Li, L. (2012). Numerical study on the  
 668 permeability in a tensorial form for laminar flow in anisotropic porous media.  
 669 *Physical Review E*, *86*, 046306. <https://doi.org/10.1103/PhysRevE.86.046306>
- 670 Galindo-Torres, S. A. (2013). A coupled discrete element lattice Boltzmann method  
 671 for the simulation of fluid-solid interaction with particles of general shapes.

- 672 *Computer Methods in Applied Mechanics and Engineering*, 265, 107–119.  
673 <https://doi.org/10.1016/j.cma.2013.06.004>
- 674 Grau, S., Verges, E., Tost, D., & Ayala, D. (2010). Exploration of porous structures  
675 with illustrative visualizations. *Computers & Graphics-UK*, 34(4), 398–408.  
676 <http://dx.doi.org/10.1016/j.cag.2010.05.001>
- 677 Grevera, G.J. (2007). Distance transform algorithms and their implementation and  
678 evaluation. *Deformable Models: Biomedical and Clinical Applications*, Springer  
679 New York, New York, NY, 33–60.
- 680 Hilderand, T., & Ruegsegger, P. (1997). A new method for the model-independent  
681 assessment of thickness in three-dimensional images. *Journal of Microscopy*,  
682 185, 67–75. <https://doi.org/10.1046/j.1365-2818.1997.1340694.x>
- 683 Howarth, R. J. (1996). History of the stereographic projection and its early use in  
684 geology. *Terra Nova*, 8(6), 499–513.  
685 <https://doi.org/10.1111/j.1365-3121.1996.tb00779.x>
- 686 Hunt, A. G., & Sahimi, M. (2017). Flow, transport, and reaction in porous media:  
687 Percolation scaling, critical-path analysis, and effective medium approximation.  
688 *Reviews of Geophysics*, 55, 993–1078. <https://doi.org/10.1002/2017RG000558>
- 689 Hyman, J. D. (2020). Flow channeling in fracture networks: characterizing the effect  
690 of density on preferential flow path formation. *Water Resources Research*, 56(9),  
691 e2020WR027986. <https://doi.org/10.1029/2020WR027986>
- 692 Ihli, J., Jacob, R.R., Holler, M., Guizar-Sicairos, M., Diaz, A., da Silva, J. C., et al.  
693 (2017). A three-dimensional view of structural changes caused by deactivation of  
694 fluid catalytic cracking catalysts. *Nature Communications*, 8, 809.  
695 <https://doi.org/10.1038/s41467-017-00789-w>
- 696 Jiang, Z., van Dijke, M. I. J., Geiger, S., Ma, J., Couples, G. D., & Li, X. (2017). Pore  
697 network extraction for fractured porous media. *Advances in Water Resources*,  
698 107, 280–289. <https://doi.org/10.1016/j.advwatres.2017.06.025>

- 699 Jiang, Z., van Dijke, M. I. J., Sorbie, K. S., & Couples, G. D. (2013). Representation  
700 of multiscale heterogeneity via multiscale pore networks. *Water Resources*  
701 *Research*, 49(9), 5437–5449. <https://doi.org/10.1002/wrcr.20304>
- 702 Jing, Y., Armstrong, R. T., & Mostaghimi, P. (2020). Image-based fracture pipe  
703 network modelling for prediction of coal permeability. *Fuel*, 270(15), 117447.  
704 <https://doi.org/10.1016/j.fuel.2020.117447>
- 705 Johnson, G. R., Gupta, K., Putz, D. K., Hu, Q., & Brusseau, M.L. (2003). The effect  
706 of local-scale physical heterogeneity and nonlinear, rate-limited  
707 sorption/desorption on contaminant transport in porous media. *Journal of*  
708 *Contaminant Hydrology*, 64(1-2), 35–58.  
709 [https://doi.org/10.1016/S0169-7722\(02\)00103-1](https://doi.org/10.1016/S0169-7722(02)00103-1)
- 710 Lee, T., Kashyap, R., & Chu, R. (1994). Building skeleton models via 3-D medial  
711 surface axis thinning algorithms. *CVGIP: Graphical Models and Image*  
712 *Processing*, 55(6), 462-478. <https://doi.org/10.1006/cgip.1994.1042>
- 713 Li, Y., Liao, X., He, C., & Lu, Z. (2021). Calcium transport along the axial canal in  
714 Acropora. *Diversity*, 13(9), 407. <https://doi.org/10.3390/d13090407>
- 715 Lyu, Q.F., Wu, H., & Li, X. (2021). A 3D model reflecting the dynamic generating  
716 process of pore networks for geological porous media. *Computers and*  
717 *Geotechnics*, 140, 104444. <https://doi.org/10.1016/j.compgeo.2021.104444>
- 718 Mahabadi, N., Zheng, X., Yun, T. S., van Paassen, L., & Jang, J. (2018). Gas bubble  
719 migration and trapping in porous media: pore-scale simulation. *Journal of*  
720 *Geophysical Research: Solid Earth*, 123(2), 1060–1071.  
721 <https://doi.org/10.1002/2017JB015331>
- 722 Martin-Garin, B., Lathuilière, B., Verrecchia, E. P., & Geister, J. (2007). Use of  
723 fractal dimensions to quantify coral shape. *Coral Reefs*, 26, 541–550.  
724 <https://doi.org/10.1007/s00338-007-0256-4>
- 725 Merchant, F. A., Shah, S. K., & Castleman, K. R. (2023). Chapter Eight-Object  
726 Measurement. *Microscope Image Processing (Second Edition)*, 153–175.  
727 <https://doi.org/10.1016/B978-0-12-821049-9.00017-4>

- 728 Mishurova, T., Léonard, F., Oesch, T., Meinel, D., Bruno, G., Rachmatulin, N., et al.  
729 (2017). *Evaluation of fiber orientation in a composite and its effect on material*  
730 *behavior*. Paper presented at 7th Conference on Industrial Computed  
731 Tomography, Leuven, Belgium.
- 732 Nemati, R., Shahrouzi, J. R., & Alizadeh, R. (2020). A stochastic approach for  
733 predicting tortuosity in porous media via pore network modeling. *Computers and*  
734 *Geotechnics*, 120, 103406. <https://doi.org/10.1016/j.compgeo.2019.103406>
- 735 Nemec, W. (1988). The shape of the rose. *Sedimentary Geology*, 59, 149–152.  
736 [https://doi.org/10.1016/0037-0738\(88\)90105-4](https://doi.org/10.1016/0037-0738(88)90105-4)
- 737 Puyguiraud, A., Gouze, P., & Dentz, M. (2020). Is there a representative elementary  
738 volume for anomalous dispersion? *Transport in Porous Media*, 131(2), 767–778.  
739 <https://doi.org/10.1007/s11242-019-01366-z>
- 740 Qin, X., Cai, J., & Wang, G. (2023). Pore-scale modeling of pore structure properties  
741 and wettability effect on permeability of low-rank coal. *International Journal of*  
742 *Mining Science and Technology*, 33(5), 573–584.  
743 <https://doi.org/10.1016/j.ijmst.2023.02.005>
- 744 Ren, X., & Santamarina, J. C. (2018). The hydraulic conductivity of sediments: Apore  
745 size perspective. *Engineering Geology*, 233(31), 48–54.  
746 <https://doi.org/10.1016/j.enggeo.2017.11.022>
- 747 Robb, K., Wirjadi, O., & Schladitz, K. (2007). *Fiber Orientation Estimation from 3D*  
748 *Image Data: Practical Algorithms, Visualization, and Interpretation*. Paper  
749 presented at 7th International Conference on Hybrid Intelligent Systems,  
750 Kaiserslautern, Germany.
- 751 Schindelin, J., Arganda-Carreras, I., Frise, E., Kaynig, V., Longair, M., Pietzsch, T.,  
752 et al. (2012). Fiji: An Open-Source Platform for Biological-Image Analysis.  
753 *Nature Methods*, 9, 676–682. <https://doi.org/10.1038/nmeth.2019>
- 754 Sebben, M. L., & Werner, A. D. (2016). A modeling investigation of solute transport  
755 in permeable porous media containing a discrete preferential flow feature.

- 756 *Advances in Water Resources*, 94, 307–317.  
757 <https://doi.org/10.1016/j.advwatres.2016.05.022>
- 758 Shahriar, M. F., & Khanal, A. (2023). Effect of formation heterogeneity on CO<sub>2</sub>  
759 dissolution in subsurface porous media. *ACS Earth and Space Chemistry*, 7(10),  
760 2073–2090. <https://doi.org/10.1021/acsearthspacechem.3c00175>.
- 761 Shigorina, E., Rüdiger, F., Tartakovsky, A. M., Sauter, M., & Kordilla, J. (2021).  
762 Multiscale Smoothed Particle Hydrodynamics Model Development for  
763 Simulating Preferential Flow Dynamics in Fractured Porous Media. *Water*  
764 *Resources Research*, 57(3), e2020WR027323.  
765 <https://doi.org/10.1029/2020WR027323>
- 766 Silin, D., & Patzek, T. (2006). Pore space morphology analysis using maximal  
767 inscribed spheres. *Physica A: Statistical Mechanics and its Applications*, 371(2),  
768 336–360. <https://doi.org/10.1016/j.physa.2006.04.048>
- 769 Song, W., Jun, Y., Wang, D., Li, Y., Sun, H., & Yang, Y. (2020). Dynamic pore  
770 network modelling of real gas transport in shale nanopore structure. *Journal of*  
771 *Petroleum Science and Engineering*, 184, 106506.  
772 <https://doi.org/10.1016/j.petrol.2019.106506>
- 773 Van der Walts, S., Schönberger J. L., Nunez-Iglesias J., Boulogne F., Warner J. D.,  
774 Yager N., Gouillart E., & Yu T. (2014). scikit-image: Image processing in  
775 Python Peer J 2:e453. <https://doi.org/10.7717/peerj.453>
- 776 Wang, J., Huang, X., Xu, J. Zhang, Z., Wang, S. F., & Li, Y. (2023). Network  
777 analysis of pore structure of coral reef limestone and its implications for seepage  
778 flow. *Engineering Geology*, 318(5), 107103.  
779 <https://doi.org/10.1016/j.enggeo.2023.107103>
- 780 Weissenbock, J., Amirkhanov, A., Li, W., Reh, A., Amirkhanov, A., Groller, E., et al.  
781 (2014). *FiberScout: An Interactive Tool for Exploring and Analyzing Fiber*  
782 *Reinforced Polymers*. Paper presented at 2014 IEEE Pacific Visualization  
783 Symposium. Yokohama, Japan.

- 784 Wildenschild, D., & Sheppard, A. P. (2012). X-ray imaging and analysis techniques  
785 for quantifying pore-scale structure and processes in subsurface porous medium  
786 systems. *Advances in Water Resources*, *51*, 217–246.  
787 <http://dx.doi.org/10.1016/j.advwatres.2012.07.018>.
- 788 Wittwer, M., & Seita, M. (2022). A machine learning approach to map crystal  
789 orientation by optical microscopy. *npj Computational Materials*, *8*(8).  
790 <https://doi.org/10.1038/s41524-021-00688-1>
- 791 Xu, L., Myers, M., Li, Q., White, C., & Zhang, X. (2020). Migration and storage  
792 characteristics of supercritical CO<sub>2</sub> in anisotropic sandstones with clay  
793 interlayers based on X-CT experiments. *Journal of Hydrology*, *580*, 124239.  
794 <https://doi.org/10.1016/j.jhydrol.2019.124239>
- 795 Yang, Z., Xu, T., Wang, F., Yang, Y., Li, X., & Zhao, N. (2018). Impact of inner  
796 reservoir faults on migration and storage of injected CO<sub>2</sub>. *Internal Journal of*  
797 *Greenhouse Gas Control*, *72*, 14–25. <https://doi.org/10.1016/j.ijggc.2018.03.006>
- 798 Zhang, K., Wang, S., Wang, L., Cheng, Y., Li, W., & Han, X. (2022). 3D  
799 visualization of tectonic coal microstructure and quantitative characterization on  
800 topological connectivity of pore-fracture networks by Micro-CT. *Journal of*  
801 *Petroleum Science and Engineering*, *208*, 109675.  
802 <https://doi.org/10.1016/j.petrol.2021.109675>
- 803 Zhang, Z., Li, C., Ning, F., Liu, L., Cai, J., Liu, C., et al. (2020). Pore Fractal  
804 Characteristics of Hydrate-Bearing Sands and Implications to the Saturated  
805 Water Permeability. *Journal of Geophysical Research: Solid Earth*, *125*(3),  
806 e2019JB018721. <https://doi.org/10.1029/2019JB018721>

Figure 1.

(a)



5 mm

Axial canal

(b)



1 mm

Defect

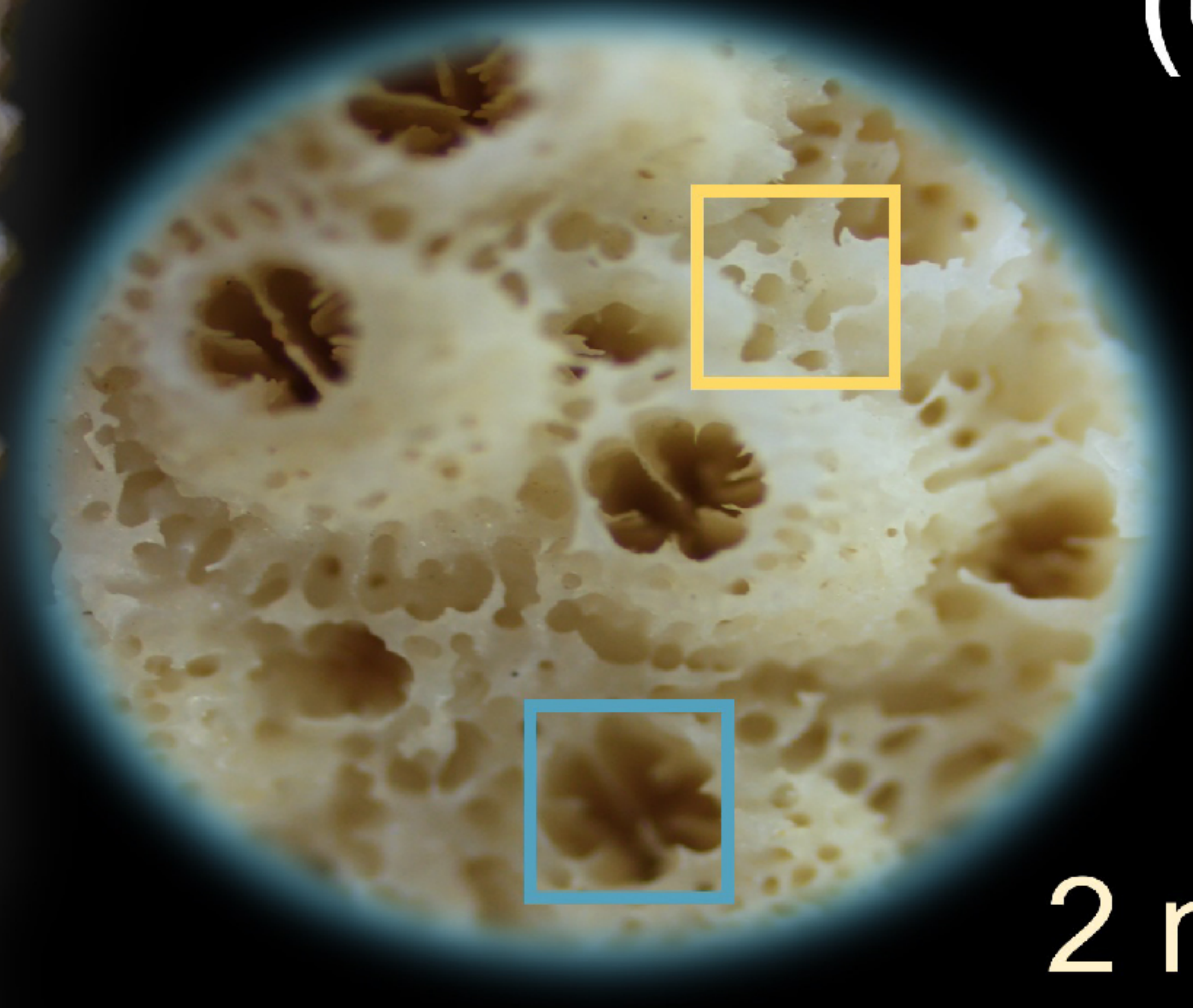
(c)



2 mm

Gastrovascular canal system

(d)

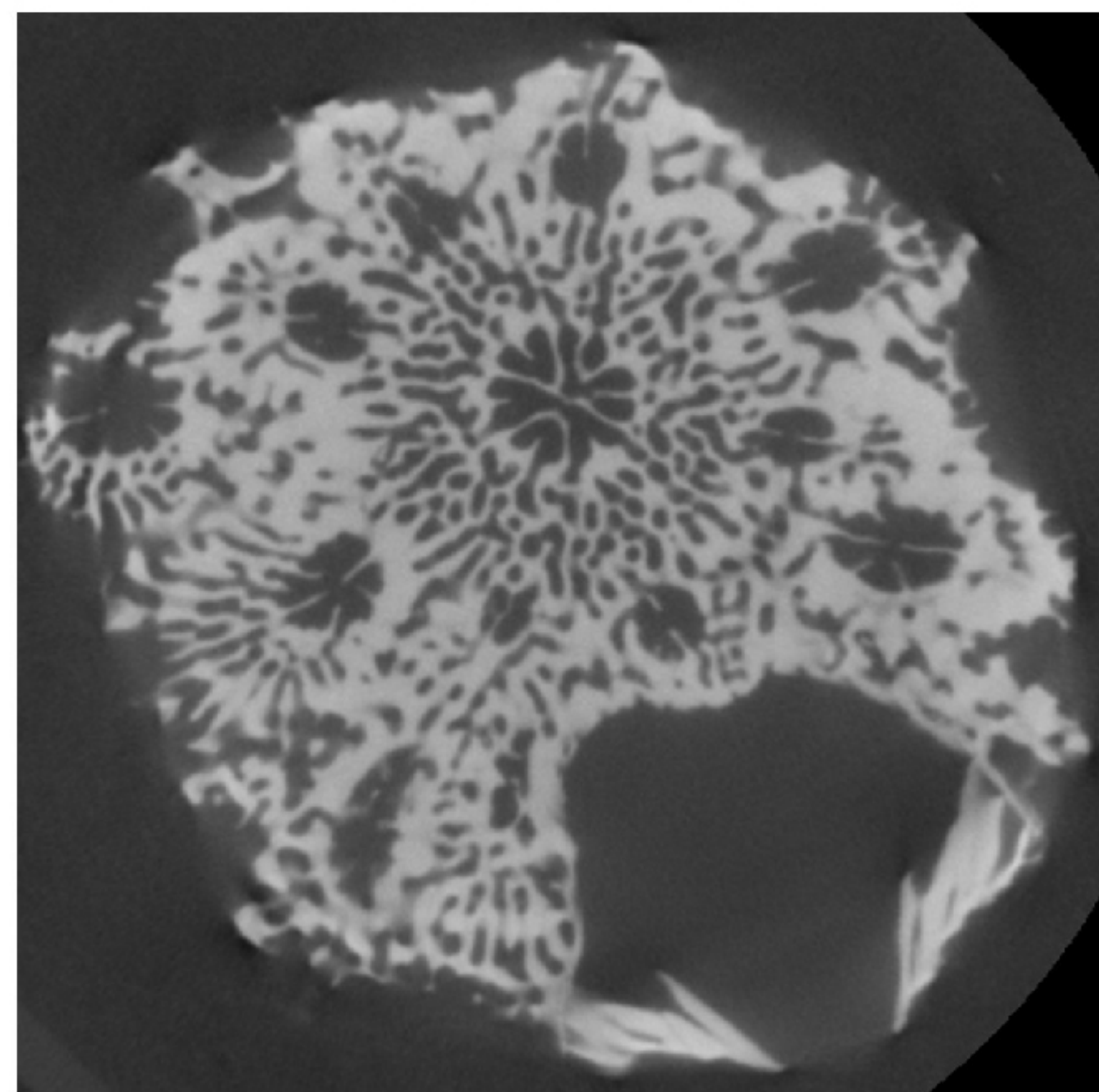


2 mm

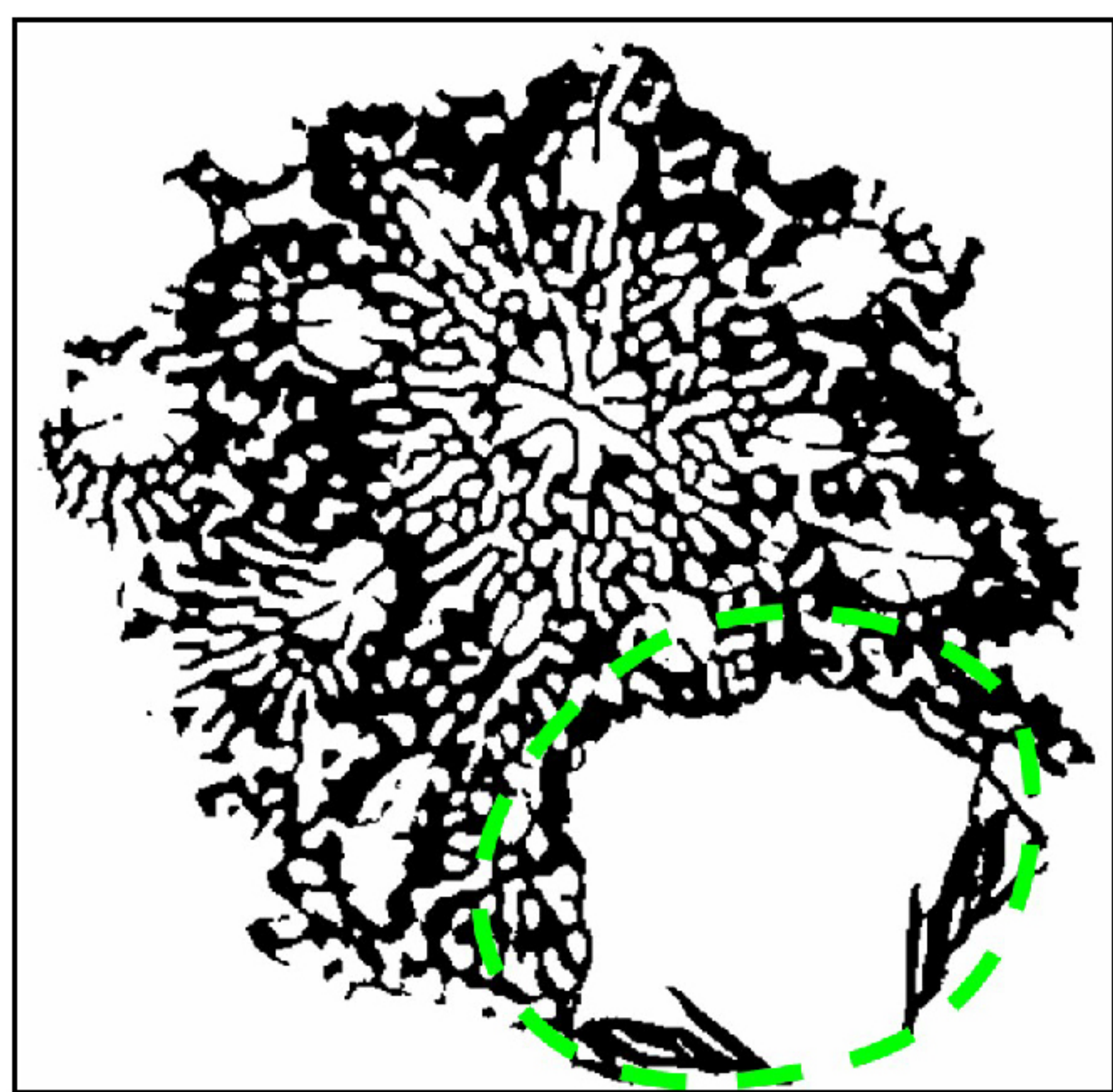
Lumen in calyx

Figure 2.

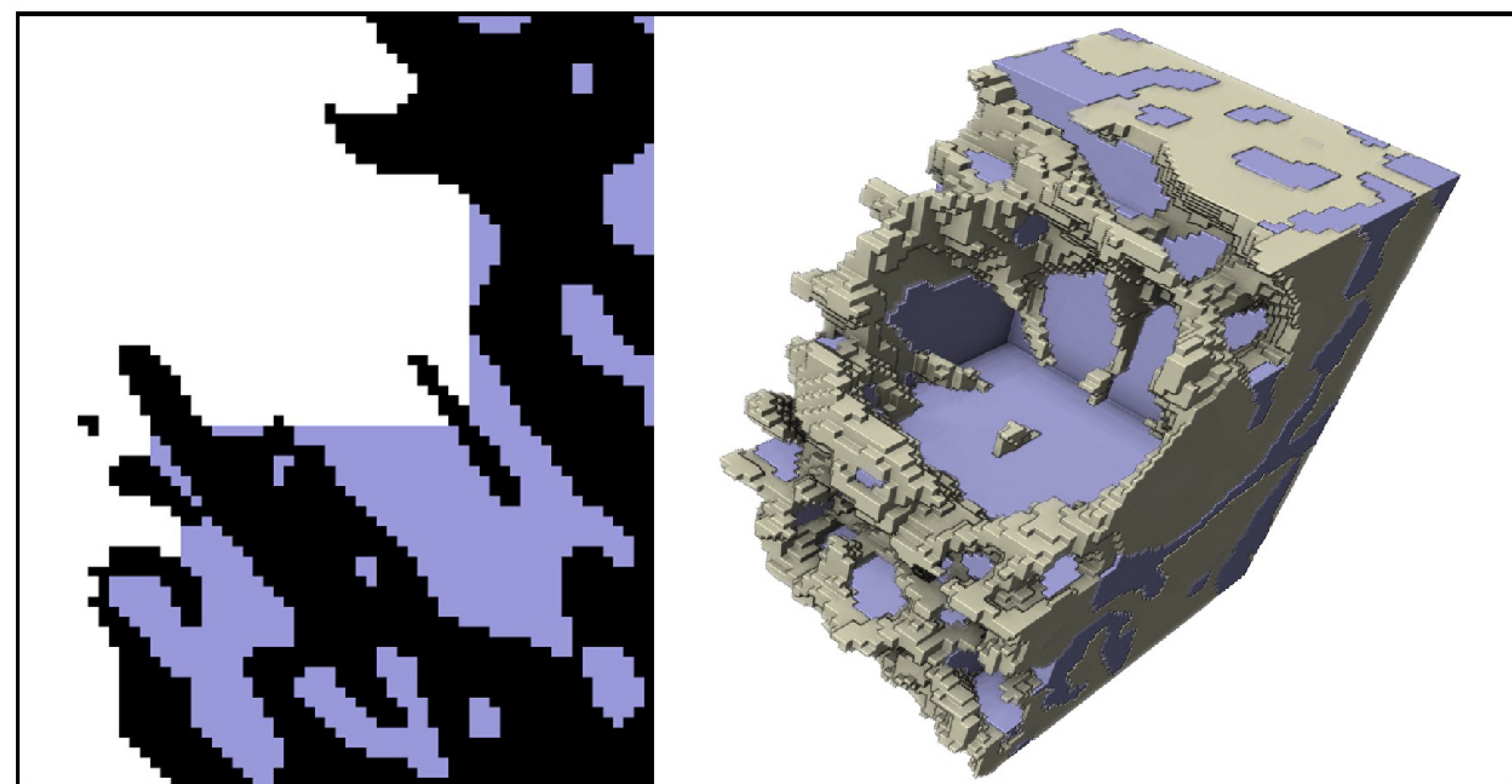
(a) Raw image



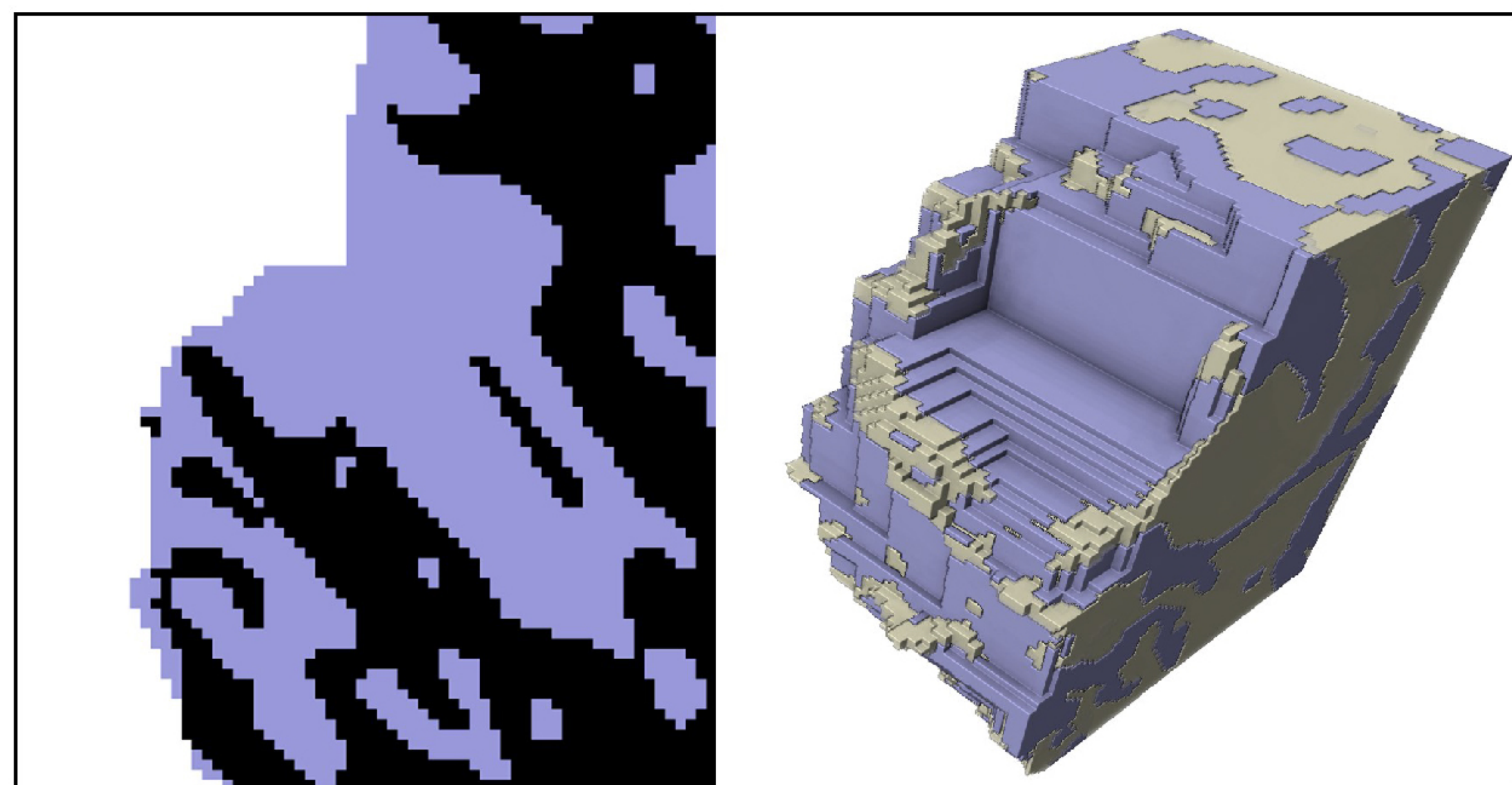
(b) Segmentation



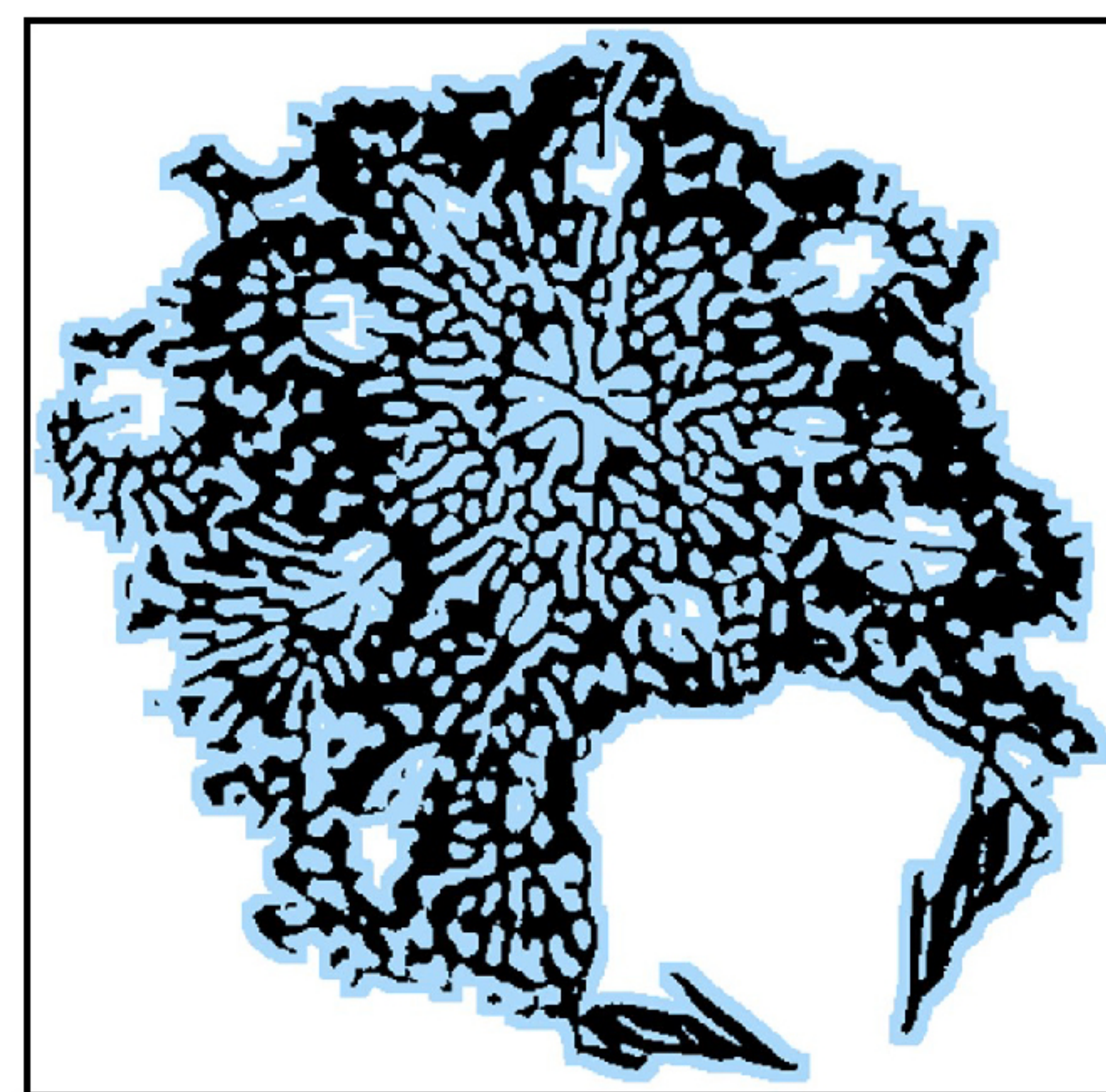
(c) Fill holes



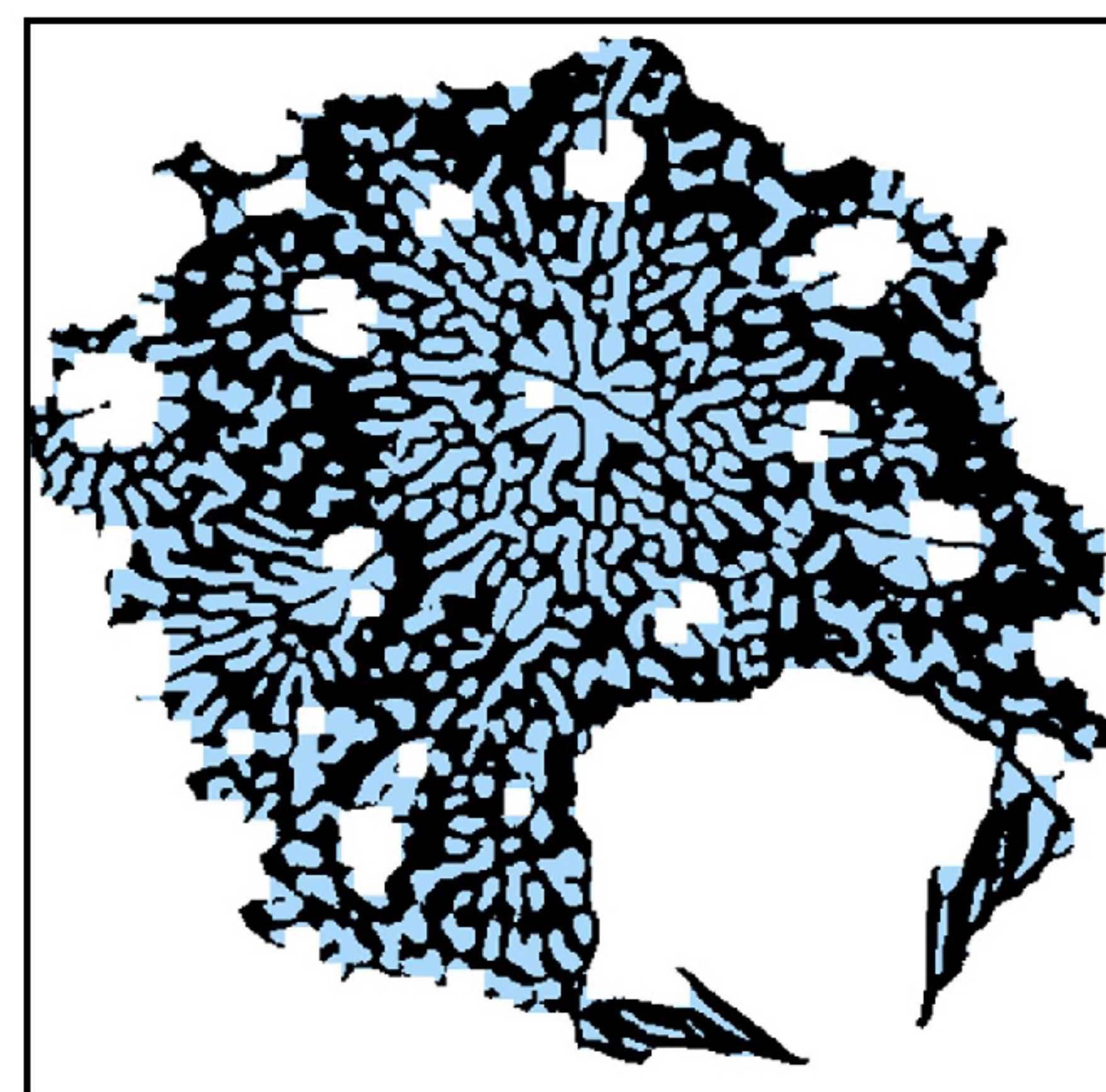
(d) Dilate & erode + fill holes



(e) Dilate

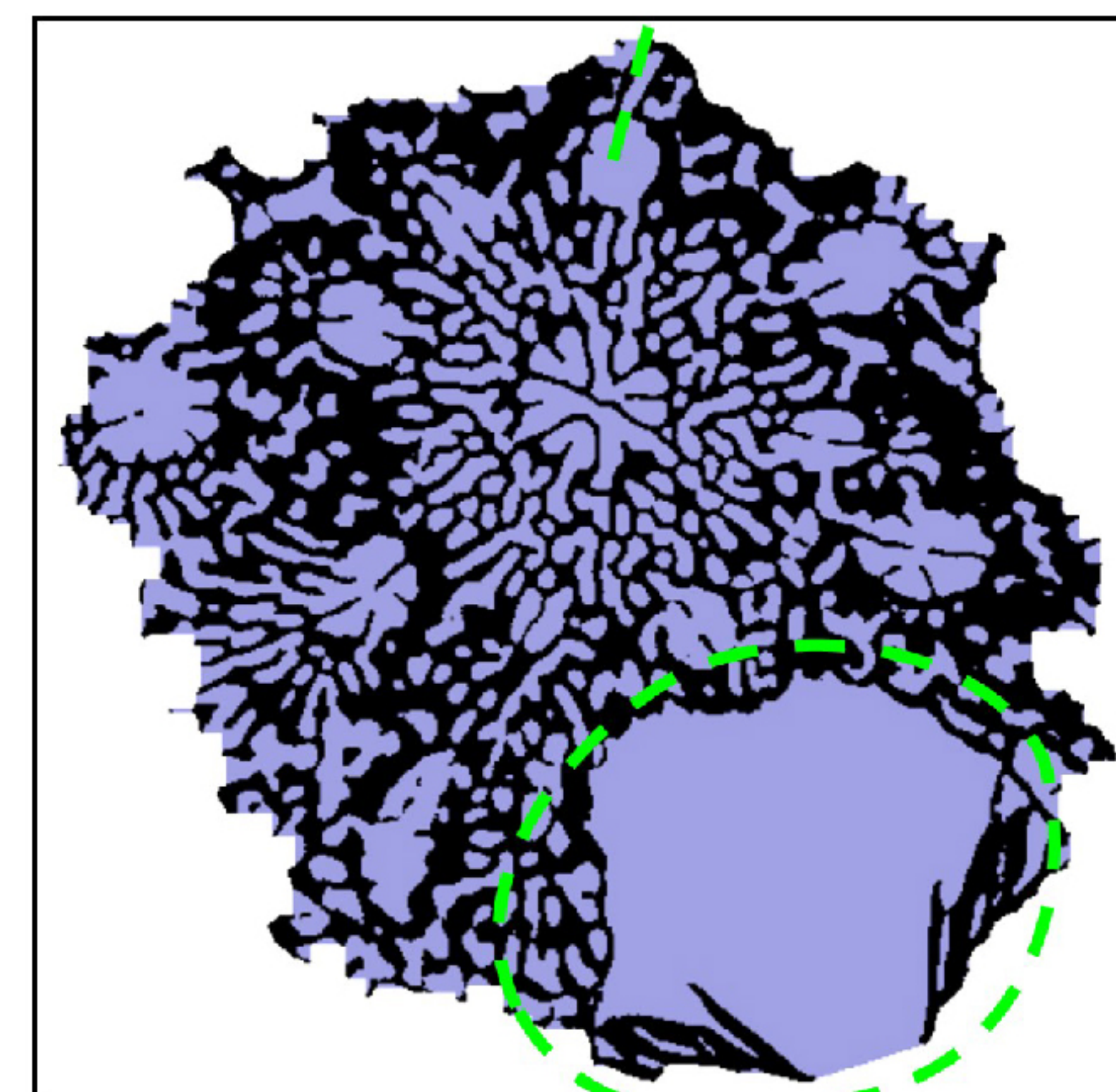


(f) Erode



(g) Isolated pores

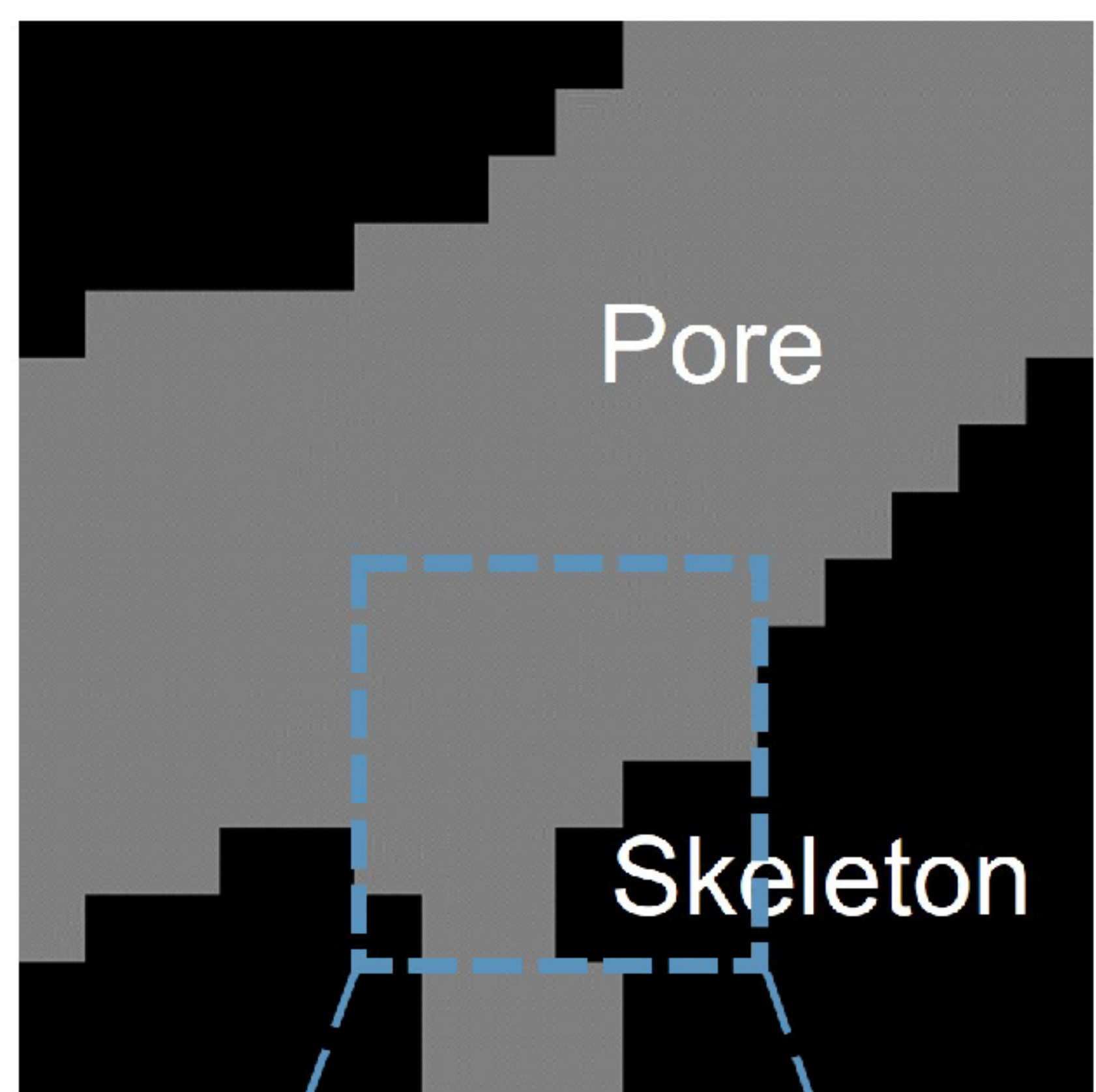
Dilate & Erode  
+ fill hole



Manually closed  
+ fill hole

Figure 3.

(a) Pore structure



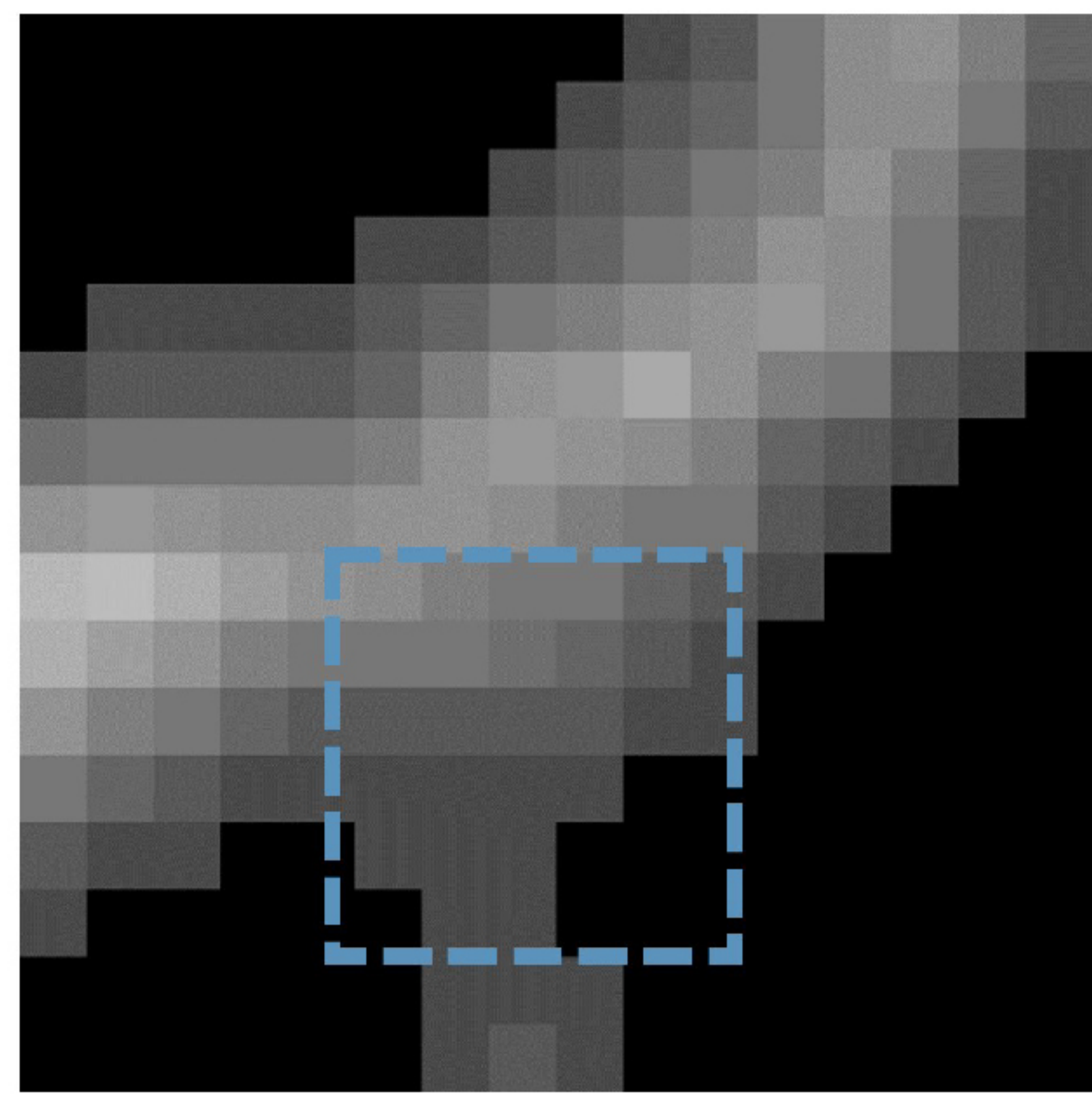
An example

Corresponding voxel

1	1	1	1	1	1
1	1	1	1	1	1
1	1	1	1	1	1
1	1	1	1	0	0
1	1	1	0	0	0
0	1	1	0	0	0

$A_1(a)$

(b) Grayscale distance map

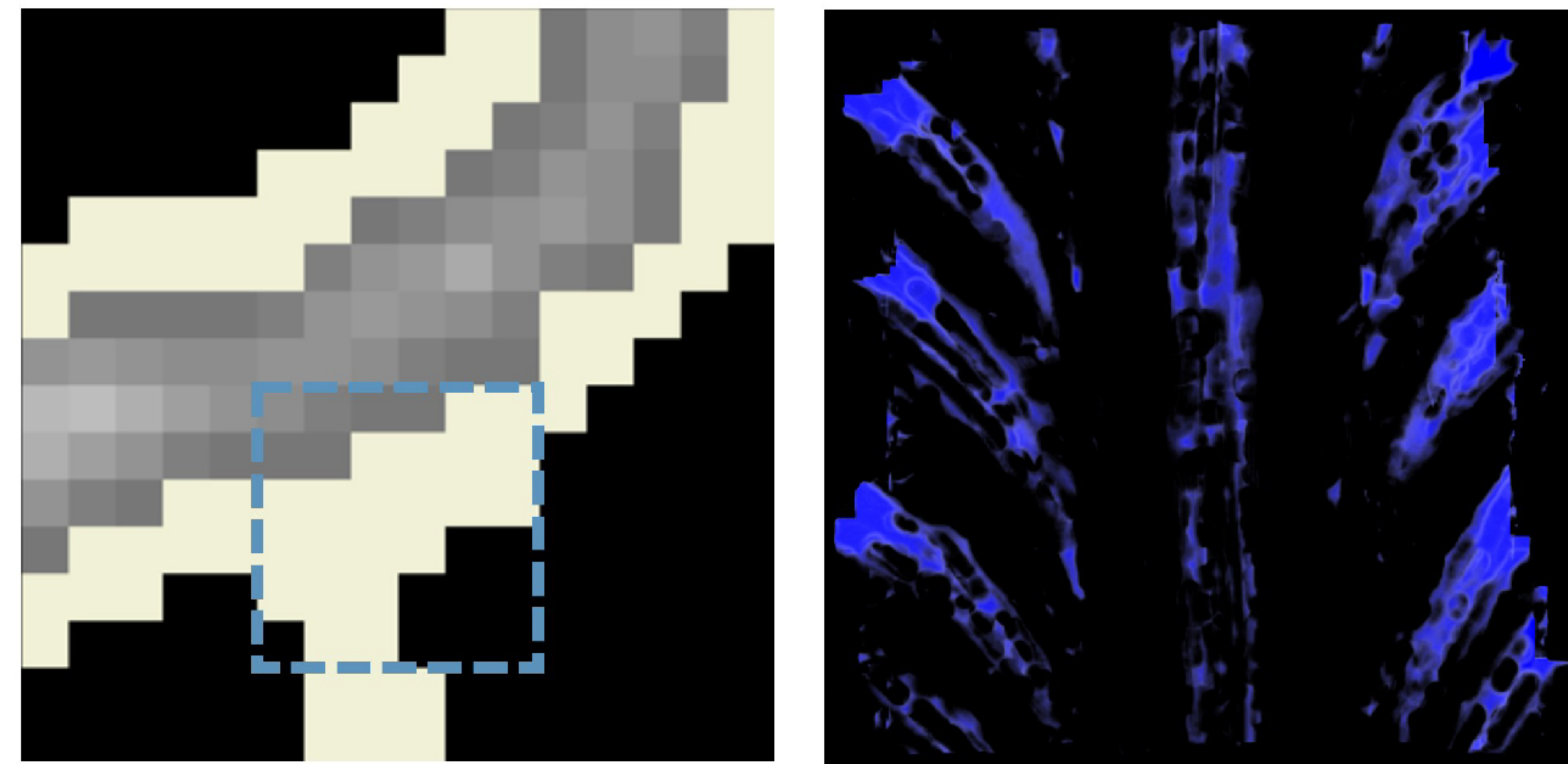


Distance (voxel)

2.8	2.4	2.2	2.2	1.7	1.4
2.2	2.2	2	1.7	1.4	1
1.4	1.4	1.4	1.4	1	1
1	1	1	1	0	0
1	1	1	0	0	0
0	1	1	0	0	0

$A_2(a)$

(d) Visualization



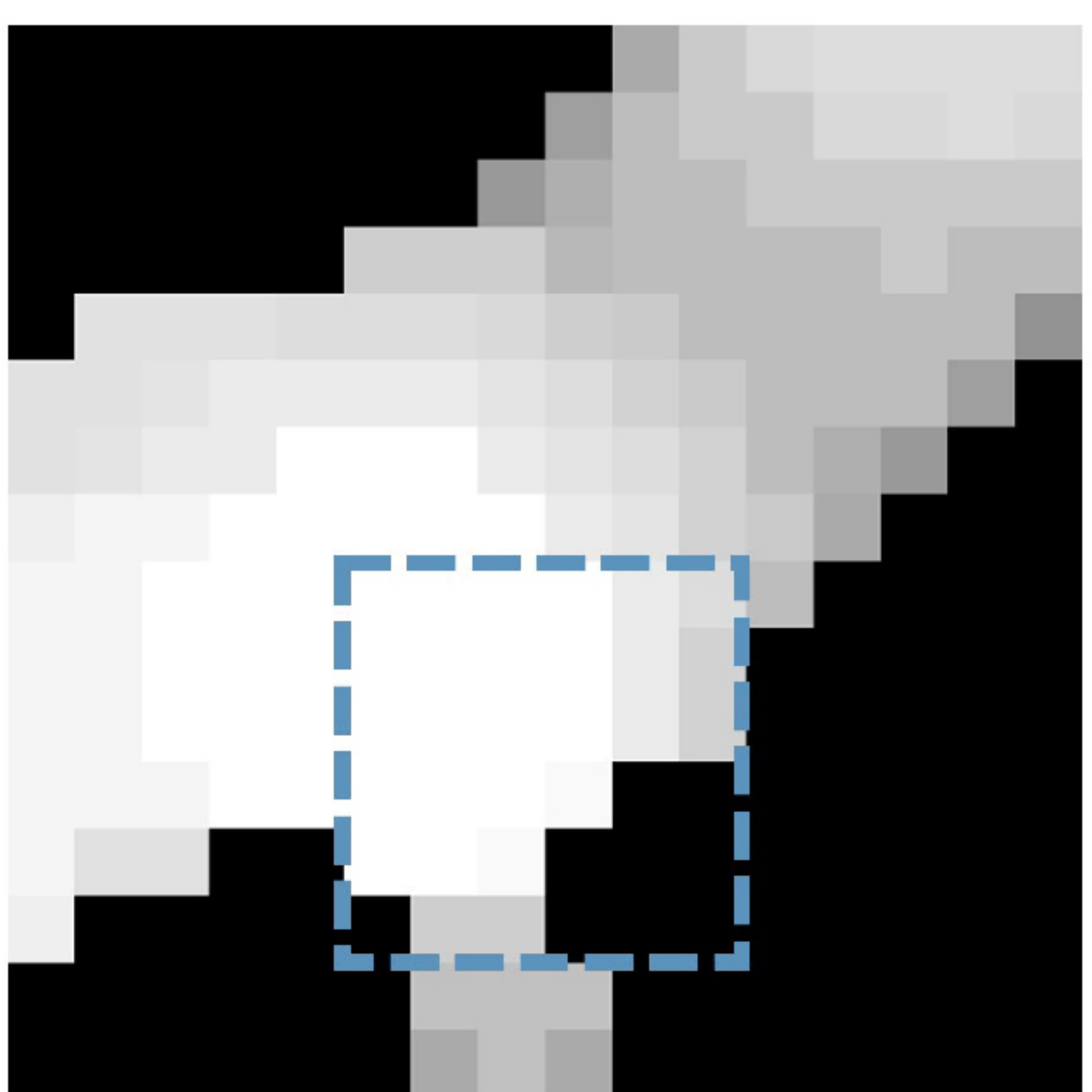
Voxel >2

3D structure

Distance / Size (mm)

0.041  0.8

(c) Grayscale 3D size map

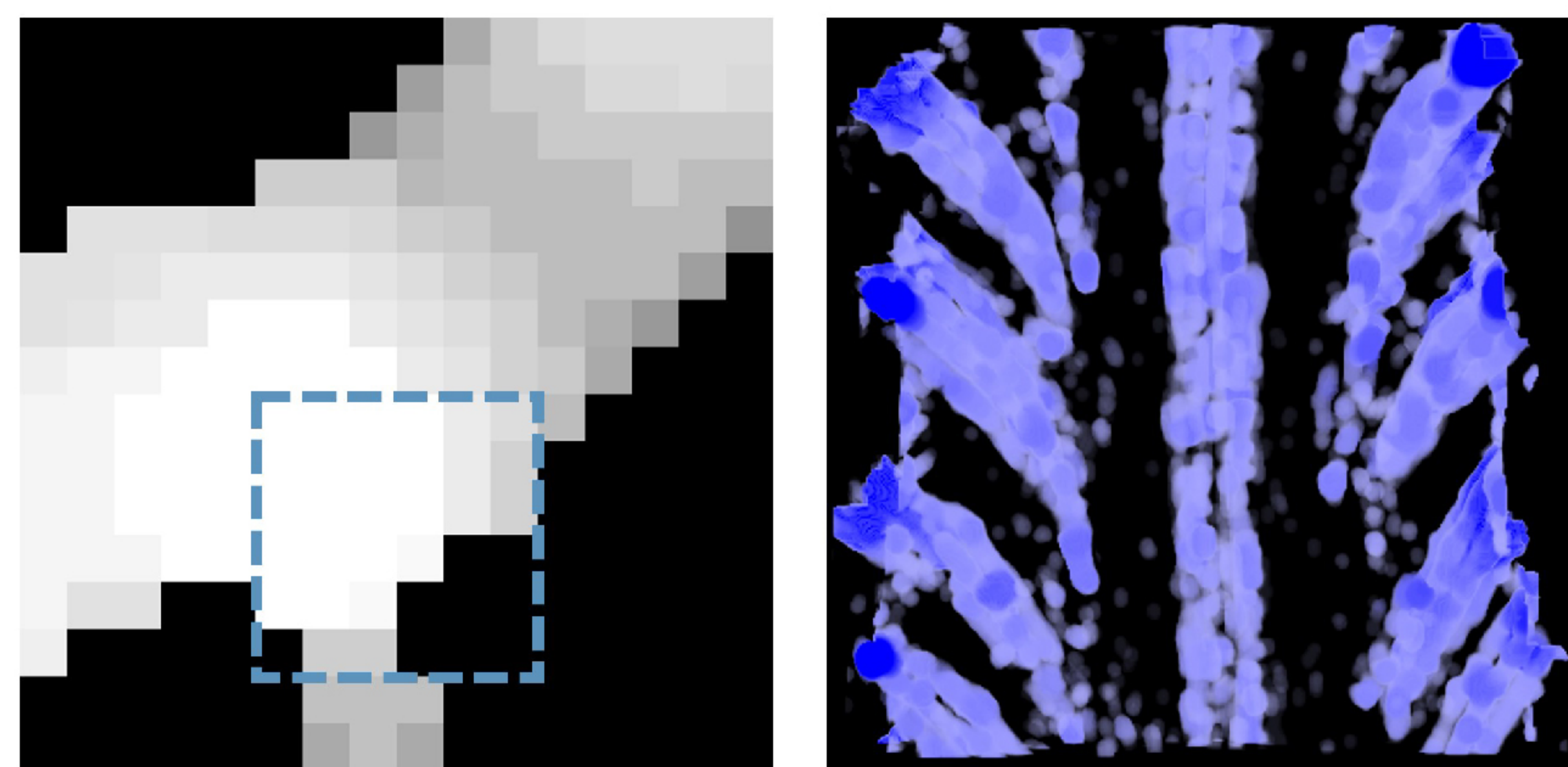


3D size (voxel)

5.9	5.9	5.9	5.9	5.4	5
5.9	5.9	5.9	5.9	5.4	4.7
5.98	5.9	5.9	5.9	5.4	4.7
5.9	5.9	5.9	5.7	0	0
5.9	5.9	5.7	0	0	0
0	4.6	4.6	0	0	0

$A_3(a)$

(e) Visualization



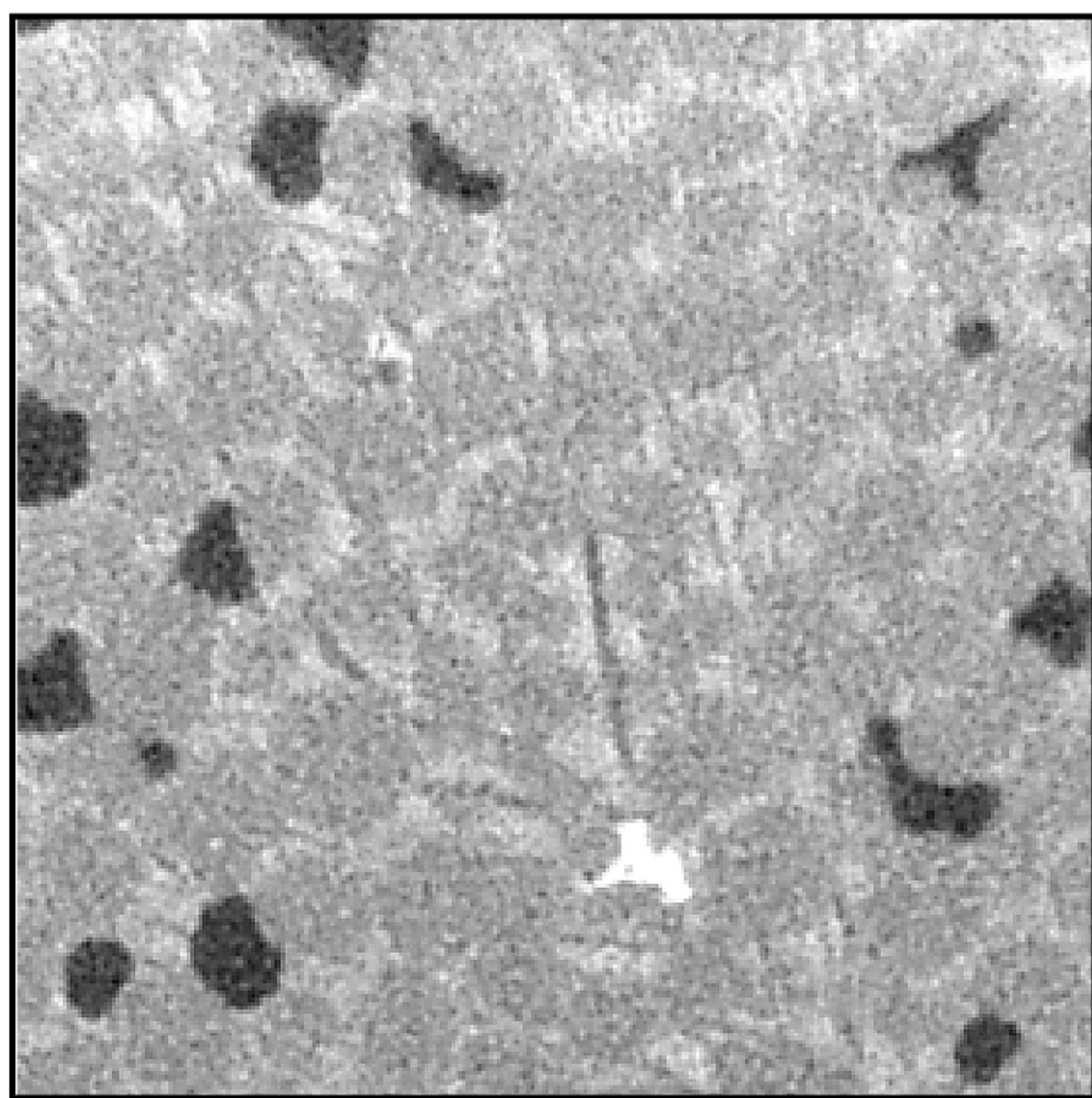
Voxel >2

3D structure

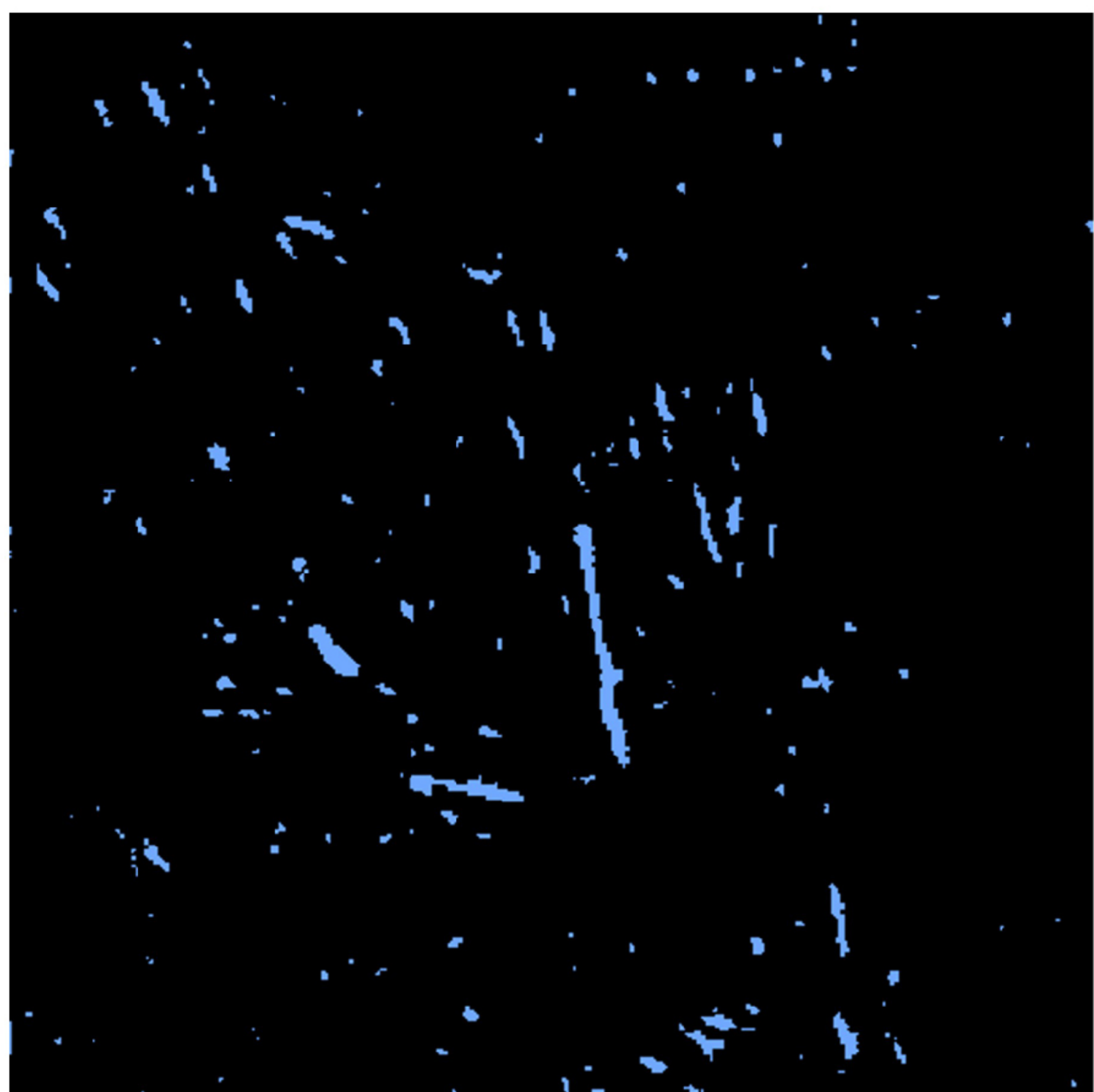
Figure 4.

### (a) Image segmentation

Raw image

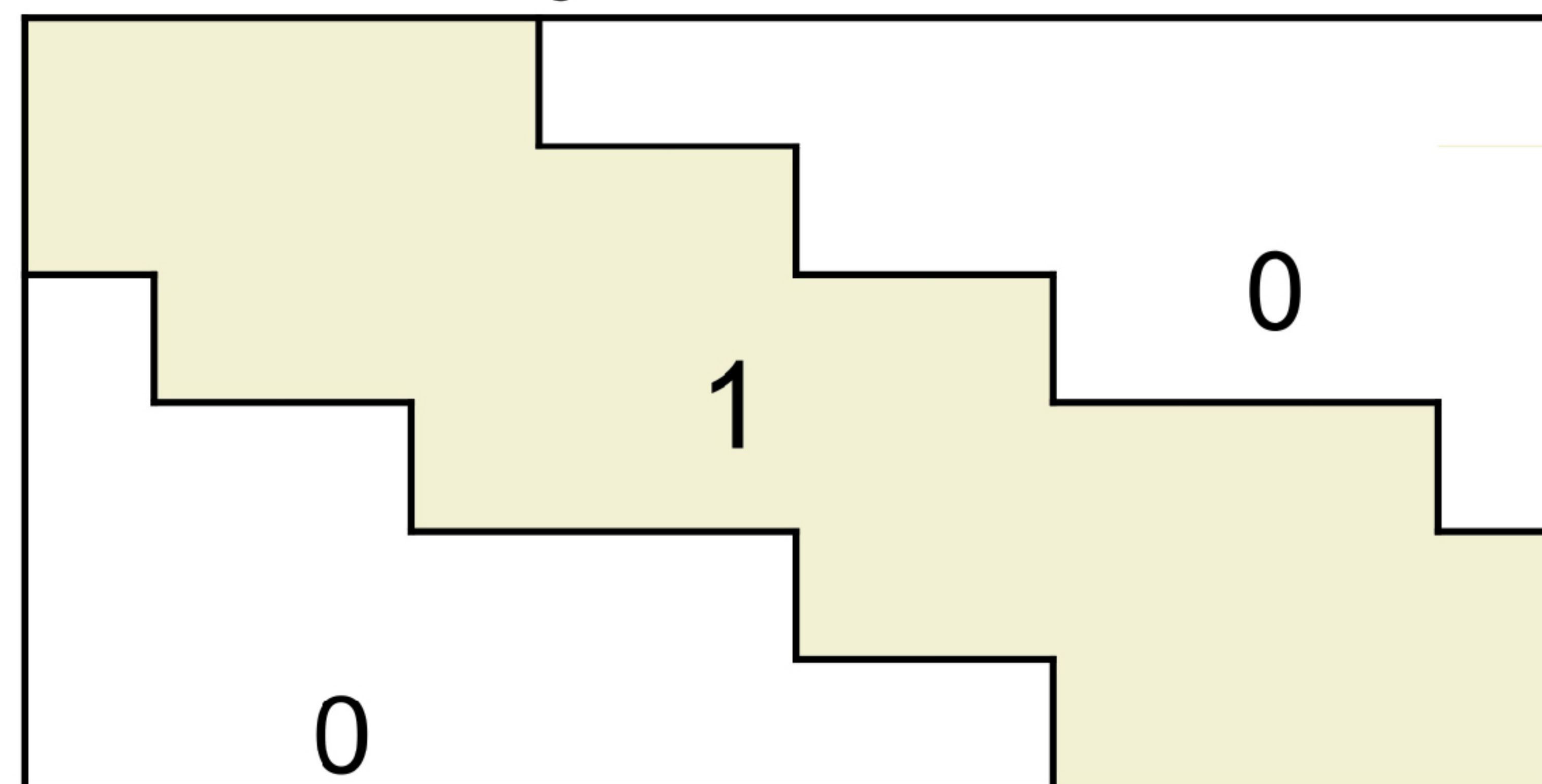


Isolated crystals



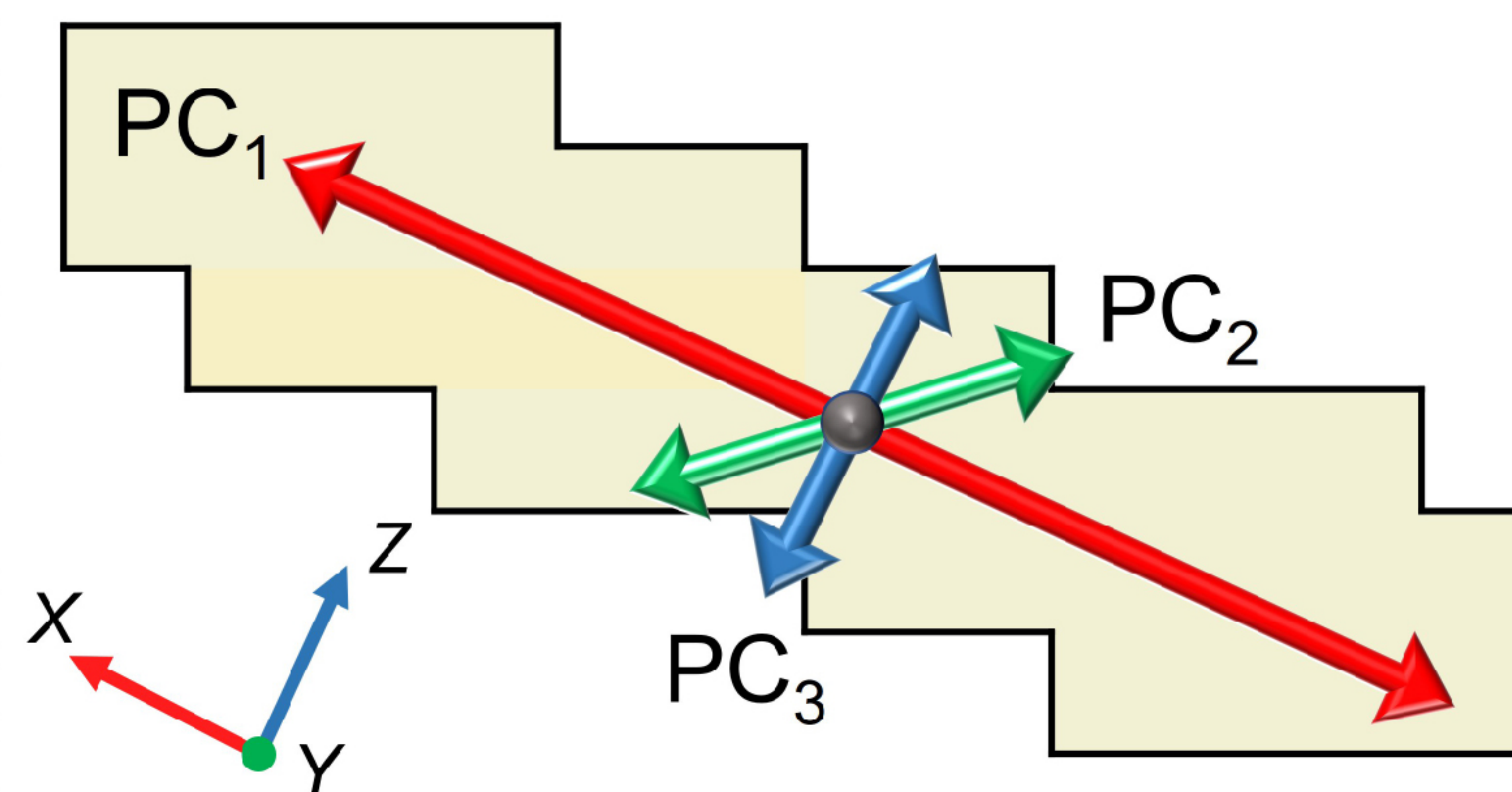
### (b) Orientation extraction

Crystal demo



Crystal voxel values = 1

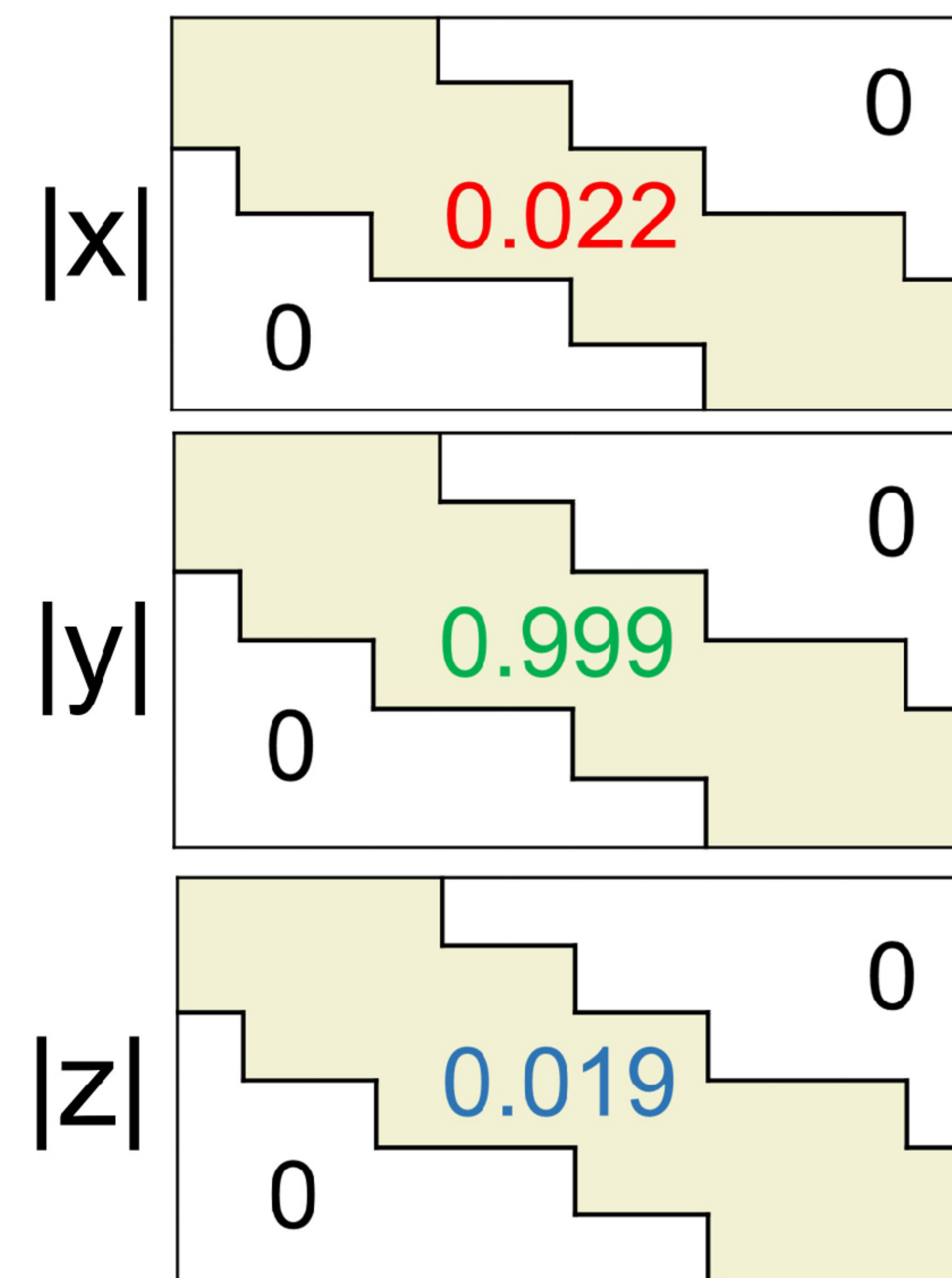
PCA of crystals



PC<sub>3</sub>: (0.022, -0.999, -0.019)

### (c) Color assignment

Voxel assignment

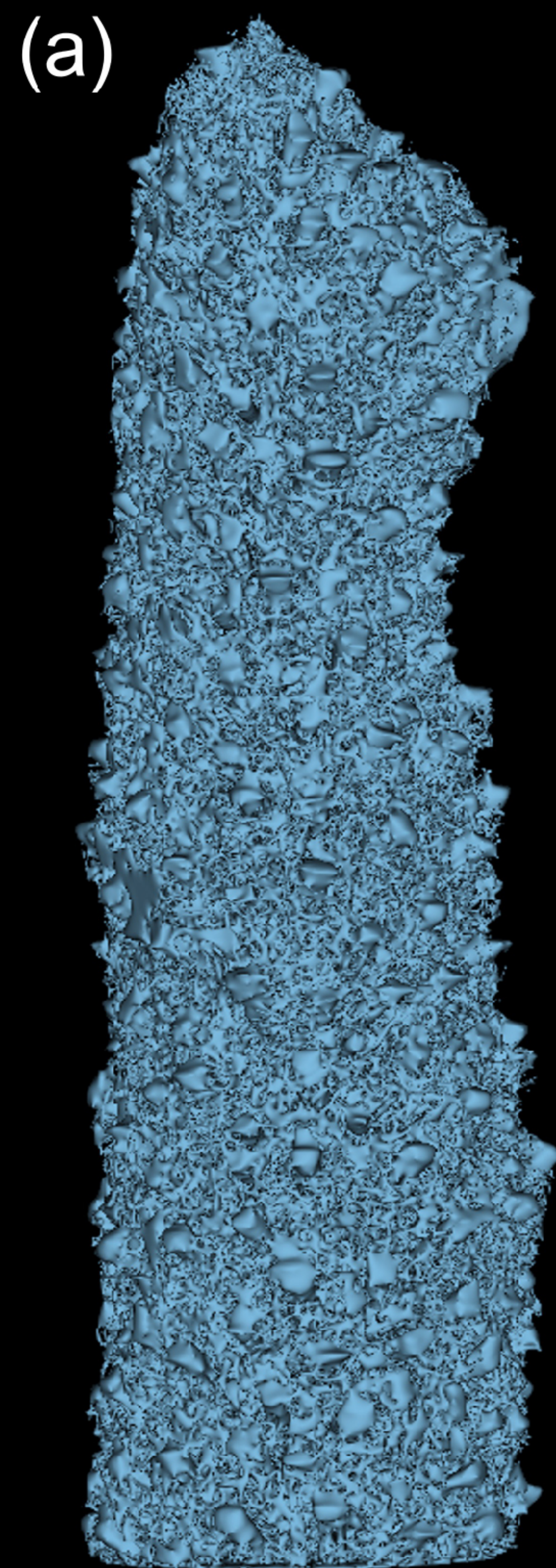


RGB visualization

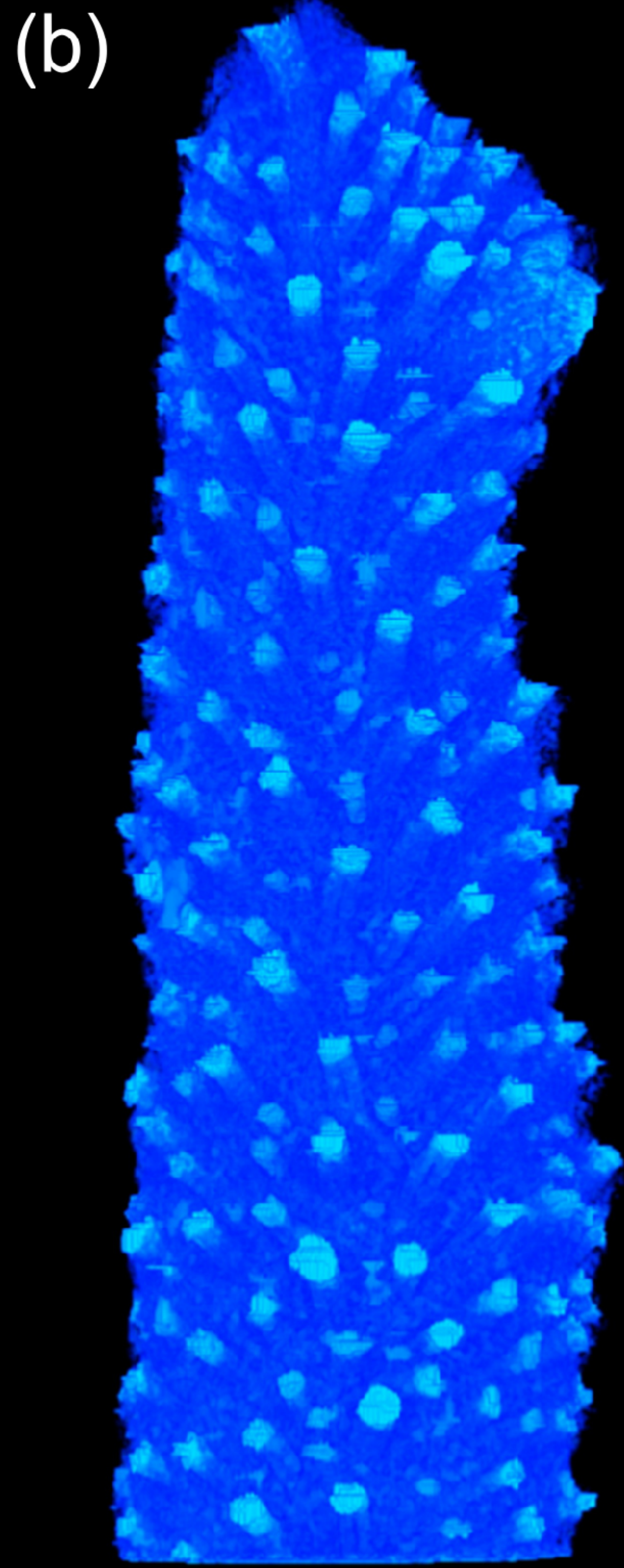
$$\begin{array}{l} X = 0.022 \\ Y = 0.999 \\ Z = 0.019 \end{array} \times 255 = \begin{array}{l} 006 \\ 255 \\ 005 \end{array} \begin{array}{l} R \\ G \\ B \end{array}$$



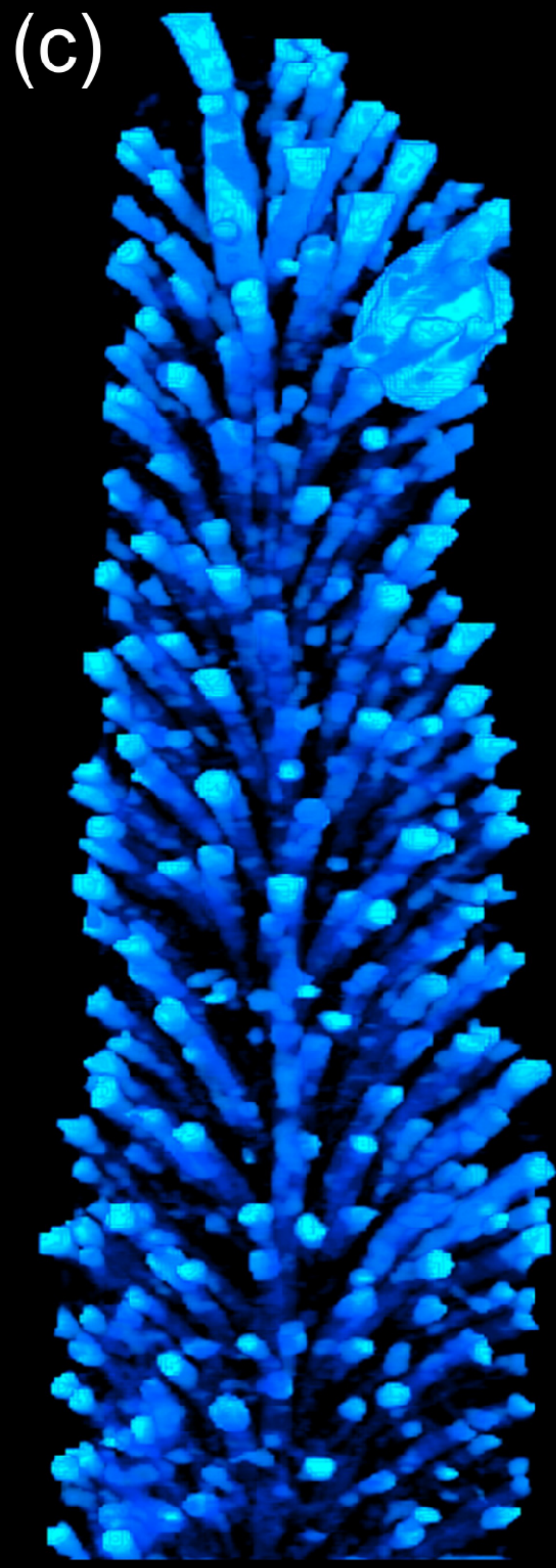
Figure 5.



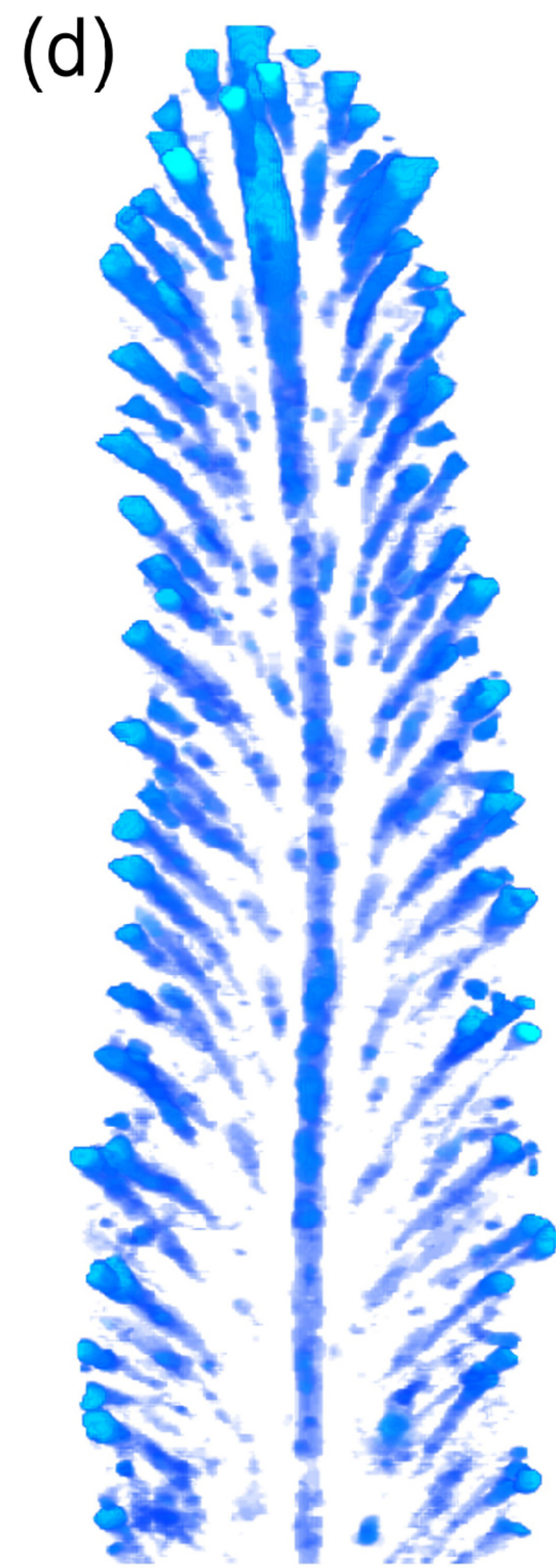
Coral pore structure



Pore radius (mm)  
0.08  1.3



Pore radius<sup>2</sup> (mm<sup>2</sup>)  
0.026  1.69



Longitudinal central section



Flow velocity ( $\mu\text{m/s}$ )  
 $3 \times 10^{-6}$   0.8

Figure 6.

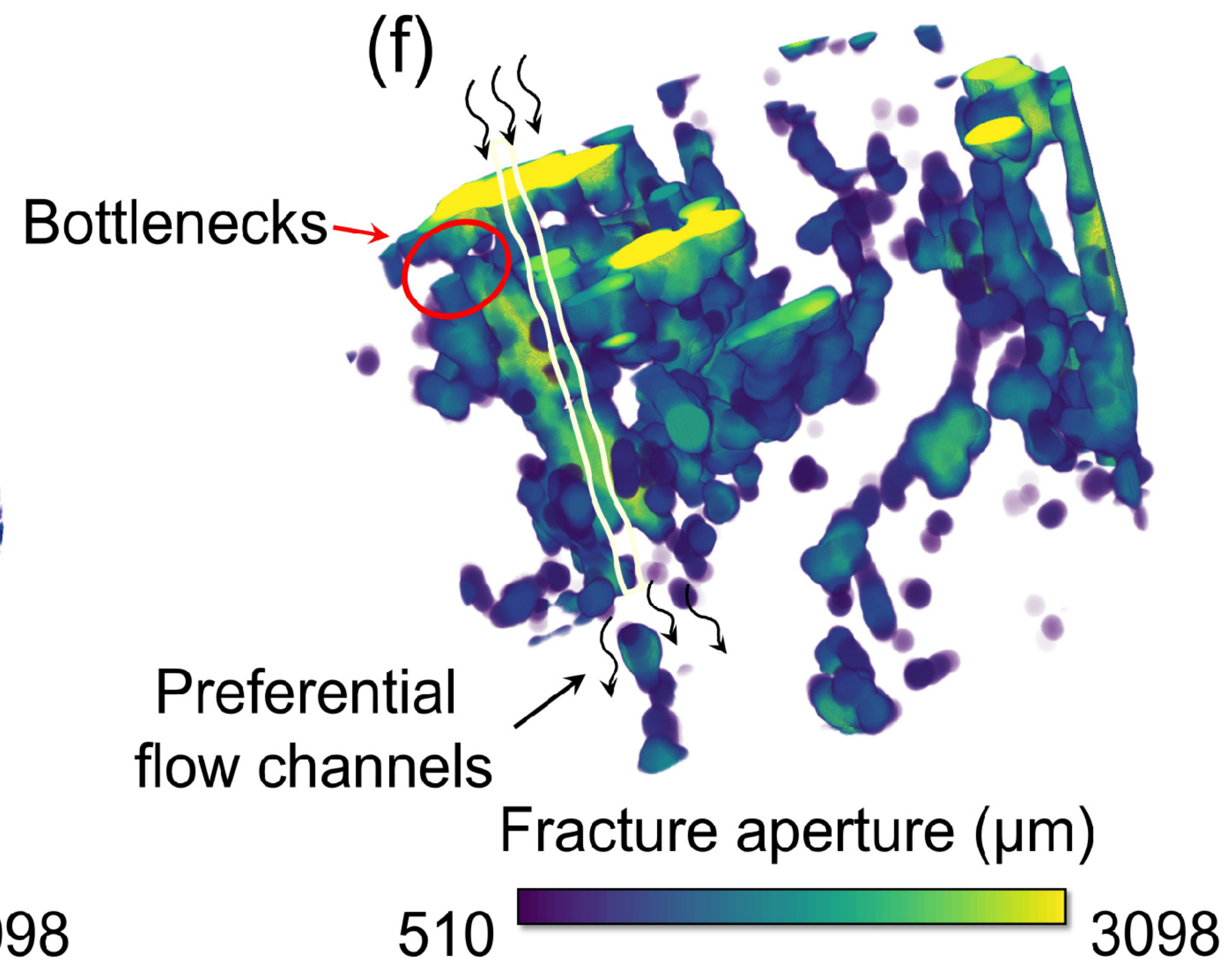
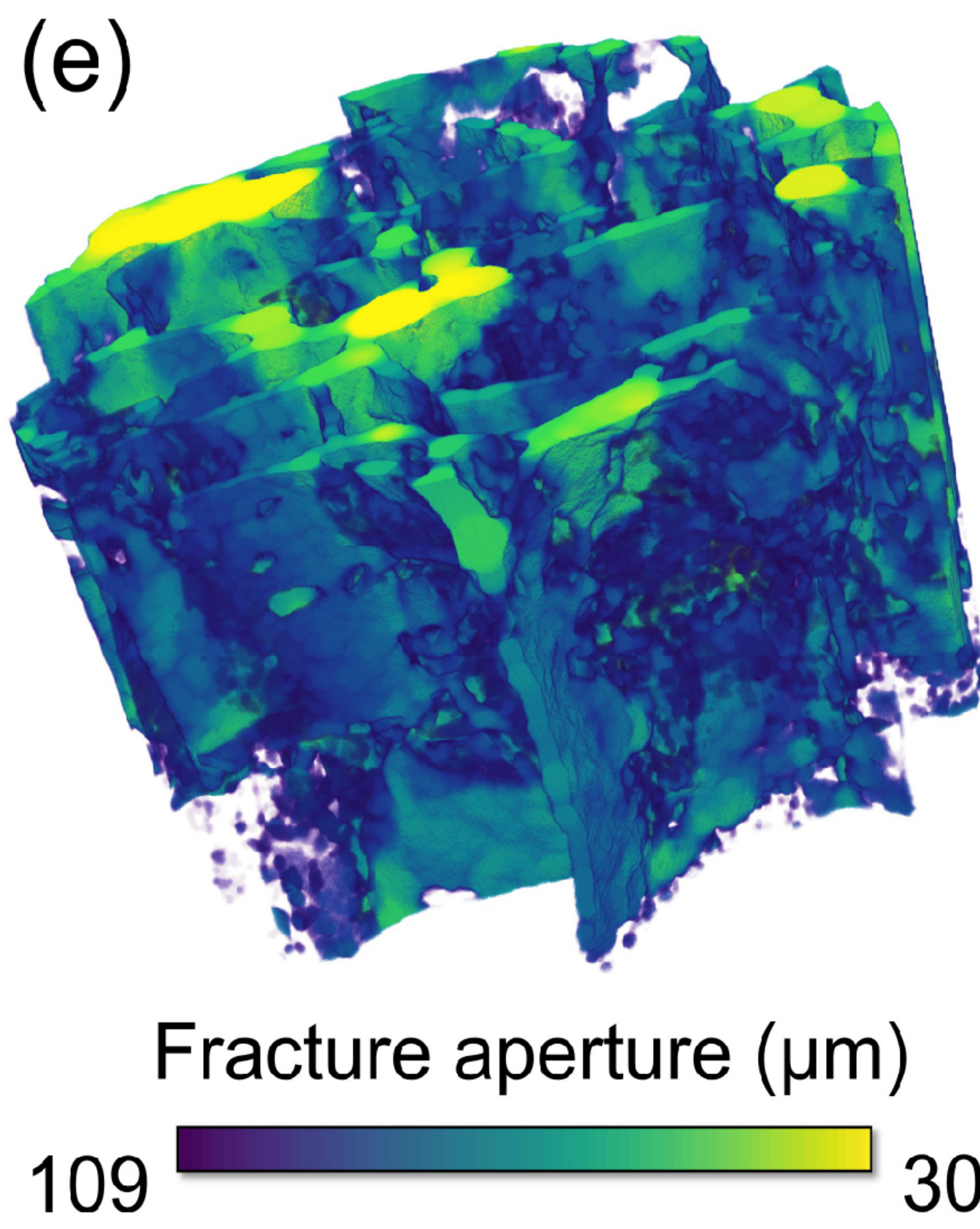
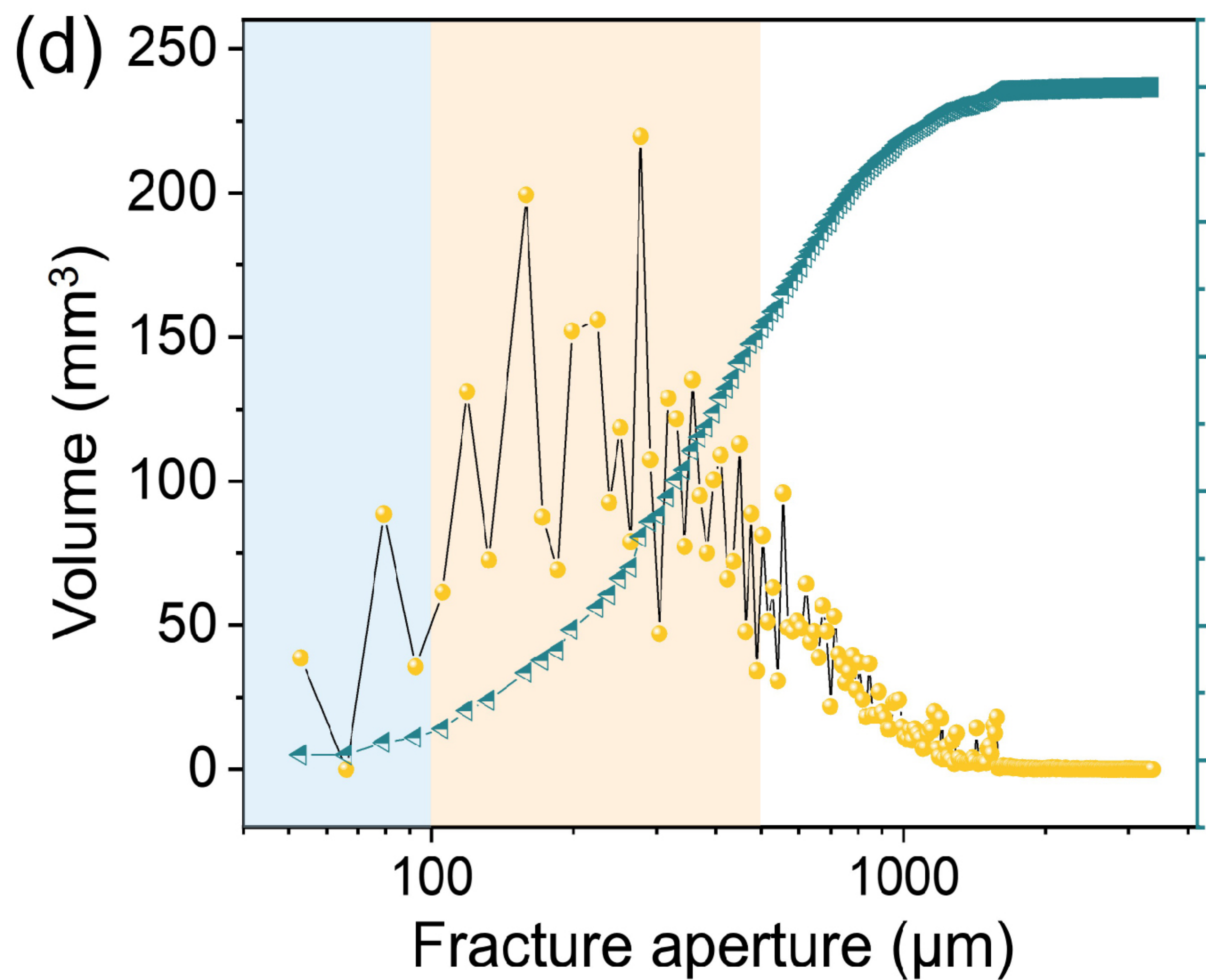
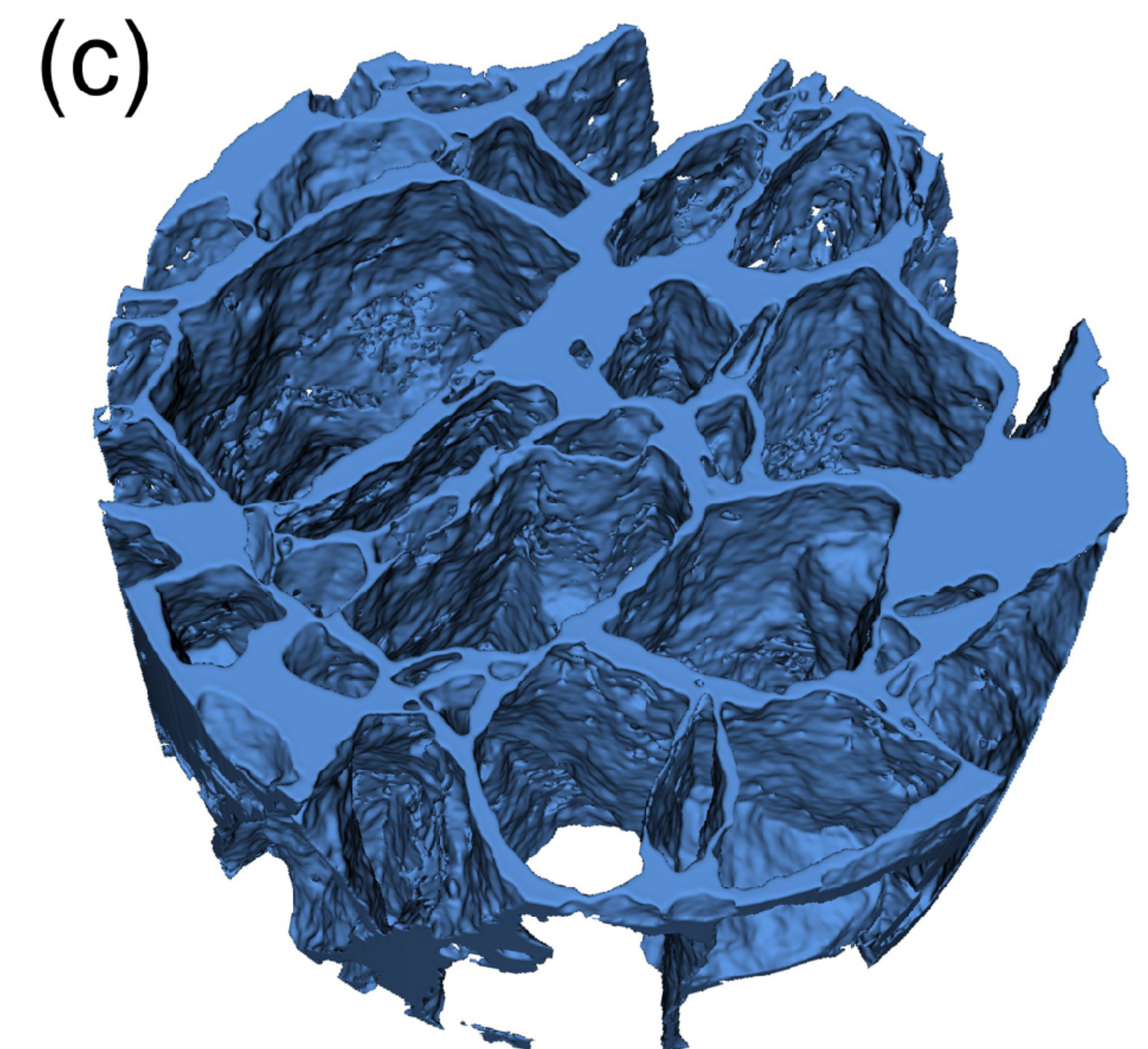
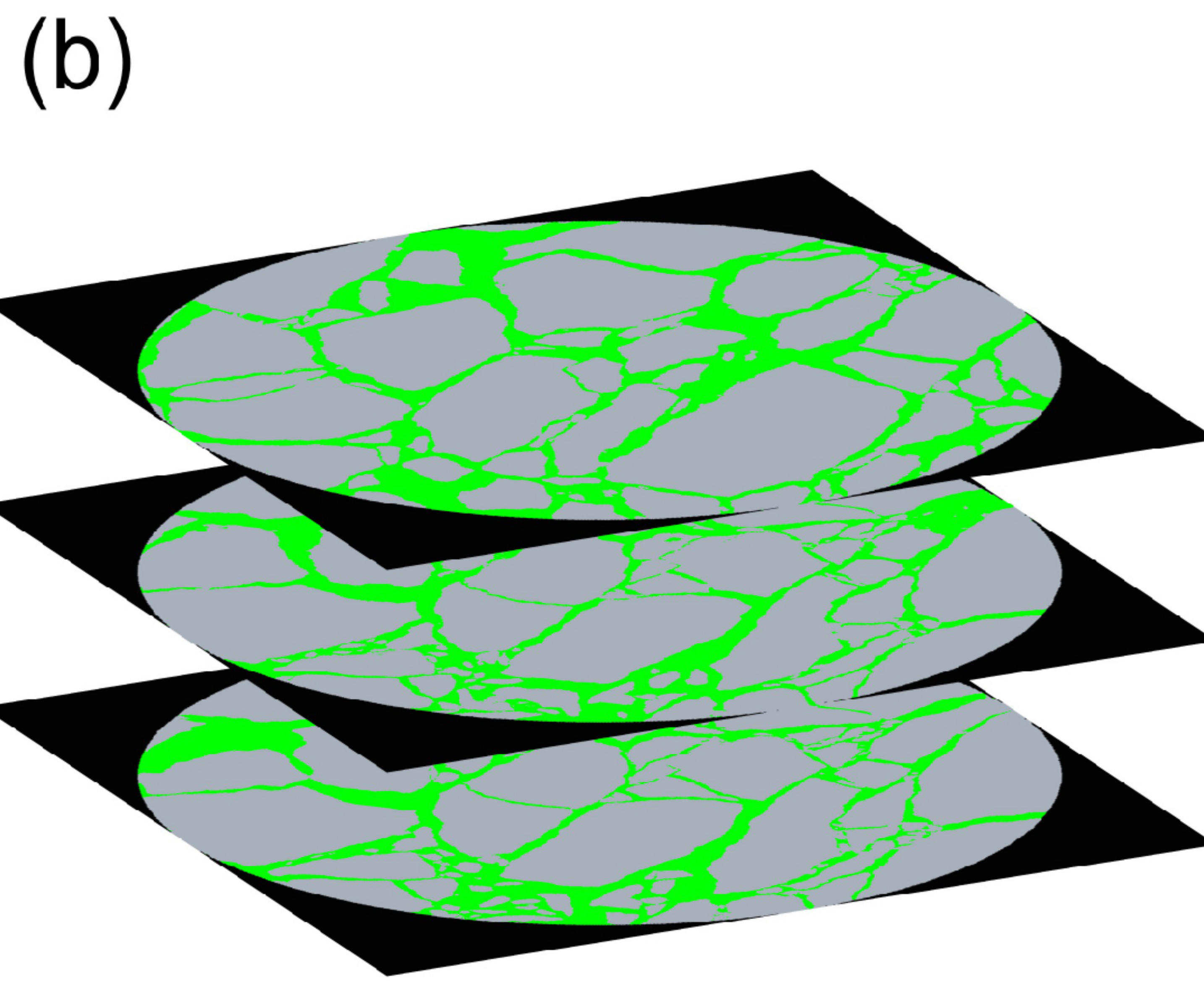
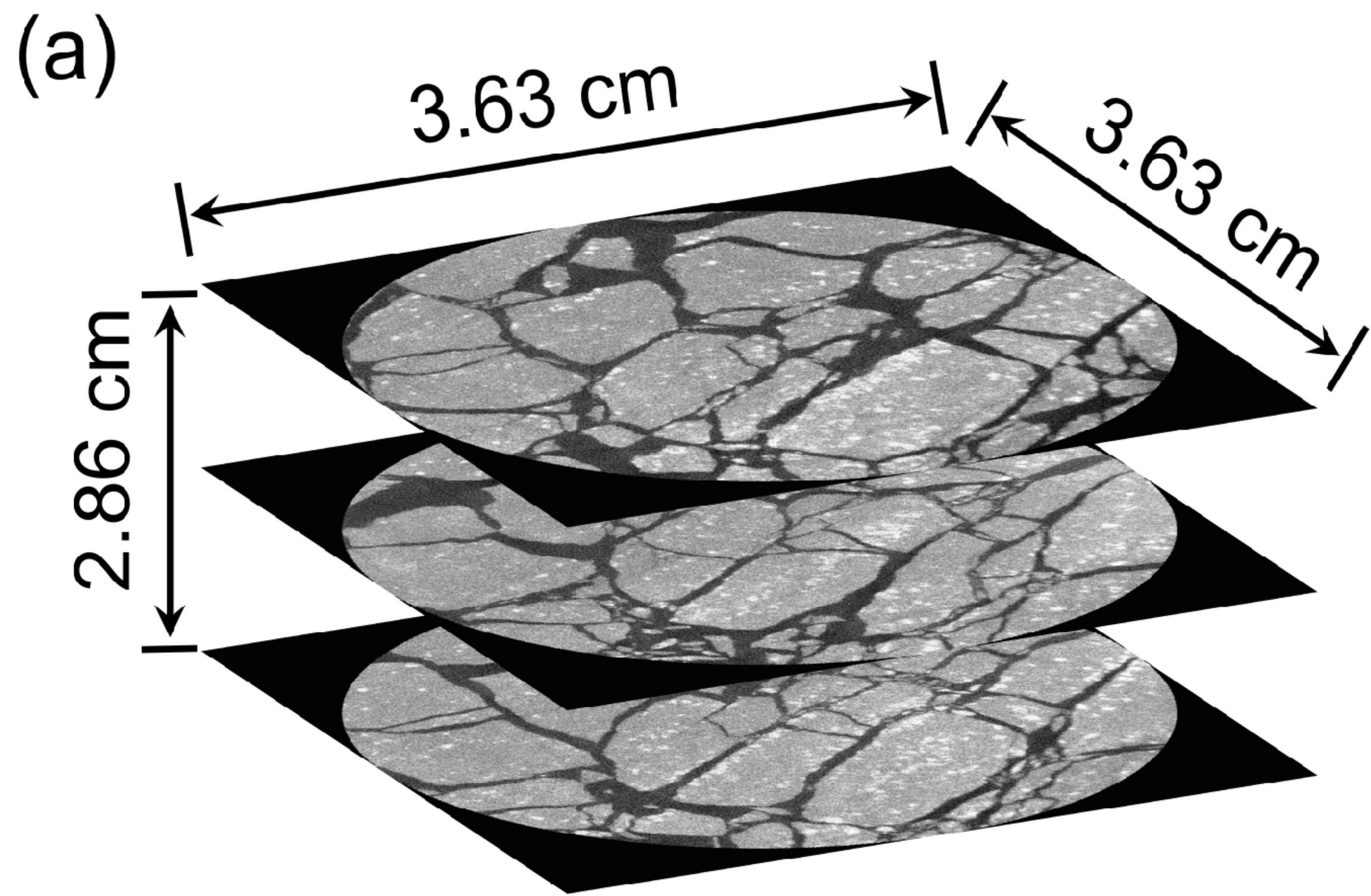


Figure 7.

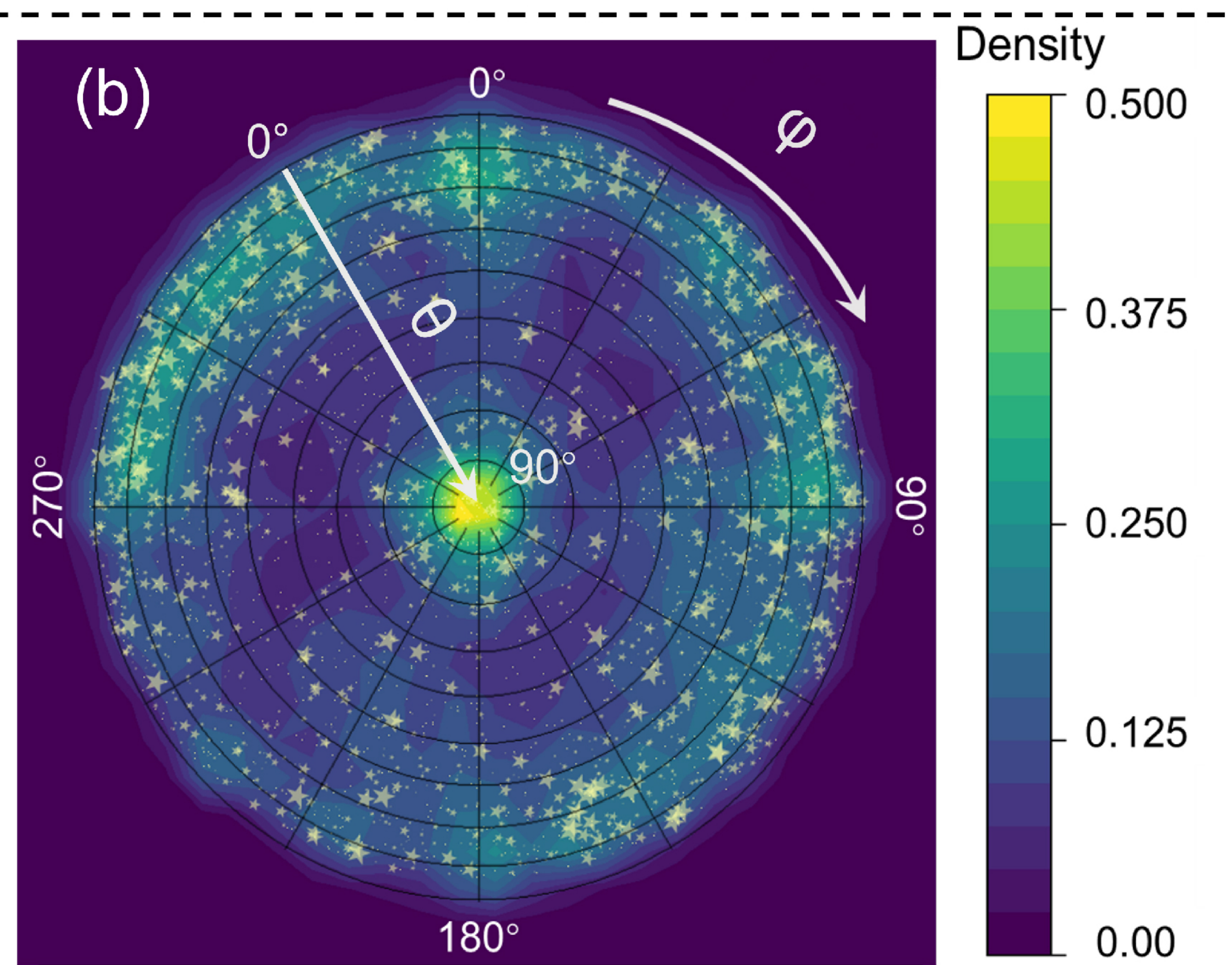
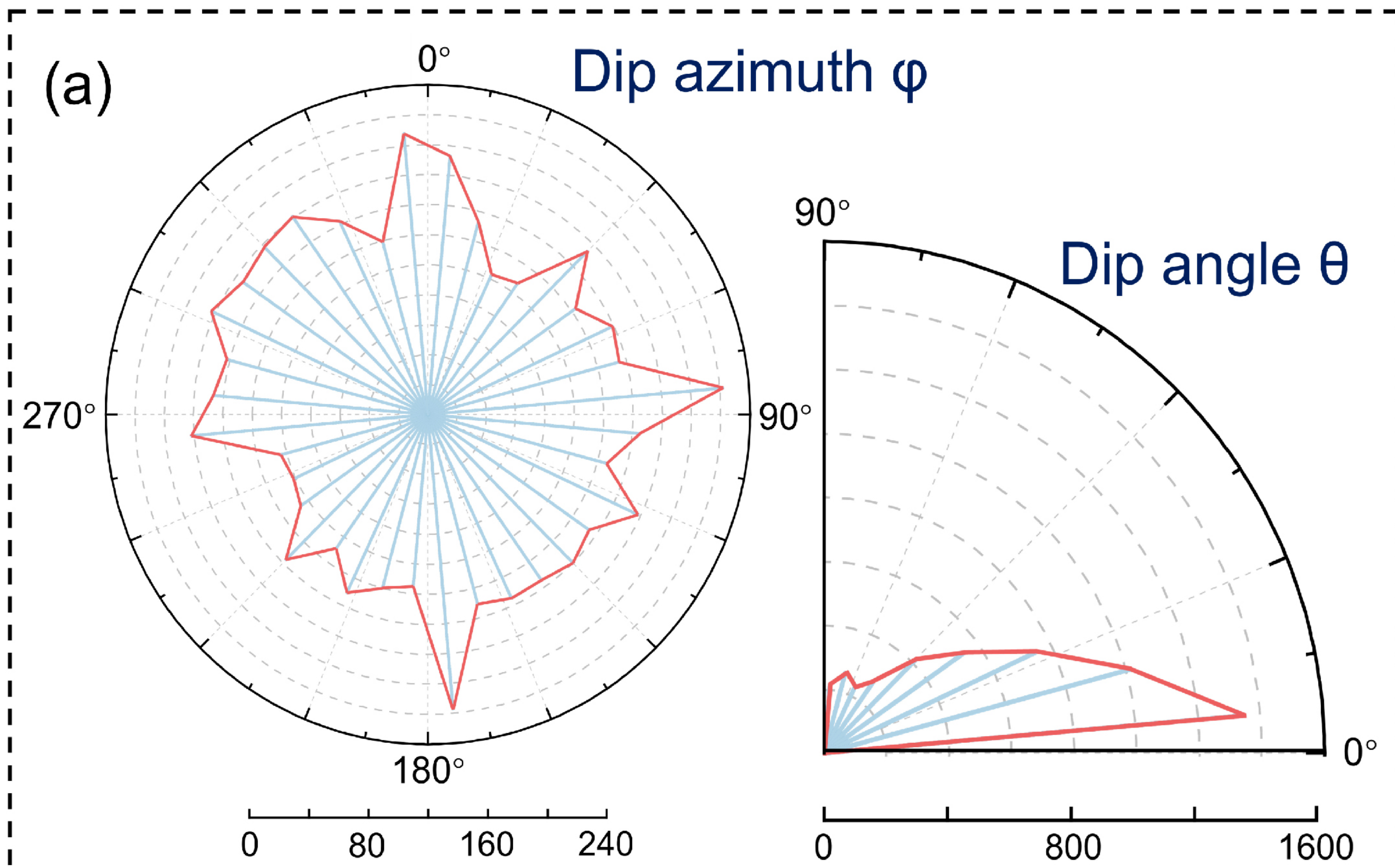
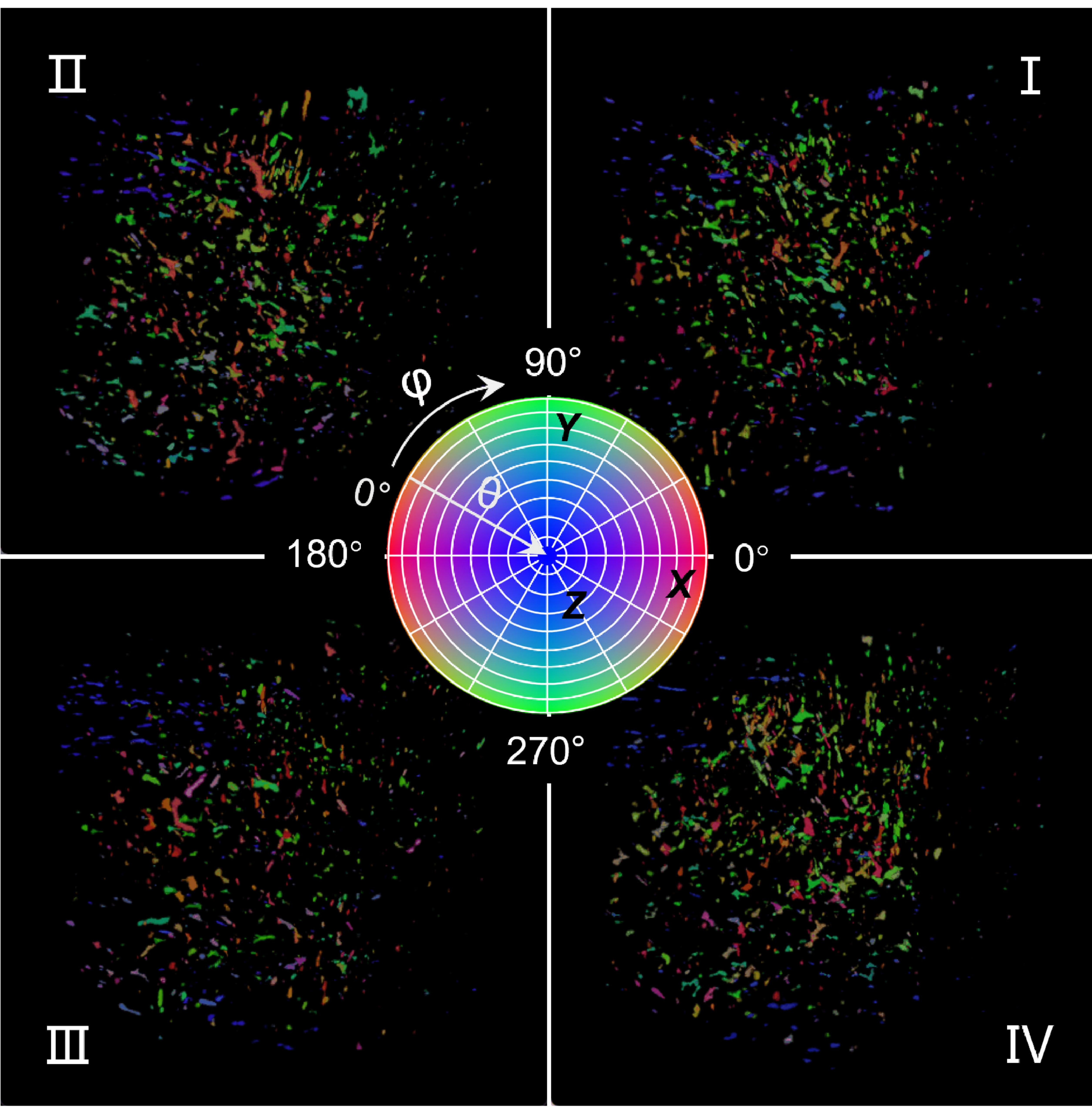


Figure 8.

(a) Orientation



(b) Orientation + Volume

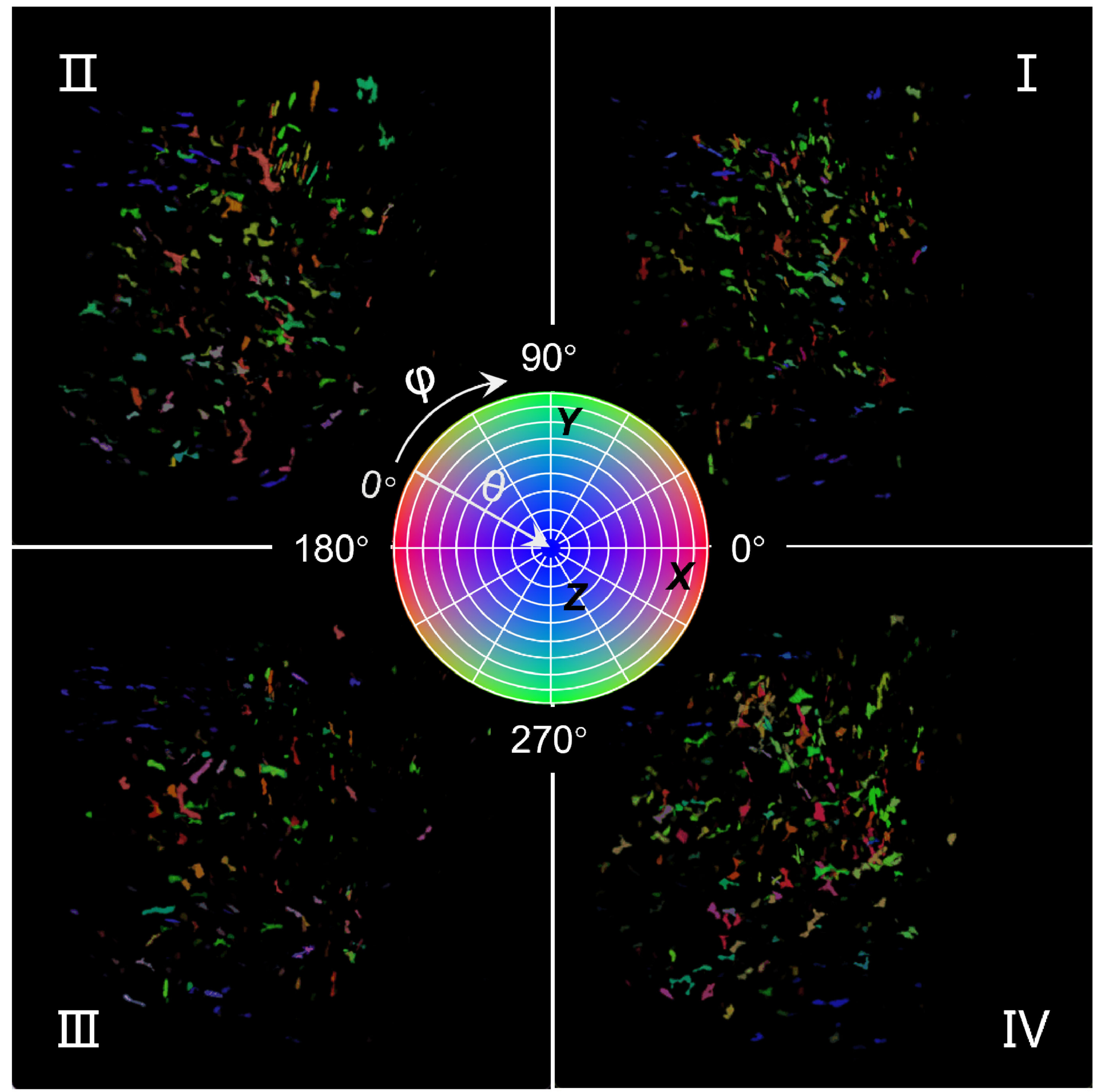
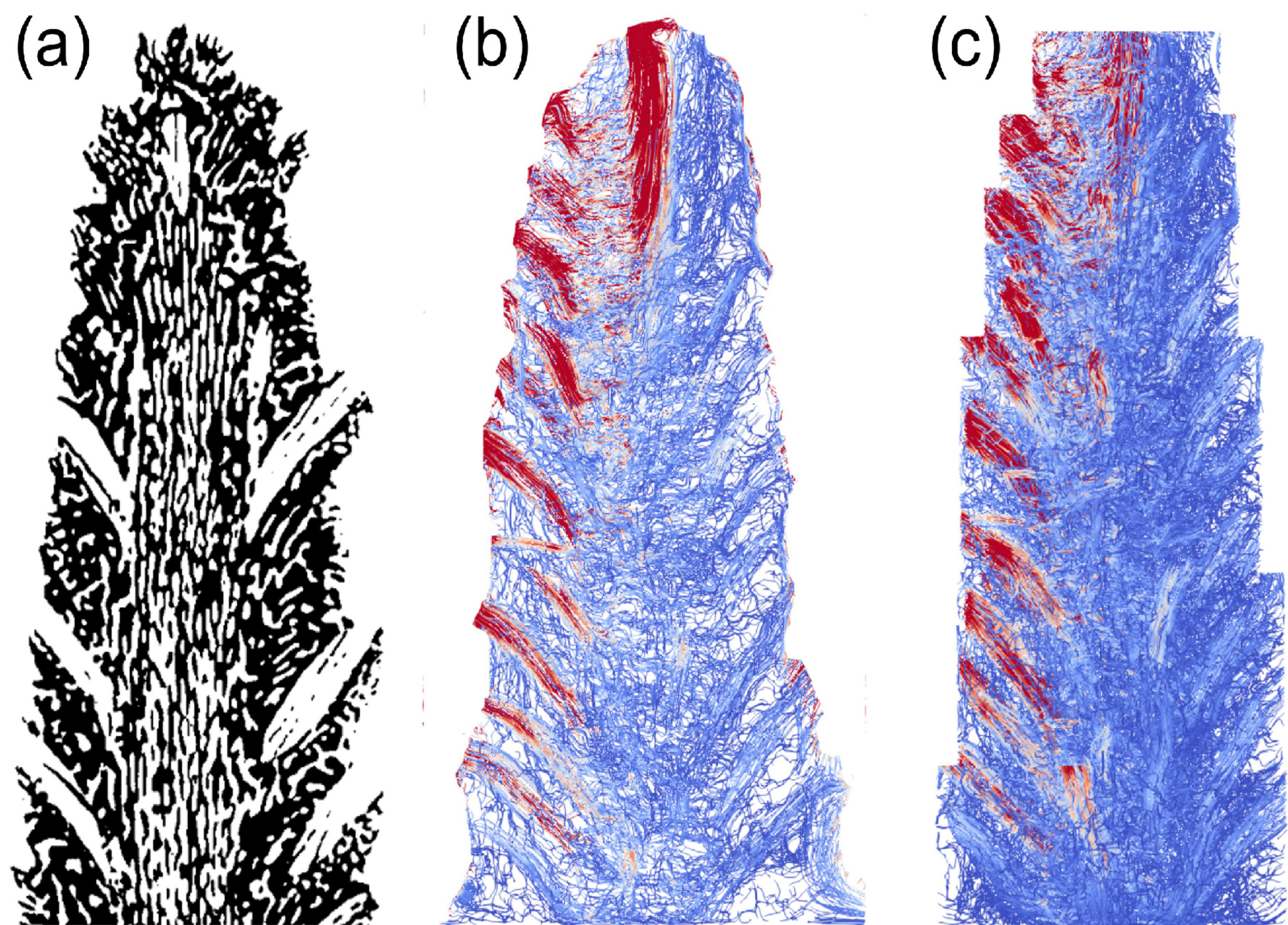
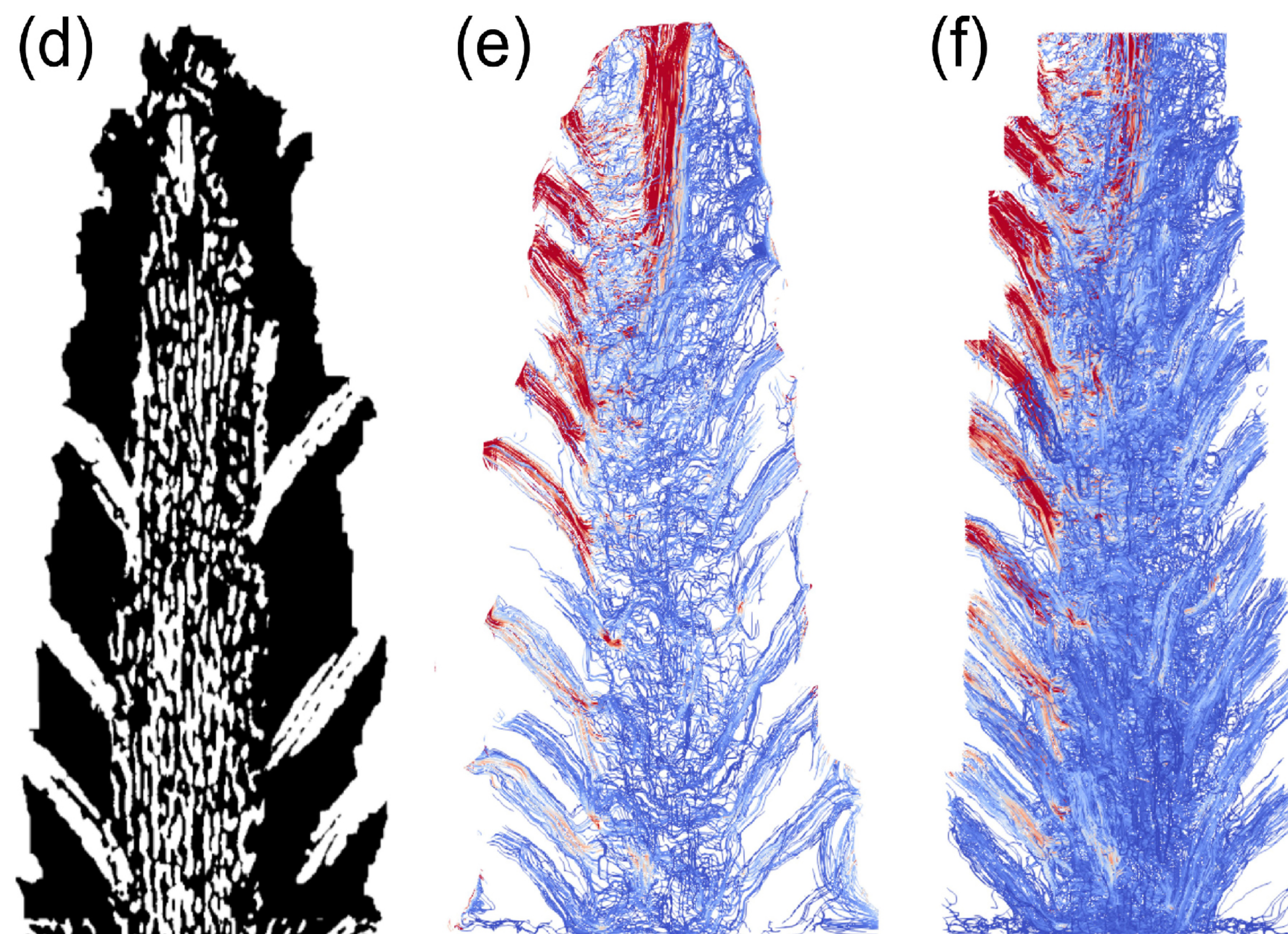


Figure 9.

Original model



Simplified model



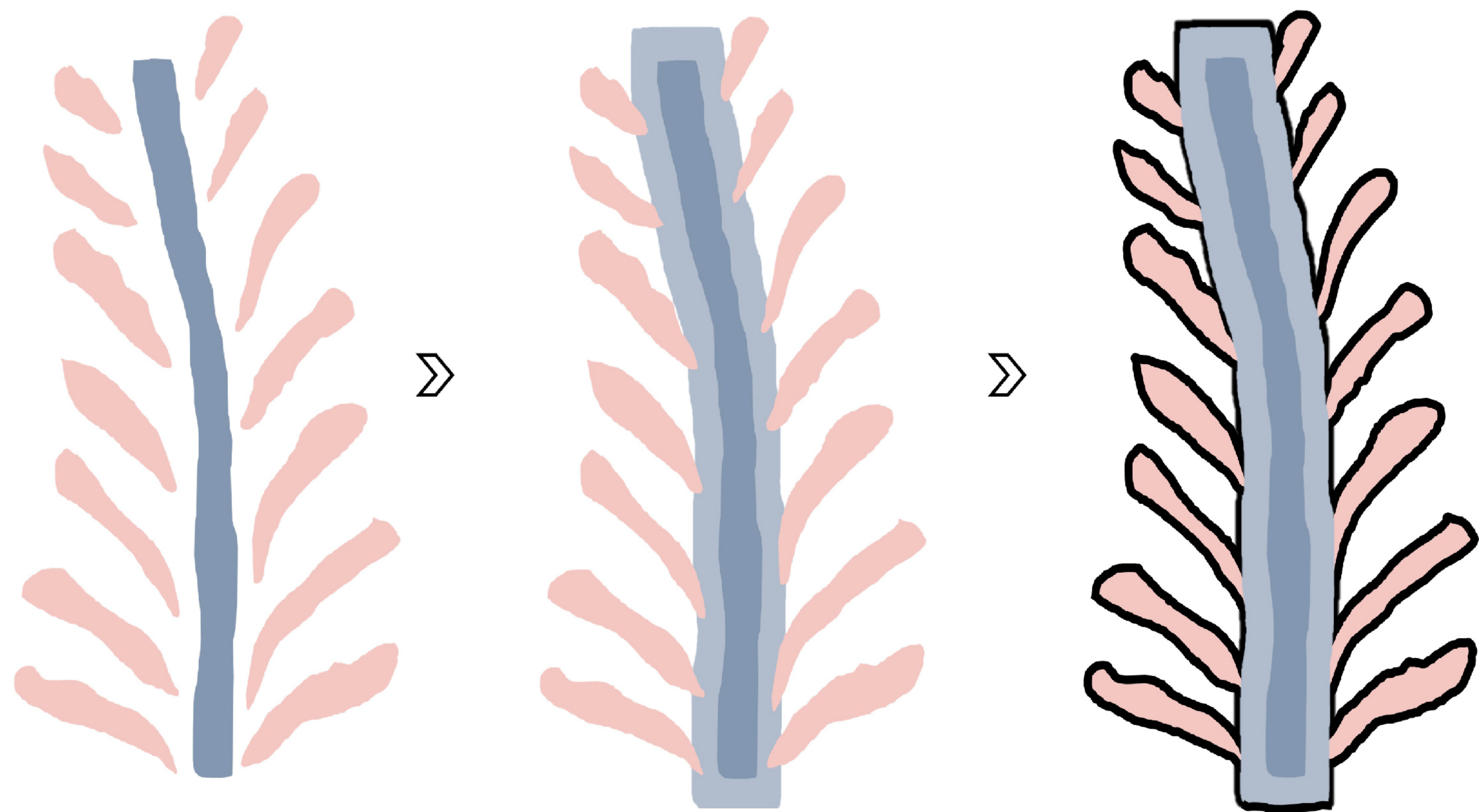
$2 \times 10^{-6}$  Flow velocity ( $\mu\text{m/s}$ ) 0.66

(g) Model simplification workflow

Main branchlets

Central dilation

Overall connectivity



Branchlets Central canal Dilated canal Identified region

(h) Velocity comparison

Selected regions

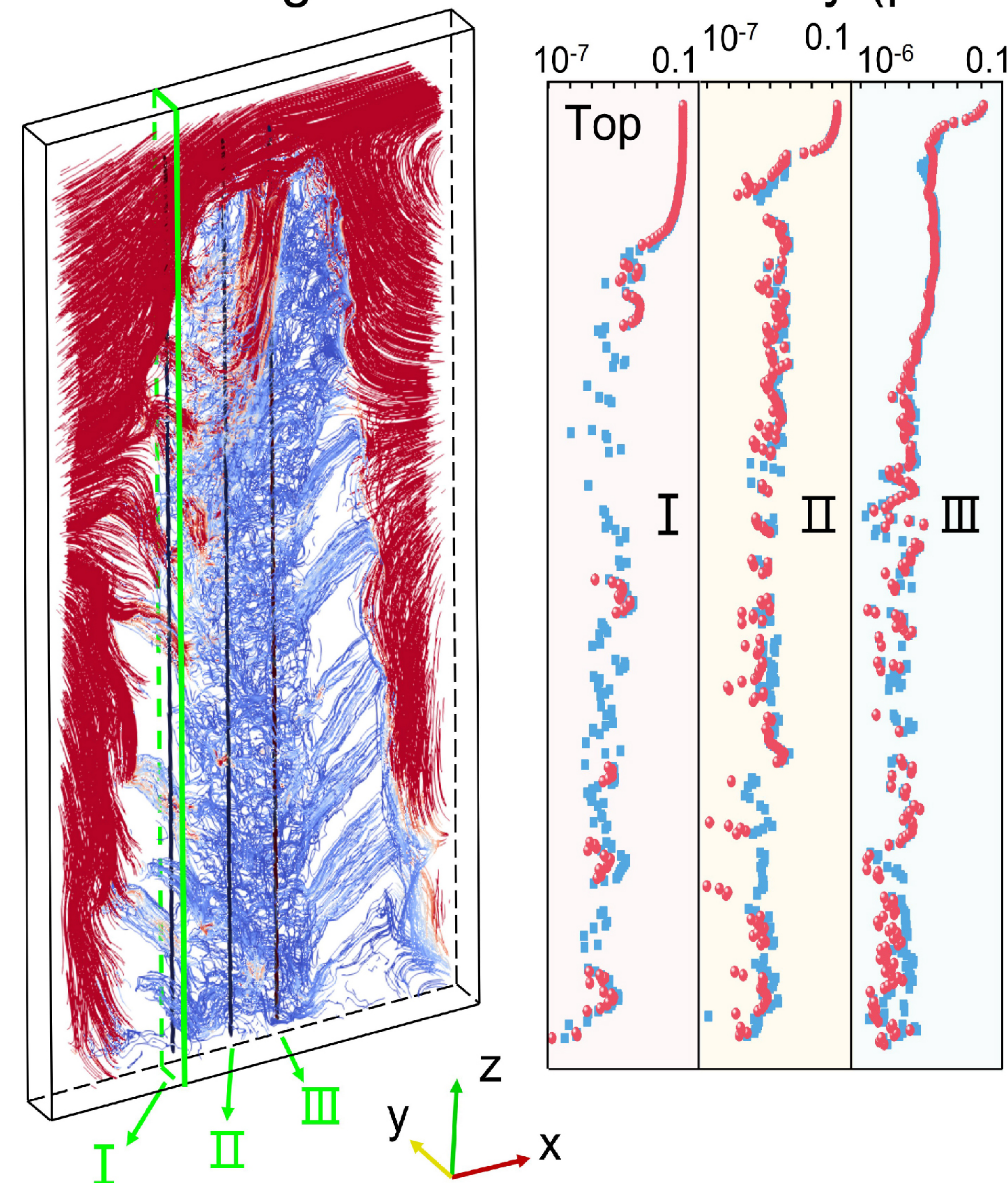
Flow velocity ( $\mu\text{m/s}$ )

Figure 10.

